Sveučilište u Rijeci
POMORSKI FAKULTET
FACULTY OF MARITIME STUDIES
University of Rijeka

University of Zagreb
Faculty of Transport
and Traffic Sciences

Royal Institute of Navigation
Science Technology Practice

ISSN 1849-7306

12th Annual Baška GNSS Conference

PROCEEDINGS

Under the High Auspicies of The European Academy of Sciences and Arts

Baška, Krk Island, Croatia
6 – 9 May 2018

Sveučilište u Rijeci
POMORSKI FAKULTET
FACULTY OF MARITIME STUDIES
University of Rijeka

University of Zagreb
Faculty of Transport
and Traffic Sciences

Royal Institute of Navigation
Science Technology Practice

12th Annual Baška GNSS Conference

PROCEEDINGS

Baška, Krk Island, Croatia

6 – 9 May 2018

Published by:

University of Rijeka, Faculty of Maritime Studies, Rijeka, Croatia

The Royal Institute of Navigation, London, UK

For the Publisher:

Prof Alen Jugović, PhD, Dean,
University of Rijeka, Faculty of Maritime Studies, Rijeka, Croatia

Publishing Associates:

Terry Moore, PhD FRIN FION, President,
The Royal Institute of Navigation, London, UK

John Pottle, FRIN, Director,
The Royal Institute of Navigation, London, UK

Editors:

Assoc Prof Kristijan Lenac, PhD, MRIN,
University of Rijeka, Faculty of Engineering, Rijeka, Croatia

Assist Prof David Brčić, PhD, MRIN,
University of Rijeka, Faculty of Maritime Studies, Rijeka, Croatia

Academician Serdjo Kos, PhD, FRIN,
University of Rijeka, Faculty of Maritime Studies, Rijeka, Croatia

Assist Prof Marko Valčić, PhD,
University of Rijeka, Faculty of Engineering, Croatia

Prof Alen Jugović, PhD,
University of Rijeka, Faculty of Maritime Studies, Rijeka, Croatia

Assist Prof Marko Horvat, PhD,
Zagreb University of Applied Sciences, Zagreb, Croatia

Front-page photo credits:

Renato Filjar: Tranquility in the winter afternoon

Text formatting:

Tempora, Rijeka

Print:

AKD d.o.o. Zagreb

Address:

University of Rijeka, Faculty of Maritime Studies
Studentska 2, 51000 Rijeka, Croatia
Phone: +385 (0)51 338 411, Fax: +385 (0)51 336 755
URL: http://www.pfri.uniri.hr/
E-mail: dekanat@pfri.hr

ISSN 1849-7306

Contents

Renato Filjar
ON SUITABILITY OF MASSIVE GNSS PSEUDORANGE DATA FOR GNSS POSITIONING PERFORMANCE STUDIES 7

Ivan Toman, Serdjo Kos, David Brčić
ON LONG-TERM SOLAR ACTIVITY IMPACT ON GPS SINGLE-FREQUENCY 3D POSITIONING ACCURACY IN THE ADRIATIC REGION 27

Michael Pattinson, Smita Tiwari, Yuheng Zheng, María Campo-Cossio, Raúl Arnau, David Obregón, Ander Ansuategui, Carlos Tubio, Iker Lluvia, Oscar Rey, Jeroen Verschoore, Libor Lenza, Joaquin Reyes
GNSS PRECISE POINT POSITIONING FOR AUTONOMOUS ROBOT NAVIGATION IN GREEN-HOUSE ENVIRONMENT FOR INTEGRATED PEST MONITORING 51

Serdjo Kos, Barbara Pongračić, David Brčić
A STUDY ON MULTI-CONSTELLATION GNSS POSITIONING PERFORMANCE IN TERMS OF MARITIME REQUIREMENTS 69

Matej Bažec, Franc Dimc
SENSING SDR-BASED GNSS JAMMERS 85

Serdjo Kos, Mario Bakota, David Brčić
PARTICULARITIES OF DETERMINING THE VESSEL POSITION, COURSE AND SPEED AND THE IONOSPHERIC ERROR BY USING DUAL-BAND GLONASS RECEIVERS 97

Franko Hržić, Diego Sušanj, Kristijan Lenac
OPTIMAL BEACON POSITIONING FOR INDOOR DRONE NAVIGATION 109

Takashi Kubota, Nobuyoshi Kouguchi, Yoshihiro Kurihara
COMPARISON OF HEADING INFORMATION OBTAINED WITH MODERN GPS-BASED NAUTICAL INSTRUMENTS 119

Alan Mahne Kalin, Dejan Žagar, Peter Vidmar
INTEGRATED APPROACH TO SAILING BOAT CONTROL PROBLEM 137

International Programme and Organising Committee:

John Pottle, FRIN, Director, The Royal Institute of Navigation, London, UK, Conference Chair

Jasna Prpić-Oršić, University of Rijeka, Faculty of Engineering, Croatia, Conference Co-chair
Academician Serdjo Kos, FRIN, University of Rijeka, Faculty of Maritime Studies, Croatia, Co-chair
Hrvoje Gold, University of Zagreb, Faculty of Transportation and Traffic Sciences, Croatia, Co-chair
Tomislav Kos, FRIN, University of Zagreb, Faculty of Electrical Engineering and Computing, Croatia, Co-chair

Mia Filić, MRIN, satellite navigation, statistical learning, SDR, and space weather specialist, Sesvete, Zagreb, Croatia, Conference Programme Chair

Terry Moore, FRIN, President, The Royal Institute of Navigation, London, UK
Jeffrey M Auerbach, US Department of State, Washington, DC, USA
Kristijan Lenac, MRIN, University of Rijeka, Faculty of Engineering, Croatia
David Brčić, MRIN, University of Rijeka, Faculty of Maritime Studies, Croatia
Ljiljana R Cander, Rutherford Appleton Laboratory, Chilton, UK
Olja Čokorilo, University of Belgrade, Faculty of Transport and Traffic Engineering, Serbia
Jordi Corbera, Institut Cartogràfic i Geològic de Catalunya, Barcelona, Spain
Giovanni E Corazza, University of Bologna, Italy
Robert Crane, National Coordination Office for Space-Based PNT, Washington, DC, USA
Franc Dimc, University of Ljubljana, Faculty of Maritime Studies and Transport, Portorož, Slovenia
Shaoujun Feng, FRIN, Imperial College, London, UK
Sharafat Gadimova, UN Office of Outer Space Affairs, Vienna, Austria
Luka Grubišić, University of Zagreb, Faculty of Science, Croatia
Darko Huljenić, MRIN, Ericsson Nikola Tesla, Zagreb, Croatia
Siniša Krajnović, LM Ericsson, Stockholm, Sweden
Bal Krishna, Coordinates Journal, Delhi, India
Marta Krywanis-Brzostowska, European GNSS Agency, Prague, Czech Republic
David Last, FRIN, Consultant Engineer and Expert Witness, Conwy, UK
Andrea Lučić, MRIN, satellite navigation and SDR specialist, Rijeka, Croatia
Anastasia Lyubimova, GLONASS/GNSS Forum Association, Moscow, Russia
Roger A McKinley, Consultant, Leatherhad, UK
WashingtonYochieng, FRIN, Imperial College,London, UK
Ivan Rumora, Croatian Navy, Pula, Croatia
Laura Ruotsalainen, Finnish Geodetic Institute, Masala, Finland
Nenad Sikirica, Polytechnic Hrvatsko Zagorje Krapina, Krapina, Croatia
Enik Shytermeja, Ecole Nationale de l'Aviation Civile, Toulouse, France
Grigory Stupak, Russian Space Systems, Moscow, Russia
Marko Ševrović, MRIN, University of Zagreb, Faculty of Transport and Traffic Sciences, Croatia
Marko Valčić, University of Rijeka, Faculty of Engineering, Croatia
Adam Weintrit, FRIN, Faculty of Navigation, Gdynia Maritime University, Gdynia, Poland
Jingnong Weng, Beihang University of Aeronautics and Astronautics, Beijing, China
Falin Wu, Beihang University, Beijing, China
Xiaosu Yi, Beihang University, Beijing, China

List of reviewers:

Tomislav Kos (Croatia), David Brčić (Croatia), Mate Barić (Croatia), Luka Grubišić (Croatia), Josip Vuković (Croatia), Franc Dimc (Slovenia), Mario Muštra (Croatia), Diego Sušanj (Croatia), Laura Ruotsalainen (Finland), Serdjo Kos (Croatia), Marko Valčić (Croatia), Kristijan Lenac (Croatia), Antonela Trbović (Croatia)

Sveučilište u Rijeci
POMORSKI FAKULTET
FACULTY OF MARITIME STUDIES
University of Rijeka

University of Zagreb
Faculty of Transport
and Traffic Sciences

Royal Institute of Navigation
Science Technology Practice

12th Annual Baška GNSS Conference

PROCEEDINGS

Sveučilište u Rijeci
POMORSKI FAKULTET
FACULTY OF MARITIME STUDIES
University of Rijeka

University of Zagreb
Faculty of Transport
and Traffic Sciences

Royal Institute of Navigation
Science Technology Practice

12th
Annual
Baška GNSS
Conference

ON SUITABILITY OF MASSIVE GNSS PSEUDORANGE DATA FOR GNSS POSITIONING PERFORMANCE STUDIES

Renato Filjar[1,2]

[1] University of Rijeka, Faculty of Engineering, Rijeka, Croatia
[2] Polytechnic of Zagreb, Zagreb, Croatia
e-mail: renato.filjar@gmail.com

Abstract

GNSS positioning performance assessment is the fundamental process that allows for definition of quality of GNSS-based services, and risk analysis of GNSS utilisation as a pre-requisite for robust and reliable GNSS applications. Such an assessment should encompass as many real situations as possible to avoid encounter with the unexpected situations of GNSS positioning performance deterioration. Here we examine the case of utilisation of experimentally collected GNSS observations within the International GNSS Service network. Here the methodology of the IGS observations utilisation for GNSS positioning performance studies is outlined. Then, the suitability of the IGS observations for three scenarios of GNSS positioning environments (ionosphere, troposphere, and multipath) are examined based on research on IGS data availability in two-weeks period in September 2017. Opportunities for multi-GNSS studies, including GNSS anti-spoofing, are examined. The IGS is considered as a template for the other GNSS observations voluntary collection initiatives, such as the one our team has proposed for smartphone multi-GNSS observations collection. The study results are presented and discussed, identifying shortcomings and obstacles for an advanced utilisation. This manuscript concludes with summary of findings and proposals for recommendations

Keywords: *GNSS pseudorange, massive data set, GNSS SDR, positioning performance, positioning environment reconstruction*

1. INTRODUCTION

Satellite navigation is one of the pillars of the modern civilisation and society, and enabling technology for a rising number of technology and socio-economic systems and services (Thomas *et al.,* 2011, UK Government Office for Science 2018, Sadlier *et al.,* 2017). It has been recognised as a component of national infrastructure, and a public good. Applications of Global Navigation Satellite Systems (GNSS) rely on accurate, available, and continuity- and integrity-guaranteed GNSS Positioning, Navigation and Timing (PNT) services (UK Government Office for Science, 2018). The reliance requires GNSS positioning performance assessment as an essential input for GNSS utilisation risk analysis (Thomas *et al.,* 2011, UK Government Office for Science, 2018, Sadlier *et al.,* 2017). The GNSS utilisation risk assessment requires GNSS positioning performance analysis in various scenarios and environments of GNSS utilisation that may affect the quality of GNSS PNT-based services and systems (UK Government Office for Science, 2018). Such an analysis is performed based on either observations taken in the utilisation scenario conducted in real environment, or observations taken as the result of carefully and accurately modelled simulation. The value of real-environment data may be recognised immediately, leading to initiative for systematic collection of real-environment data in particular utilisation scenarios for the advantage of science, strategy, industry, and education. With the transparent GNSS position estimation process, the GNSS community of scientists, engineers, strategists, regulators, application developers and operators, and GNSS users may advantage with the access to a large database of raw GNSS position estimates and pseudoranges, taken systematically in real positioning environments for defined GNSS utilisation scenarios (Sadlier *et al.,* 2017, SaPPART, 2017). Recent developments in proprietary Android Location API (GSA GNSS Raw Measurements Task Force, 2017), the smartphone operating system that dominates the market, allow for raw GNSS pseudoranges collection with commercial-grade single- and dual-freqeuncy low-cost GNSS receiver embedded in devices owned by literary everyone (Filić and Filjar, 2018c). The introduction of Software-Defined Radio (SDR) concept (Stewart *et al.,* 2015) in satellite navigation benefits the GNSS community with an open and transparent tool for objective GNSS positioning performance assessment in various GNSS position estimation conditions (Filić, Filjar and Ruotsalainen, 2016).

Space weather and its inducing effects on geomagnetic field and the Earth's ionospheric dynamics pose the single source of profound causes for GNSS positioning performance degradations, that translate into Quality of Service (QoS) deterioration

of GNSS-based applications (Canon *et al.,* 2013, Filić and Filjar, 2018a). Studies of GNSS positioning performance in various utilisation scenarios and different space weather positioning environment conditions are essential in GNSS utilisation risk assessment (Filić, Filjar and Ruotsalainen, 2016, SaPPART, 2017). A widespread global network of stationary GNSS reference stations has been developed in recent decades to provide scientists, engineers and the other interested parties with GNSS pseudorange observations contaminated with ionospheric effects at various scales. Known as the International GNSS Service (IGS, 2018), this network consists of individually funded and operated dual-frequency (often multi-GNSS) GNSS receivers that collect GNSS pseudoranges and GNSS navigation messages continuously every 30 s throughout 24 hours of every day in a year. Observations are raw (uncorrected) in the sense of ionospheric effects, with all the other sources of degradation, such as multipath and tropospheric errors, suppressed at various levels of success. Observations of GNSS pseudoranges are stored in electronic form of RINEX files. As the result, collected GNSS pseudoranges retain the deteriorating effects induced by space weather, geomagnetic and ionospheric processes, allowing for evidence-based analysis (Filić, Filjar and Ruotsalainen, 2016, Filić, 2017a, Filić, 2018).

The IGS database is an essential tool for every space weather, ionospheric and GNSS scientist or engineer. People behind the IGS work extensively to provide raw GNSS observations in systematic and accurate way, and with highest quality of data, the prime requirement for a successful research.

Here we discuss the extent of the IGS data quality through analysis of spatio-temporal availability and content of the IGS observations throughout an extended period of time. The suitability of the largest internet-based GNSS observations database is studied for potential exploitation in GNSS positioning performance assessment.

2. METHODOLOGY

The study of the massive IGS data suitability for GNSS positioning performance studies assessed the quality of IGS GNSS pseudoranges in terms of continuity and availability. This section discusses the means for GNSS positioning performance assessment, utilisation of the GNSS SDR for GNSS positioning performance assessment and the role of GNSS pseudoranges in GNSS positioning estimation process.

2.1 *GNSS positioning performance* is the target of every GNSS utilisation risk assessment study. It is determined through definition of four essential GNSS PNT performance parameters (Parkinson and Spilker Jr, 1996): (1) accuracy, (2) availability, (3) integrity, and (4) continuity.

Accuracy of GNSS PNT service is defined as ability to provide an environment for position, velocity and time estimation with the estimation error within the acceptable limits. It is expressed in the form of the vector of GNSS positioning error component values observed with a stationary GNSS receiver of a known position during a period of time (usually 24 hours). Alternatives include the positioning error presentation in the form of the 2σ horizontal 24-hours GNSS positioning error, depicted in Figure 1.

Availability of GNSS PNT service refers to the number of visible (usable) satellites a GNSS receiver is capable of signal reception from at an instant of time, or over the period of assessment. In latter case, the minimum number of visible satellites is concerned with.

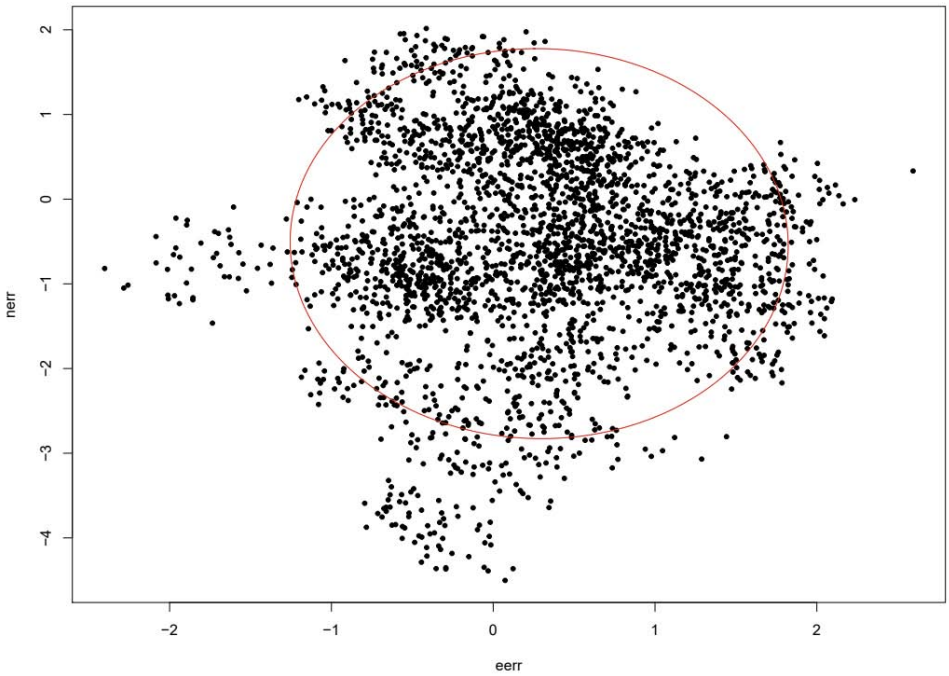

Figure 1. An example of the GNSS 2σ 24-hours horizontal positioning error representation

Integrity of GNSS PNT service is defined as an ability to detect a system's malperformance and to inform the user of it. It is expressed in the time between the occurrence of disruption and the instance users receive the notification on it.

Continuity of GNSS PNT service is defined as ability to provide seamless positioning, navigation and timing service. It is expressed as the time between the two consecutive position estimates (position fixes).

An objective, unbiased and independent assessment of GNSS positioning performance requires provision of experimentally observed raw (uncorrected) GNSS pseudoranges and navigation messages (Filić, Filjar and Ruotsalainen, 2016). Those are to be processed further using the very methods and position estimation procedures used in targeted classes of GNSS receivers. Ideally, the GNSS receiver of a targeted class should be used for post-processing the observations.

Obtained GNSS-based position estimates are then compared with actual (true) position of a stationary reference station, and time series of positioning error components (northing, easting, and vertical/height) are determined (Filić, Filjar and Ševrović, 2018, SaPPART, 2017) as defined in (1):

$$\begin{bmatrix} \epsilon_{northing} \\ \epsilon_{easting} \\ \epsilon_{vertical} \end{bmatrix} = \begin{bmatrix} latitude_{est} \\ longitude_{est} \\ height_{est} \end{bmatrix} - \begin{bmatrix} latitude_{true} \\ longitude_{true} \\ height_{true} \end{bmatrix} \tag{1}$$

2.2 *GNSS SDR for research*. The Software-Defined Radio (SDR) approach is a known concept of dedicated hardware replacement with dedicated software run on general-purpose hardware, such as a PC, or a smartphone, for radio communication purposes (Stewart *et al.,* 2015). The concept has found a firm establishment in satellite navigation (Filić, Filjar and Ruotsalainen, 2016), where just a minor portion of signal and data processing relies on hardware-specific processing, mostly in radio-frequency domain and for the analog-to-digital (A/D) conversion.

Transition of base-band and navigation processing domains to software, rather than hardware, renders them transparent and eligible for bespoke modifications to balance the complexity and the actual requirements for accuracy needed for targeted GNSS applications (Figure 2). Researchers and engineers may benefit from that transparency with an opportunity to examine intermediate results (before the position estimation is completed), thus developing an insight into quality of position estimation algorithms and into the nature error sources effects to position estimation errors.

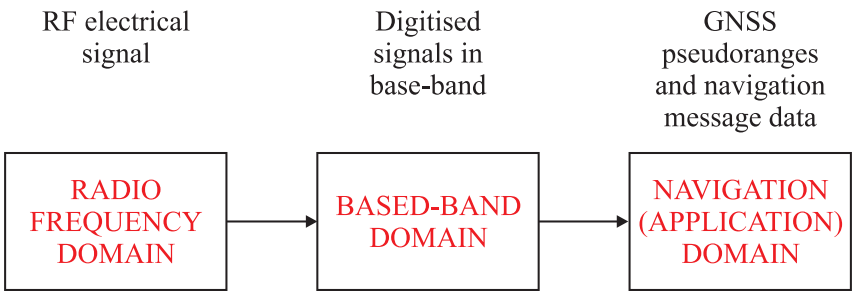

Figure 2. Division of signal and data processing in a GNSS SDR receiver

Generally, the raw GNSS pseudorange observations are contaminated with measurement errors caused by ionospheric, tropospheric and multipath effects, related to the particular satellite's signal. The effect of contamination is reduced through the pre-processing of GNSS observations, as depicted in Figure 3. Position of every satellite involved in the process, taken at the time of the signal broadcast, may be determined using data provided in navigation message, and is expressed in the vector form as shown in (2)

$$\vec{x_i} = (x_{Si}, y_{Si}, z_{Si})^{\mathrm{T}} \tag{2}$$

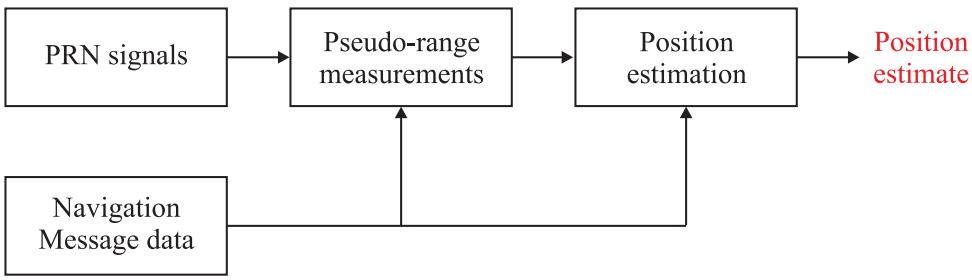

Figure 3. Pre-processing of raw GNSS pseudoranges is conducted for mitigation of systematic pseudorange measurement errors

Relationship between observed raw GNSS pseudorange, the actual distance of propagation, and causes of error may be expressed using the additive model given in (3) (Filić and Filjar, 2018a, Filić, 2017a, Oxley, 2017, Parkinson and Spilker Jr, 1996).

$$\rho_i = R_i + c \cdot b_{rec} + \epsilon_{iono}(i) + \epsilon_{tropo}(i) + \epsilon_{multipath}(i) + \epsilon_{other} \tag{3}$$

where:

ρ_i … observed (measured) GNSS pseudorange from the *i*-th satellites, *c* … velocity of light (electromagnetic wave) in vacuum, b_{rec} … the (unknown) user GNSS receiver's clock error, $\varepsilon_{iono}(i)$ … GNSS pseudorange measurement error for *i*-th satellite due to ionospheric effects (delay and scintillation), $\varepsilon_{tropo}(i)$ … GNSS pseudorange measurement error for *i*-th satellite due to tropospheric effects (delay and scintillation), $\varepsilon_{multipath}(i)$ … GNSS pseudorange measurement error for *i*-th satellite due to multipath effects, ε_{other} … GNSS pseudorange measurement error due to the other (non-nevironmental) causes, R_i … actual GNSS pseudorange from the *i*-th satellites, expressed as in (4).

$$R_i = \sqrt{(x_{Si} - x_u)^2 + (y_{Si} - y_u)^2 + (z_{Si} - z_u)^2} \tag{4}$$

where:

(x_{Si}, y_{Si}, z_{Si}) … the position of the *i*-th satellite, derived from the orbital parameters given in navigation message, (x_u, y_u, z_u) … the (unknown) user position.

With error terms in (3) either neglected or supposedly corrected for the error effects using correction models that yields corrected GNSS pseudoranges ρ_{ci} (with the index *c* given to indicate correction), (3) and (4) form the GNSS position estimation model. Expanded to at least four independent simultaneously taken GNSS pseudorange observations (i = 1, …, n, $n \geq 4$), the model forms four non-linear equations system with four unknowns. The system may be transformed using Taylor series linearisation, after which it may be solved in the least-square iteration-based process (5) … (9), shown here for $n = 4$:

$$\begin{bmatrix} x_{k+1} \\ y_{k+1} \\ z_{k+1} \end{bmatrix} = \begin{bmatrix} x_k \\ y_k \\ z_k \end{bmatrix} + \begin{bmatrix} \Delta x \\ \Delta y \\ \Delta z \end{bmatrix}, \tag{5}$$

$$\begin{bmatrix} \Delta x \\ \Delta y \\ \Delta z \\ c \cdot b \end{bmatrix} = \begin{bmatrix} \frac{x_k - x_{S1}}{R_{1,k}} & \frac{y_k - y_{S1}}{R_{1,k}} & \frac{z_k - z_{S1}}{R_{1,k}} & 1 \\ \frac{x_k - x_{S2}}{R_{2,k}} & \frac{y_k - y_{S2}}{R_{2,k}} & \frac{z_k - z_{S2}}{R_{2,k}} & 1 \\ \frac{x_k - x_{S3}}{R_{3,k}} & \frac{y_k - y_{S3}}{R_{3,k}} & \frac{z_k - z_{S3}}{R_{3,k}} & 1 \\ \frac{x_k - x_{S4}}{R_{4,k}} & \frac{y_k - y_{S4}}{R_{4,k}} & \frac{z_k - z_{S4}}{R_{4,k}} & 1 \end{bmatrix} \cdot \begin{bmatrix} \rho_{c1} \\ \rho_{c2} \\ \rho_{c3} \\ \rho_{c4} \end{bmatrix} \tag{6}$$

$$R_{i,k} = \sqrt{(x_{Si} - x_k)^2 + (y_{Si} - y_k)^2 + (z_{Si} - z_k)^2}, \quad i = 1, \ldots 4, \tag{7}$$

$$\begin{bmatrix} x_{k+1} \\ y_{k+1} \\ z_{k+1} \end{bmatrix} = \begin{bmatrix} a \\ b \\ c \end{bmatrix}, \quad a \in \mathbb{R}, b \in \mathbb{R}, c \in \mathbb{R}, \tag{8}$$

$$\boldsymbol{G} = \begin{bmatrix} \frac{x_k - x_{S1}}{R_{1,k}} & \frac{y_k - y_{S1}}{R_{1,k}} & \frac{z_k - z_{S1}}{R_{1,k}} & 1 \\ \frac{x_k - x_{S2}}{R_{2,k}} & \frac{y_k - y_{S2}}{R_{2,k}} & \frac{z_k - z_{S2}}{R_{2,k}} & 1 \\ \frac{x_k - x_{S3}}{R_{3,k}} & \frac{y_k - y_{S3}}{R_{3,k}} & \frac{z_k - z_{S3}}{R_{3,k}} & 1 \\ \frac{x_k - x_{S4}}{R_{4,k}} & \frac{y_k - y_{S4}}{R_{4,k}} & \frac{z_k - z_{S4}}{R_{4,k}} & 1 \end{bmatrix}. \tag{9}$$

The solution is given as the user's state vector (10):

$$\overrightarrow{x_u} = (x_u, y_u, z_u, b)^{\mathrm{T}} \tag{10}$$

The least-square approach yields another model representing the GNSS pseudorange measurement error $\Delta\rho$ propagation into the GNSS positioning error Δx, as follows:

$$\Delta \boldsymbol{x} = (\boldsymbol{G}^{\mathrm{T}}\boldsymbol{G})^{-1}\boldsymbol{G}^{\mathrm{T}}\Delta\boldsymbol{\rho}. \tag{11}$$

Weights $\boldsymbol{R}^{-1}$ may be assigned to correct for several random errors (Filić, 2017a), (Gustafsson, 2010) in GNSS pseudorange observations. In that case, the Weighted Least-Square approach (Filić, 2017a) may be deployed that yields the GNSS pseudoranges error propagation model, as given in (12).

$$\Delta \boldsymbol{x} = (\boldsymbol{G}^{\mathrm{T}}\boldsymbol{R}^{-1}\boldsymbol{G})^{-1}\boldsymbol{G}^{\mathrm{T}}\boldsymbol{R}^{-1}\Delta\boldsymbol{\rho}. \tag{12}$$

2.3 *Comparative studies with GNSS SDR*. Transparency of the position estimation process within the GNSS SDR receiver renders it an invaluable research tool, capable of using any point in the process to enter the appropriate inputs (signals or data) to simulate behaviour and characteristics of the receiver as it would extend in real conditions (Filić, Filjar and Ruotsalainen, 2016). In that way, a GNSS SDR receiver may serve as a GNSS post-processing, or GNSS simulation tool, providing

the appropriate data or signals are presented as input. In particular case of available GNSS pseudorange observations taken with a dual-frequency receiver, such as those utilised in the IGS reference stations network, the ionospheric effects on GNSS positioning performance may be revealed using a simple and efficient procedure.

The comparative study aimed at revealing the impact of the ionospheric effects on GNSS positioning performance may benefit from creation of two sets of position estimates. One may utilise GNSS pseudoranges uncorrected for, and thus exposing the ionospheric effects. Another one may utilise dual-frequency correction of ionospheric effects, thus completely removing them. Correction of effects of the other potential error sources should be treated in the same way in both cases.

Time series of GNSS position estimation errors due to ionospheric effects may be derived using the model (13)

$$\begin{bmatrix} northing_{iono} \\ easting_{iono} \\ height_{iono} \end{bmatrix} = \begin{bmatrix} northing_{raw} \\ easting_{raw} \\ height_{raw} \end{bmatrix} - \begin{bmatrix} northing_{df} \\ easting_{df} \\ height_{df} \end{bmatrix} \tag{13}$$

where:
(northing, easting, height) … denotes the respective positioning errors in northing, easting, and vertical directions, index *iono* … denotes errors due to ionospheric effects; index *raw* … denotes error estimates obtained using GNSS pseudoranges uncorrected for ionospheric effects, index *df* … denotes error estimates obtained using GNSS pseudoranges with dual-frequency correction for ionospheric effects (ionospheric effects removed).

The comparative data sets may be created easily through the appropriate configuration of a GNSS SDR receiver, as depicted in Figure 4 using RTKLIB, an open-source GNSS SDR receiver.

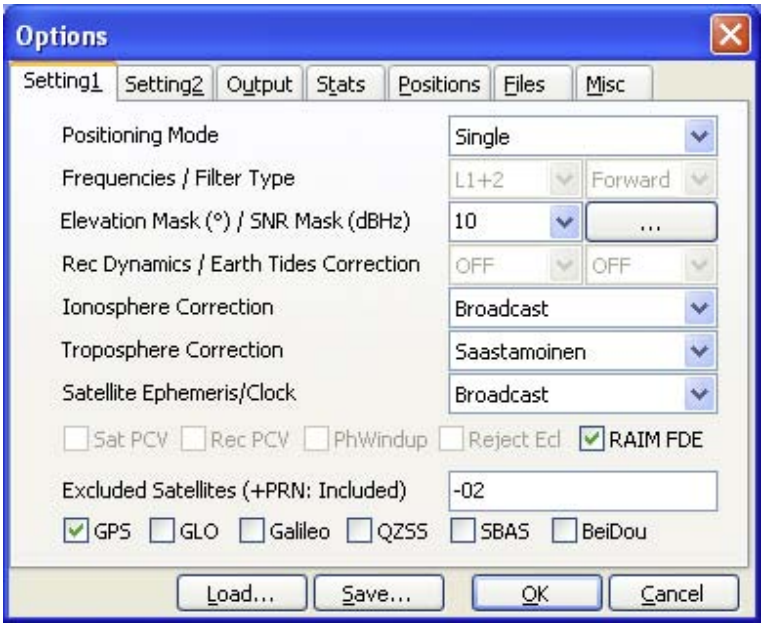

Figure 4. Configuration Graphical User Interface (GUI) of RTKLIB GNSS SDR receiver (Takasu, 2013)

Figure 5. The IGS reference station network (IGS, 2018)

2.4 *Data description*. The IGS reference stations network (IGS, 2018) (Figure 5) database of daily observation files was examined in the study. The NASA internet site for data access was used that provides the structure approach to data access. Number of GPS (RINEX o and files), GLONASS (RINEX g files), and Galileo (RINEX l files) raw pseudorange observation files in the daily basis was counted, along with the number of supplied navigation message RINEX files of GPS (RINEX n files), and multi-GNSS (RINEX p files, containing navigation messages in a single file of all four major GNSSs: GPS, GLONASS, Beidou and Galileo). The availability of meteorological observations (RINEX m files), required for tropospheric positioning environment reconstruction, was examined as well. Database examination covered time interval between 1 September (DOY244) and 15 September (DOY258) in 2017, encompassing the largest single ionospheric disturbance in the year observed.

2.5 *Scenarios of utilisation*. GNSS positioning performance is commonly assessed from the perspective of potential GNSS utilisation. Such an approach is required for determination of GNSS-based applications (services and systems) quality. It allows for assessing and modelling the GNSS utilisation risk in GNSS-founded applications. (Thomas *et al.,* 2011) presented a comprehensive classification of GNSS applications, and assigned qualitative level of the GNSS accuracy requirement to every one of them.

The GNSS positioning performance assessment may be conducted from the positioning environment perspective, the approach taken in this study. During the preparatory phase (pre-processing of GNSS pseudoranges) in the navigation (application) domain, observed GNSS pseudoranges are corrected for the (known) systematic influence of ionosphere, troposphere and satellite clock errors (Luo, 2013). Additional measures are commonly introduced to mitigate potential multipath effects, in most cases without the prior detection of multipath conditions. The procedure yields GNSS pseudoranges corrected for systematic errors, but still compromised with stochastic (random) errors and uncorrected systematic errors that cannot be predicted with correction models (Gustafsson, 2010, Luo, 2013). The extent of uncorrected stochastic errors within GNSS pseudoranges determines resulting GNSS positioning error, and therefore the GNSS positioning performance. GNSS positioning performance assessment focuses on the three most prominent performance environment scenarios: (1) ionospheric scenario, (2) tropospheric scenario, and (3) multipath scenario.

The ionospheric effects emerge as a consequence of GNSS signal (radio wave) propagation in ionised media (Davis, 1990, Parkinson and Spilker Jr, 1996). It consists of the ionospheric delay and ionospheric scintillation, with former corrected for systematic errors using the appropriate models. The extent of the ionospheric scintillation effect on GNSS positioning performance is usually negligible in mid-latitudes. Single frequency GNSS receivers, with the exception of Galileo, use the Klobuchar model (Parkinson and Spilker Jr, 1996), an 8-parameters model based on presumption of a flat night-time GNSS ionospheric delay and a cosine-like ionospheric delay dynamics during the daylight period. Galileo uses its own climatological NeQuick model, developed by S M Radicella, and B Nava (European Commission, 2016).

The GNSS positioning performance studies examine the effects of various levels of space weather, geomagnetic and ionospheric disturbances, ranging from quiet conditions to massive storms, as a positioning environment conditions scenario of GNSS utilisation. Research has been conducted to model space weather conditions (Zolesi and Cander, 2014), and the space weather - GNSS positioning performance coupling across the chain involving: space weather, geomagnetic field, ionosphere, ionospheric delay, GNSS positioning error (Filić, 2018, Filić and Filjar, 2018a, Filić and Filjar, 2018b, Filić, 2017b). In a reverse engineering-sense, the IGS data was demonstrated as a foundation for a simulator of GNSS ionospheric positioning environment (Filić, Filjar and Weng, 2018).

Tropospheric impact on GNSS positioning performance arises from effects of GNSS signal (radio wave) propagation in non-ionised media (air) (Parkinson and Spilker Jr, 1996, Reguzzoni, 2013). Tropospheric effects appear as either signal delay, or tropospheric scintillation, with the latter being far less pronounced than in the ionospheric scenario. GNSS receivers commonly mitigate tropospheric effects with utilisation of the Saastamoinen model (Parkinson and Spilker Jr, 1996), usually with the input data taken from the standard model of atmosphere, instead of the actual meteorological observations. While being less influential on GNSS positioning performance, tropospheric effects may cause noticeable effects during considerable weather deteriorations (Rumora *et al.,* 2018).

GNSS positioning performance assessment studies focus on effects of fast weather deterioration, passage of cold and warm fronts, and massive tropospheric storms on GNSS positioning performance for particular classes of GNSS applications.

The multipath scenario accounts for the effects of local positioning environment, behind the outreach of the GNSS system. Due to the entirely stochastic nature of multipath effects (Parkinson, and Spilker Jr, 1996, Hannah, 2001, Faragher, 2007), the core GNSS system cannot provide mitigating assistance to GNSS user equipment. However, uncompensated multipath effects may considerably degrade GNSS positioning performance, rendering it an important scenario to study.

Character of the multipath effects varies widely across particular positioning environments (indoors, urban, mountains, marine) impedes development of generalised model. GNSS positioning performance studies aim at detection and statistical description of various classes of multipath effects, as well as their applications as correction models for targeted GNSS applications (Rumora, Sikirica and Filjar, 2018).

3. IGS DATA AVAILABILITY

Two-weeks interval in September 2017 was selected for the study, which encompasses the encounter with the most powerful ionospheric disturbance in the year observed. The over-all availability of daily RNEX observations, commonly required for GNSS positioning performance studies in various positioning conditions and different application scenarios, was assessed, with the results presented in this Section.

Table 1 presents a summary of exploratory statistical analysis of related GNSS observations. Box-and-whiskers plots of RINEX d, g, l, and m files (Figure 6), and o, and p files (Figure 7) are presented, respectively, showing variations of stability of data provision.

Table 1. Exploratory statistics of GNSS observations availability in the time interval observed

	RINEX d	RINEX g	RINEX l	RINEX m	RINEX n	RINEX o	RINEX p
mean	514.5	268.6	26.7	91.6	388.8	514.5	0
median	516	268	27	92	391	516	0
st dev	7.4	3.0	0.5	1.2	7.2	7.4	0

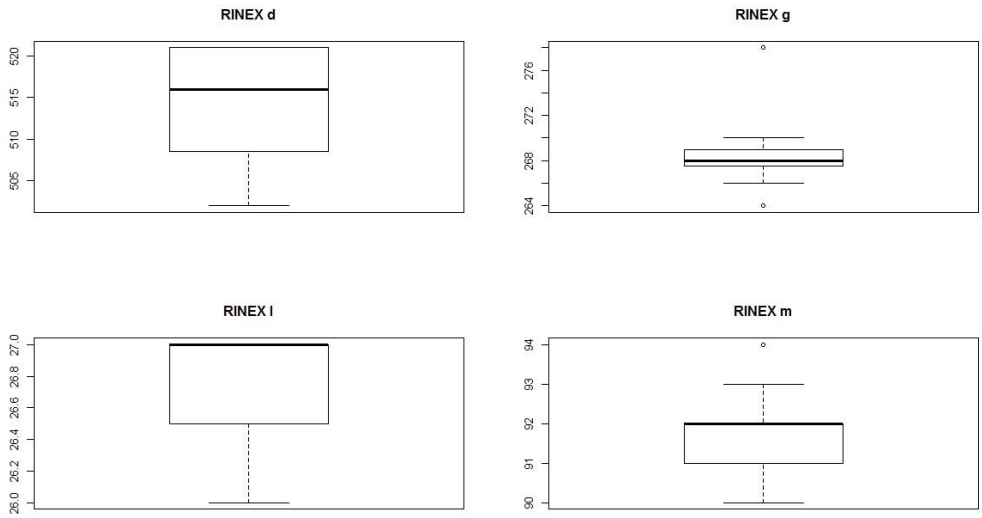

Figure 6. Box-and-whiskers plots of the counts of RINEX d (GPS), RINEX g (GLONASS), RINEX l (Galileo), and RINEX m (meteorological conditions) daily observation files

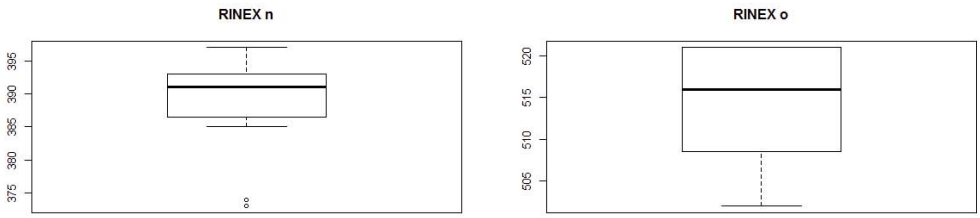

Figure 7. Box-and-whiskers plots of the counts of RINEX n (GPS), RINEX o (GPS) daily observation files (RINEX p files) were not detected during the interval observed)

4. DISCUSSION

Study results reveals the status of, and initiates several recommendations on the ICG data improvements to suit wider range of GNSS positioning performance assessment. The IGS network and service provide an invaluable source of raw dual-frequency multi-GNSS (at various levels) GNSS observations uncorrected for ionospheric effects.

Provision of raw GPS pseudorange observations (RINEX d and o files) is stable, with minor variations, presumably caused by local maintenance, and rare local and systematic effects.

GLONASS pseudorange observations (RINEX g files) are provided to the far less extent, compared with the provision of GPS pseudoranges. Approximately half of the IGS reference stations that provide GPS pseudoranges report the GLONASS ones as well. However, the provision is even more stable stable than in case of GPS pseudoranges, with prevailing majority of stations providing GLONASS pseudoranges seamlessly.

Only 5 % of the IGS reference stations report Galileo pseudoranges continuously. While variation in data provision is very low, it is expected that the contribution will raise with the introduction of new Galileo satellites.

GNSS positioning performance assessment in two remaining scenarios of positioning environment are far less supported by the IGS. As the result of our experience from various previous studies, including (Rumora *et al.,* 2018) and (Rumora, Sikirica and Filjar, 2018), the IGS data consist of GNSS pseudoranges of unsustainable mitigation quality levels. Since all the IGS reference stations try to mitigate tropospheric and multipath using non-standardised approaches and methods, the IGS pseudorange observations are inconsistently corrected for related effects. As the result, it is possible to find data sets almost uncorrected for tropospheric and multipath effects. On the less bright side, some IGS stations report GNSS pseudoranges that are corrupted with low-quality or inappropriate tropospheric and multipath corrections. Since details are not immediately visible, a researcher must examine the reference station equipment description in detail, and perform initial data analysis to identify data set suitable for his or her research. Additionally, slightly less than 20 % of the IGS stations report meteorological data continuously, thus reducing the IGS database as a source of data for troposphere-related GNSS positioning performance assessment.

Finally, the IGS database is an invaluable source of multi-GNSS observations (Ren, 2016). Considering its in-the-field operation on the voluntary basis essentially, one cannot complain about prevalence of GPS observations, compared with the contribution percentage of the other systems' pseudoranges. Contributors provide whatever they have at hand and can afford. Their effort and results should be appreciated and applauded. Situation is going to improve with fall of the multi-GNSS receiver prices. The IGS operators should consider extending support for

multi-GNSS studies with the aggregation of observed multi-GNSS messages in single daily RINEX p files. Such an improvement will not only foster the multi-GNSS positioning performance research, but will allow for research in GNSS spoofing segment, another very important subject. Provision of original (broadcast) navigation messages, and those observed in the field will allow for research in detection, classification and mitigation observed GNSS spoofing cases, providing those are not suppressed by defence algorithms deployed in GNSS equipment.

The organisation of observation collection, monitoring network operation and provision of advanced services based on experimental data as detailed by the IGS should be seen as a template for similar voluntary (crowdsourcing) initiatives. Modern smartphones are almost entirely multi-GNSS-based, with the support of reception GPS and GLONASS signals, at least. Recent advancement in proprietary Google Android Location API allows for direct collection of raw GNSS pseudoranges from devices everyone uses today (Filić and Filjar, 2018c, GSA GNSS Raw Measurements Task Force, 2017). We see an exceptional research opportunity for voluntary data collection on the international basis in more variety of positioning environments without any corrections applied, since neither ionospheric, nor tropospheric and multipath corrections are applied. In the most recent developments, smartphone manufacturers have started to equip devices with dual-frequency multi-GNSS receivers. We expect the proliferation of such devices and an enormous opportunity for massive data collection that will describe various positioning environment conditions in more detail. We argue that the systematic approach developed by the IGS should be considered for deployment on smartphone observation collection initiative.

5. CONCLUSION

The International GNSS Service (IGS) network of stationary GNSS reference receivers is an invaluable source of continuously and systematically collected raw GNSS pseudorange observations. Initially established as a data source for studies on ionospheric effects on GNSS positioning performance, the IGS data allows for GNSS positioning performance assessment in selected positioning environment conditions and for selected utilisation scenarios. Massive GNSS observations sets are freely available for scientists, engineers, GNSS receiver manufacturers, GNSS-related services developers and operators, strategists, regulators and general public for non-commercial studies.

Here we selected and examined a set of the IGS GNSS observations, with prospects for utilisation for GNSS positioning performance assessment using our methodology, proposed here. Additionally, we challenged the quest for data availability and quality for a GNSS positioning performance study by examining the most popular and populous GNSS pseudorange databases for potential utilisation in three characteristic scenarios of positioning performance assessment: ionosphere, troposphere and multipath. We examined data availability (i. e. GNSS pseudorange existence in a database) and quality (i. e. the existence of positioning environment descriptors) for those scenarios in spatio-temporal domain (i. e. across the globe, and throughout the day) according the scenario-specific criteria. The exploratory statistical analysis was performed in the R environment for statistical computing (R project team, 2018) to provide a clear description of data availability and quality for GNSS positioning performance studies, emphasising shortcomings in data format and structure, as well as gaps in data availability. In addition, support for multi-GNSS studies was examined, and recommendations proposed to render available data more suitable for multi-GNSS positioning performance assessment studies. The findings were used for suggestions and recommendations for improvements, with the aim to render GNSS pseudorange data pools more attractive to scientists and engineers for their GNSS resilience development studies.

References

Cannon, P. et al. (2013). *Extreme space weather: impacts on engineered systems and infrastructure*. London: Royal Academy of Engineering. Available at: http://bit.ly/11OdBNN.

Davis, K. (1990). *Ionospheric Radio*. London: Peter Peregrinus Ltd.

Efron, B. and Hastie, T. (2016). *Computer Age Statistical Inference: Algorithms, Evidence and Data Science*. Cambridge: Cambridge University Press.

European Commission. (2016). *European GNSS (Galileo) Open Service. Ionospheric Correction Algorithm for Galileo Single Frequency Users*. Bruxelles: European Commission.

Faragher, R. M. (2007). *Effects of Multipath Interference on Radio Positioning Systems*. Cambridge: Churchill College, University of Cambridge.

Filić, M. (2018). On development of the forecasting model of GNSS positioning performance degradation due to space weather and ionospheric conditions. *Proc 2nd URSI Atlantic Radio Science Conference*. Gran Canaria, Canary Islands, Spain. Available at: https://bit.ly/2K1lJDv.

Filić, M. and Filjar, R. (2018a). *Forecasting model of space weather-driven GNSS positioning performance*. Riga: Lambert Academic Publishing. ISBN 978-613-9-90118-0.

Filić, M. and Filjar, R. (2018b). Modelling the Relation between GNSS Positioning Performance Degradation, and Space Weather and Ionospheric Conditions using RReliefF Features Selection. *Proc of 31st International Technical Meeting ION GNSS+ 2018*. Miami, FL.

Filić, M. and Filjar, R. (2018c). Smartphone GNSS positioning performance improvements through utilisation of Google Location API. *Proc of 41 st International Convention MIPRO/CTI*. pp. 507–510. Opatija, Croatia.

Filić, M., Grubišić, L. and Filjar, R. (2018). Improvement of standard GPS position estimation algorithm through utilization of Weighted-Least-Square Approach. *Proc of 11th Annual Baška GNSS Conference*. pp. 7–18. Baška, Krk Island, Croatia. Available at: https://bit.ly/2sLuR82.

Filić, M., Filjar, R. and Ševrović, M. (2018). Expression of GNSS Positioning Error in Terms of Distance. *Promet – Traffic & Transportation*. 30(3). pp. 305–310. doi: 10.7307/ptt.v30i3.2304. Available at: https://bit.ly/2z2pOX2.

Filić, M., Filjar, R. and Weng, J. (2018). An IGS-based simulator of ionospheric conditions for GNSS positioning quality assessment. *Coordinates*. Feb 2018. pp. 31–34. Available at: http://mycoordinates.org/an-igs-based-simulator-of-ionospheric-conditions-for-gnss-positioning-quality-assessment/.

Filić, M. (2017a). *Analysis of the position estimation procedure based on given GNSS pseudoranges in a GNSS SDR receiver*. Master Thesis (in Croatian). Zagreb: Faculty of Science, University of Zagreb. Available at: https://zir.nsk.hr/islandora/object/pmf%3A3230.

Filić, M. (2017b). A comparative study of forecasting methods for space weather-caused GNSS positioning performance degradation. *Invited lecture at UN/USA Workshop on the International Space Weather Initiative*. Boston College. Chestnut Hill, MA.

GSA GNSS Raw Measurements Task Force. (2017). *Using GNSS raw measurements on Android devices (white paper)*. Prague: European GNSS Agency. Available at: http://bit.ly/2BiQ4s2.

Gustafsson, F. (2010). *Statistical Sensor Fusion (2nd ed)*. Linkoepping: Studentlitteratur AB.

Hannah, B. M. (2001). *Modelling and Simulation of GPS Multipath Propagation*. Doctoral Dissertation. Queensland: Queensland University of Technology.

Hapgood, M. (2017). Satellite navigation – Amazing technology but insidious risk: Why everyone needs to understand the space weather. *Space weather*. 15. pp. 545–548. doi:10.1002/2017SW001638.

IGS. (2018). International GNSS Services – Data archive (internet site operated and maintained by NASA). Available at: ftp://cddis.gsfc.nasa.gov/gnss/data/daily.

Luo, X. (2013) *GPS Stochastic Modelling: Signal Quality Measures and ARMA Processes*. Heidelberg: Springer Verlag.

Nguyen, T. Q. (2007). Efficient GPS position determination algorithms. Air Force Institute of Technology. Wright-Patterson AFB, OH.

Oxley, A. (2017). *Uncertainties in GPS positioning: a mathematical discourse*. London: Academic Press/Elsevier.

Parkinson, B. W. and Spilker, Jr, J. J. (1996). *Global Positioning System: Theory and Applications (Vol. I.)*. Washington, DC: AIAA.

R-project team. (2018). *The R project for Statistical Computing (software, documentation, and monographs)*. Available at: https://www.r-project.org.

Reguzzoni, I. (2013). *GPS tropospheric delay for meteorological applications*. Master Thesis. Milan: Politechnico di Milano.

Ren, X. *et al*. (2016). Global Ionospheric Modelling using Multi-GNSS: BeiDou, Galileo, GLONASS and GPS. *Sci Rep*. 6. 33499. doi: 10.1038/srep33499.

Rumora, I., Jukić, O., Filić, M. and Filjar, R. (2018). A study of GPS positioning error associated with tropospheric delay during Numa Mediterranean cyclone. *Int J for Transp and Traff Eng*. 8(3). pp. 282–293. doi: 10.7708/ijtte.2018.8(3).03.

Rumora, I., Sikirica, N and Filjar, R. (2018). An Experimental Identification of Multipath Effect in GPS Positioning Error. *TRANSNAV Journal*. 12(1). pp. 29–32. doi: 10.12716/1001.12.01.02. Available at: http://www.transnav.eu/Article_An _Experimental_Identification_Rumora,45,783.html.

Sadlier, G. *et al*. (2017). *The economic impact on the UK of a disruption to GNSS*. London: London Economics. Available at: https://bit.ly/2zJ9GXh.

SaPPART. (2017). SaPPART Handbook: Assessment of positioning performance in ITS applications. COST Action TU1302 Satellite Positioning Performance Assessment for Road Transport. Marne-la-Vallee, France.

Stewart, W. *et al*. (2015). *Software Defined Radio using MatLab & Simulink and the RTL-SDR*. Glasgow: University of Strathclyde.

Takasu, T. (2013) RTKLIB: An Open-Source Program Package for GNSS Positoning – Software and Documentation. Available at: http://www.rtklib.com.

Thomas, M. *et al*. (2011) *Global navigation space systems: reliance and vulnerabilities.* London: The Royal Academy of Engineering.

UK Government Office for Science. (2018). Satellite-Derived Time and Position: A Study of Critical Dependencies. HM Government of the United Kingdom and Northern Ireland. Available at: https://bit.ly/2E2STnd.

Zolesi, B. and Cander, Lj. R. (2014). *Ionospheric Prediction and Forecasting*. Springer Verlag. Berlin and Heidelberg, Germany.

Sveučilište u Rijeci
POMORSKI FAKULTET
FACULTY OF MARITIME STUDIES
University of Rijeka

University of Zagreb
Faculty of Transport and Traffic Sciences

Royal Institute of Navigation
Science Technology Practice

12th Annual Baška GNSS Conference

ON LONG-TERM SOLAR ACTIVITY IMPACT ON GPS SINGLE-FREQUENCY 3D POSITIONING ACCURACY IN THE ADRIATIC REGION

Ivan Toman[1], Serdjo Kos[2], David Brčić[2]

[1] University of Zadar, Department of Nautical Studies, Zadar, Croatia
e-mail: itoman@unizd.hr (Corresponding author)

[2] University of Rijeka, Faculty of Maritime Studies, Rijeka, Croatia

Abstract

The Sun acts as the main driver of processes affecting the Earth's ionosphere, directly and indirectly influencing the Global Navigation Satellite System (GNSS) signals' timing measurements. Solar impacts can be categorized according to different timescales that are short-lasting (regarding minutes during solar events), diurnal, seasonal (yearly) and perennial, covering the duration of the solar cycle. The proposed paper deals with seasonal and solar cycle and its impact on Global Positioning System (GPS) single-frequency (L1) positioning accuracy. Solar activity was analyzed during 17 years of available observation data. For this purpose, Sunspot Number (SSN) and Daily Solar Flux 10.7 cm (SFD) were analyzed. Indices were compared with GPS three-dimensional positioning deviations calculated on three locations in the broader region of the Adriatic Sea. Positioning data were calculated as single frequency solutions, obtained from the International GNSS Service (IGS) Receiver INdependent EXchange (RINEX) data. A significant correlation has been found between positioning accuracy and elaborated indices, both with and without the employment of standard ionospheric correction model, as presented. The emphasis was given on un-modelled positioning solution or errors, respectively, to employ a GPS receiver as a partial solar activity indicator. Besides solar cycle related period, seasonal positioning deviations were analyzed in the frame of the

Local Equatorial Coordinate System (LECS) with declination and hour angle as main coordinates. Detectable positioning error increase has been observed during periods of positive Sun declination (in Northern hemisphere), based on the scenario of 4 consecutive years within the elaborated period. Obtained results rendered the possibility of predictive modelling of the GPS L1 positioning error. For this purpose, the elastic net regression method was used, employing SSN and SFD indices as predictors. Results are presented and discussed, with observations and findings summarized in the concluding chapter, together with the desirable continuation of the research.

Keywords: *solar cycle, seasonal variations, ionospheric delay, 3D GPS positioning accuracy, local equatorial coordinate system, predictive modelling, Adriatic region*

1. INTRODUCTION AND BACKGROUND

The ionosphere is a compound of several ionized layers of Earth's atmosphere at altitudes from approximately 60 to 1000 km, where free electrons affect the propagation of radio waves (IEEE, 1998). Prominent effects on GNSS signal delay mostly occur within F2 layer which forms at heights of approximately 200-300 kilometres from the Earth surface (Klobuchar, 1987, Goodman, 2005). There are various cycles associated with solar radiation changes that reach ionospheric layers: diurnal cycles, seasonal cycles, solar activity cycles and disturbances/events, all of them acting as causes of satellite positioning degradation.

The effect of the Total Electron Content (TEC) on time measurements of signal transfer from satellite to the receiver (ionospheric delay) is expressed as (Klobuchar, 1987):

$$t = \frac{40.3}{3 \times 10^8} \times f^2 \int N dl \tag{1}$$

where: f ... system operating frequency and N ... the number of electrons along the signal path.

Kumar *et al.* (2012) researched TEC variability by analysing dual frequency GPS signals recorded at several Indian locations. They found a diurnal variation of TEC around with maximum values half an hour after noon and minimum before dawn. During equinox season maximum and minimum TEC has been found during winter and summer, respectively. During the night, and hemisphere winter, ionosphere

strength is lower because of lower amounts of received energy, either by being shaded by Earth during the night, or at an unfavourable angle of incidence during winter. As for ionospheric refraction, the physical path of the satellite signal differs from Euclidian direct geometrical path. According to Fermat's principle (Feynman, Leighton and Sands, 2011), satellite signal ray propagates between two points along the shortest path between the satellite (*S*) and the receiver's (*r*) antenna (Petrovski and Tsujjii, 2012, Subirana, Zornoza and Hernandez-Pajares, 2013):

$$l = \int_r^s n dl \tag{2}$$

where: l ... the shortest ray path and n ... refractivity index.

Satellite positioning signal delay can, therefore, be expressed as (Subirana, Zornoza and Hernandez-Pajares, 2013):

$$\Delta = \int_r^s n dl - \int_r^s dl. \tag{3}$$

The second integral represents a resulting distance between satellite and user's antenna – the pseudorange.

The described effect causes ranging measurement error between GNSS satellite and receiver, leading to error position estimation. On a worst-case basis, signals can be retarded by more than 300 ns, which correspond to the range of positioning error of 100 meters (Klobuchar, 1987). The ionospheric delay caused by ionospheric refraction is still subject of ongoing research. Standard GPS ionospheric (Klobuchar) correction model eliminates approximately 50-70 % of error using eight solar activity coefficients transmitted as a part of the navigational message (Bent, Llewellyn and Walloch, 1972, Kobuchar, 1978).

During periods of increased solar activity, ionospheric variations are more pronounced as well, leading to less accurate pseudorange measurements and finally increased satellite positioning error. The proposed paper elaborates long-term solar activity influence on GPS 3D positioning error, namely solar and seasonal cycles. In the following text, solar indices used for the study are described, as well as parameters related to the position of the Sun relative to Earth, related to seasonal cycle variations. The methodology of conducted research comprising all elements is presented. The correlation between positioning solutions/errors and mentioned

indices is presented, results of which are discussed regarding two employed scenarios: by determination of positioning solutions *i)* with and *ii)* without employment of the Klobuchar model. Based on findings, an experimental modelling of GPS 3D positioning error was conducted, as shown in the appropriate chapter. Results are presented and discussed in the concluding chapter, together with activities emerged from the proposed research.

2. LONG-TERM SOLAR ACTIVITY RELEVANT INDICATORS

Sporadic historical observations of sunspot data can be found all the way back to B.C. (Clark and Stephenson, 1978), with reliable data archived from 1610 (Hathaway, 2010). However, available systematic observations date from 1818 at NOAA public server (NOAA, 2018)

It is considered that relevant indices of solar activity are the sunspot number (SSN), sunspot areas, solar radio flux 10.7 cm (SFD) and total solar irradiance (Hathaway, 2010). Most relevant index describing solar activity based on a count of a number of sunspots on the solar disk is given by relationship (Goodman, 2005):

$$R = k \cdot (10g + s) \tag{4}$$

where: k ... correction factor dependent upon the specific observatory, g ... a number of sunspot groups and s ... number of individual spots.

Sunspot numbers vary with time in solar cycle periods. Average duration of one solar cycle is 11 years with a standard deviation of 14 months (Hathaway, 2010). There are 24 recorded solar cycle periods to date, with first cycle recorded in February 1755. Cycles are dynamically characterized by their maximum and minimum, periods and amplitudes, shapes and other features. Particular cycle characteristics are periodically variable as well, both in short and long term (Hathaway, 2010). Methods to predict solar activity exists; however they are not precise, especially in the long term (Goodman, 2005).

Wavelength of 10.7 cm solar density flux is one of the most widely used indices of solar activity. Wavelengths in a region of 10 cm are the best for monitoring the level of solar activity because solar emissions at these wavelengths are very sensitive to conditions in the solar upper chromosphere and at the base of the corona. Solar flux

measurement of 10.7 cm is a determination of the strength of solar radio emission averaged over an hour and expressed in solar flux units (sfu) where 1 sfu = 10^{-22} Wm^{-2} Hz^{-1} (Tapping, 2013). Sunspot number and solar radio flux are most frequently used to describe the long-term solar activity (Li *et al.*, 2014). These indices were used as analysed indices in the proposed research.

3. LOCAL EQUATORIAL COORDINATE SYSTEM

The equatorial coordinate system is mostly used to describe positions of celestial bodies, with the origin projected at the centre of the Earth. Two planes are defined; Earth's equator projection to celestial sphere defines celestial equator and observer's meridian projection to celestial sphere defines celestial meridian. Celestial body's position is determined by measuring two angles respective to those planes. Declination is coordinate defined as an angle measured at the origin, between celestial equator and the celestial body. Local hour angle is an angle measured at the between celestial meridian and celestial body (Figure 1). While declination describes the angular distance from Earth's equator in the north-south direction, local hour angle describes the angular distance from observer meridian in the east-west direction (Vallado, 2001).

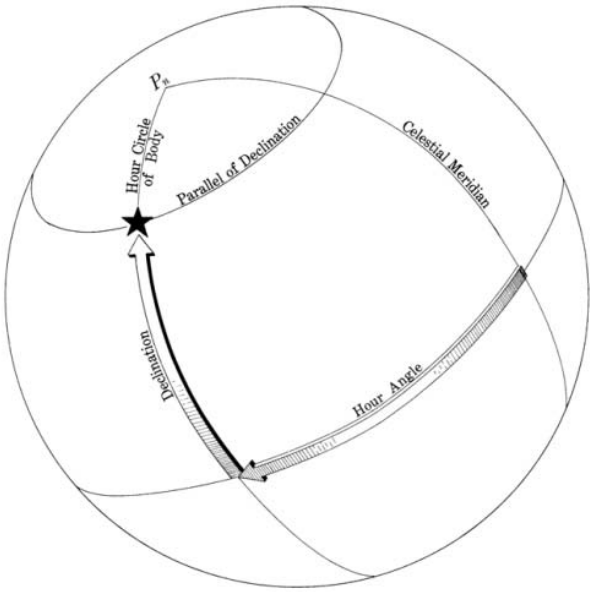

Figure 1. Local Equatorial Coordinate System (Wikimedia, 2018)

LECS coordinates are given as (Lipovac, 1981):

$$\partial = -23.45° \cdot \cos\left(\frac{360}{365} \cdot (d + 10)\right) \tag{5}$$

where: ∂ ... the Sun declination and d ... day of the year. The local hour angle (LHA) of the observer is given as:

$$LHA = LST - \alpha \tag{6}$$

where: LST ... the local sidereal time and α ... is the right ascension of the observer (Lipovac, 1981). Due to long-term features of data and the proposed study, the declination coordinate was further analysed.

4. METHODOLOGICAL APPROACH

The methodology of the conducted research comprises of *i)* selection of the elaborated period, *ii)* selection of IGS stations and respective data needed to determinate GPS positioning solutions, *iii)* selection and analyses of solar indices, *iv)* calculation of GPS positioning solutions and positioning errors, *v)* formulation of correlations between respective indices/parameters and *vi)* approach to predictive modelling of positioning error in function of solar activity indices.

4.1 *IGS stations (area), the period of interest and solar activity data*. The IGS (International GNSS Service) is a service of the International Association of Geodesy with the primary goal of supporting scientific research based on highly precise and accurate Earth observations using GNSS technologies (Dow, Neilan and Rizos, 2009). More than 200 organisations in more than 100 countries are participating in IGS, providing access to data sets of more than 400 worldwide reference stations (IGS, 2018). Basic properties for analyzed stations are given in Table 1 (IGS, 2018).

Table 1. General properties of IGS stations corresponding products of which were used for the study

Station name	Country	Latitude [°]	Longitude [°]	Height ASL [m]
Graz	Austria	47.0671000	15.4935000	538.3
Medicina	Italy	44.5199000	11.6468000	50.0
Ohrid	Macedonia	41.1273056	20.7940556	773.0

Solar activity data were obtained from the NOAA public web server (NOAA 2018), with SSN and SFD indicators archived as daily indices. The period of 17 years was determined according to the availability of GPS positioning data provided by the IGS network, products of which were analyzed.

Although the availability of IGS data ranges from 1993, they were not adequate for the study before 1st of May 2000 due to active Selective Availability-generated error (US DOD, 2007). Due to this limitation, the arbitrary starting date of 1st January 2001 was selected.

Besides mentioned stations, IGS Padua (Italy) has been used in the study as it is located within the elaborated geographical area. However, historical record of that station does not cover years before 2002, containing a certain amount of erratic data as well. Therefore, this station was not analysed further.

4.2 *Calculation of positioning errors.* Archived RINEX observational and navigational files were collected from the IGS network (IGS, 2017) for stations Graz, Medicina and Ohrid, for the period 2001 – 2018. Single-frequency daily positioning solutions were created using RTKLIB software, an open source program package for GPS positioning (Takasu, 2018). Resolution frequency was set to 30s with mask angle of 15°. The total number of 17920 positioning solutions/days was made for three elaborated locations for each of ionospheric scenarios, i.e. Klobuchar- modelled and un-modelled positioning solutions.

For each 30 s timing in derived positioning dataset, two errors were calculated. The horizontal error was determined as the spherical distance between true and calculated station position, whereas vertical distance error was calculated as a vertical distance between true and calculated station elevation, as follows. For horizontal distance, haversine method was used:

$$h_{err} = 2r \arcsin \sqrt{sin^2\left(\frac{lat_c}{lat_t}\right) + \cos(lat_t)\cos(lat_c)sin^2\left(\frac{lon_t - lon_c}{2}\right)} \quad (7)$$

where: r... radius of the Earth, chosen as $6367 \cdot 10^3$ m, an approximate mean value between Equatorial and polar radius, which should be very close to correct value as area of interest lies at approximately 45° of latitude. Differences made by this error are less significant for this type of research. Even the Euclidian geometric method could also be used with sufficient accuracy due to small positioning error distances. The calculated latitude of specific IGS station derived from RINEX files is denoted as lat_c, while lat_t is the reference latitude. Similarly, lon_t and lon_c are the reference and calculated IGS station longitudes. The equation returns horizontal distance h_{err} of calculated position from the true station position in meters, or horizontal positioning error. Vertical distance or vertical positioning error is calculated as:

$$v_{err} = hgt_t - hgt_c \quad (8)$$

where: hgt_t... true station elevation (height above sea level) and hgt_c... is calculated elevation from RINEX files. Three-dimensional positioning error was calculated from horizontal and vertical errors as follows:

$$err = \sqrt{h_{err}^2 + v_{err}^2}. \quad (9)$$

4.3 *Formulation of correlations*. To correlate obtained positioning results with solar activity, data frequency matching was performed. Frequency of positioning error observables data has been resampled to daily mean value of all recorded observations.

As long-term effects of 11-year solar cycles were studied, day-to-day variations in data were considered to be noisy and filtered out. To perform data smoothing, rolling mean function was introduced on all data before calculating correlation with the same window of 365 days. From there, the Pearson correlation coefficient was calculated, and data were visualized for all stations and both for position calculation with and without GPS ionospheric correction applied. Also, mean positioning error values and mean standard deviation values were calculated for each scenario. Pearson correlation coefficient is calculated as (Rodgers and Nicewander, 1988):

$$r[x,y] = \frac{N\sum xy - \sum x \sum y}{\sqrt{[N\sum x^2 - (\sum x)^2][N\sum y^2 - (\sum y)^2]}} \tag{10}$$

where: x,y ... correlation variables. In this case, those are positioning errors and each of two solar indices, respectively.

4.4 *Positioning error predictive modelling.* Data have been modelled to find regression between SSN and SFD as predictors and positioning error as a dependent variable. Data has been modelled using various machine learning algorithms/ regression models. After testing model predictions, it was found that the linear regression model ElasticNet returns the most accurate results for the given data set. The ElasticNet is a regularized regression method used in statistics for fitting of linear or logistic regression models, proposed by Zou and Hastie (2005).

It has been shown that similar former methods (e.g. lasso method) are not an ideal choice when a significant correlation exists between different model predictors, what is the case of this research. The sunspot number and solar flux are highly correlated variables. In such a case, lasso tends to select only one predictor variable and ignore other correlated variables. ElasticNet regularization technique can select groups of correlated variables. In the case of SSN and SFD, the model treats those variables as a predictors group. The model estimates are given by the following theorem (Zou and Hastie, 2005):

$$\widehat{\boldsymbol{\beta}} = \underset{\boldsymbol{\beta}}{\operatorname{argmin}}\, \boldsymbol{\beta}^T \left(\frac{\boldsymbol{X}^{\mathrm{T}}\boldsymbol{X} + \lambda_2 \boldsymbol{I}}{1+\lambda_2} \right) \boldsymbol{\beta} - 2\boldsymbol{y}^{\mathrm{T}}\boldsymbol{X}\boldsymbol{\beta} + \lambda_1 |\boldsymbol{\beta}|_1 \tag{11}$$

where: $\boldsymbol{X},\boldsymbol{y}$ ... data, λ_1, λ_2 ... penalty terms, and T ... transpose operator.

SSN and SFD daily values were used as model features (input) and mean 3D positioning error daily values from observed IGS stations were used as the model response (output). For each tested model, train/test split with 70/30 percent ratio has been used to test model's coefficient of R^2 determination, which is here used as a measure of how well regression function fits the data. It is calculated as

$$R^2 = 1 - \frac{SSE}{SST} \tag{12}$$

where: SSE ... sum of squared errors for regression function and SST ... a sum of squared errors for dataset mean value.

5. 3D POSITIONING ERRORS IN CORRELATION WITH SOLAR CYCLE

When ionospheric correction is not applied, the results showed a very strong correlation between both solar indices (SSN and SFD) and calculated three-dimensional positioning errors, as shown on the following Figures. A somewhat lower however significant correlation was observed when ionospheric correction is applied.

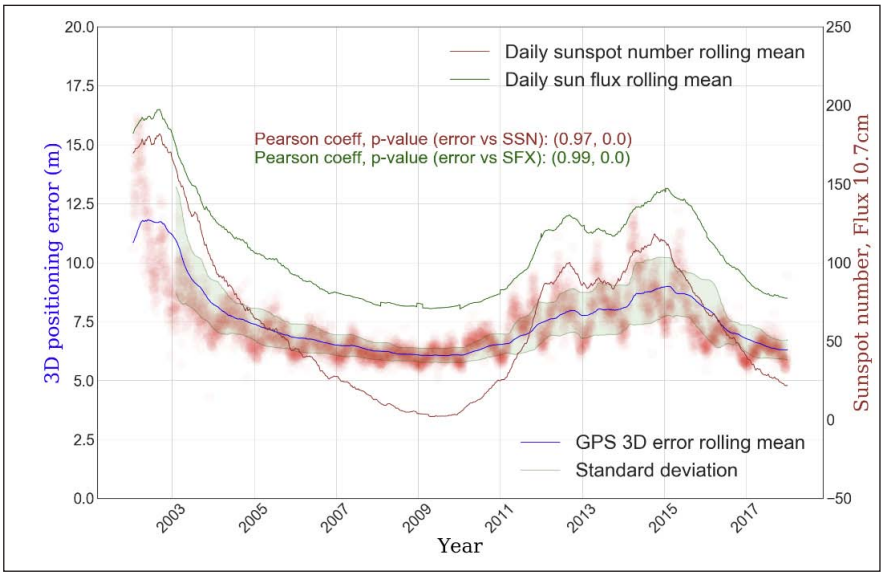

Figure 2. GPS 3D positioning error vs solar activity (SSN and SFD) indices as observed on IGS station Graz in the period 2002 – 2018. Ionospheric correction model disabled. Authors according to (IGS, 2017)

Positioning error correlates slightly better with SFD than with SSN, which can be explained that SSN is not a physical quantity, but indirect indicator of solar activity and as such does not directly influence Earth's ionosphere. However, differences are small, at least with data smoothed to one year rolling mean window. This suggests that average SSN number over longer periods such as one year is still a very reliable indicator of solar activity. In the following Figures, positioning errors are compared with solar indices, as described.

There are significant differences between stations itself in average error value. While average error for Ohrid is 3.31 m, for the same method of position calculation, Medicina has a 7.76 m average error, which is more than double.

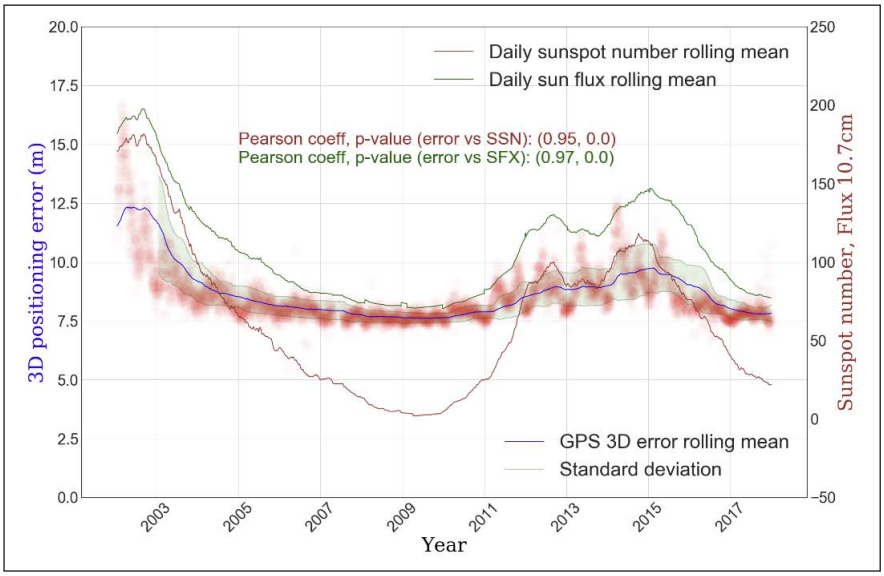

Figure 3. GPS 3D positioning error vs solar activity (SSN and SFD) indices as observed on IGS station Medicina in the period 2002 – 2018. Ionospheric correction model disabled. Authors according to (IGS, 2017)

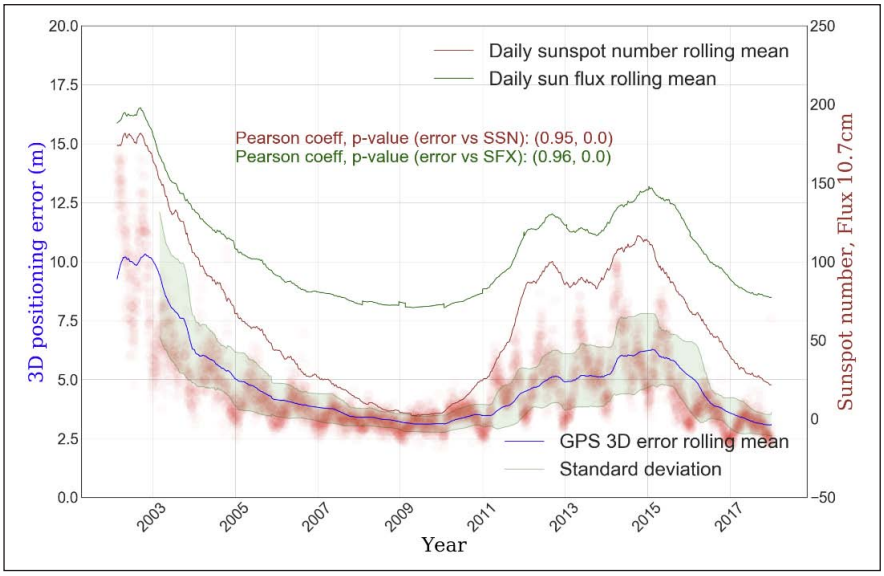

Figure 4. GPS 3D positioning error vs solar activity (SSN and SFD) indices as observed on IGS station Ohrid in the period 2002 – 2018. Ionospheric correction model disabled. Authors according to (IGS, 2017)

However, as error standard deviation for Medicina is lower than for Ohrid (0.34 vs 0.76), it might be that noted station position on IGS network website for Medicina is not accurate enough. Also, from the noted position, the numeric precision for Medicina is lower than for Ohrid.

Precision for Medicina is rounded to 4 decimal places, which in horizontal plane allows for maximum possible rounding error of 0.00005° or 5.56 meters in meridional direction and 3.97 meters in zonal direction. Combined, it gives the maximum of 6.83 meters in the worst case scenario that is possible due to rounding to 4 decimal places. This might very well explain why Medicina has a higher average error but lower error standard deviation. There is also possible that station elevation is also somewhat rounded, concluding from round 50.0 meters value. Same four decimal places rounding are also done for Graz station position, whereas Ohrid station has a position given in precision of 7 decimal places. Positioning errors with employed ionospheric correction applied and solar indicators are compared on Figures 5-7.

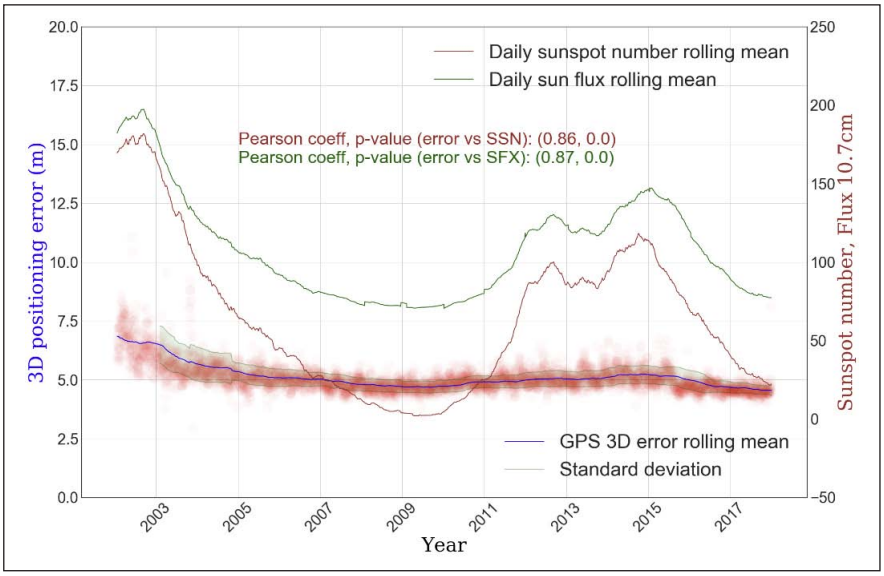

Figure 5. GPS 3D positioning error vs solar activity (SSN and SFD) indices as observed on IGS station Graz in the period 2002 – 2018. Ionospheric correction model enabled. Authors according to (IGS, 2017)

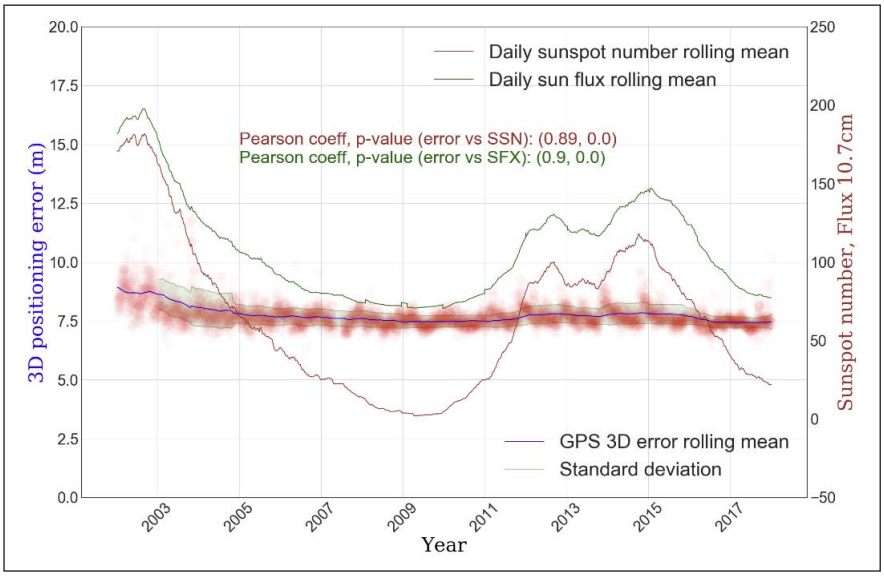

Figure 6. GPS 3D positioning error vs solar activity (SSN and SFD) indices as observed on IGS station Medicina in the period 2002 – 2018. Authors according to (IGS, 2017)

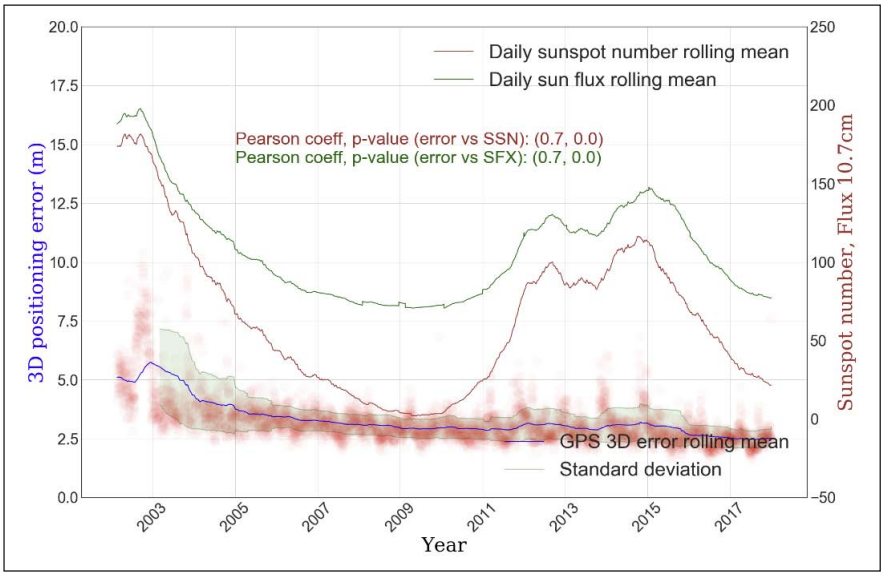

Figure 7. GPS 3D positioning error vs solar activity (SSN and SFD) indices as observed on IGS station Ohrid in the period 2002 – 2018. Ionospheric correction model enabled. Authors according to (IGS, 2017)

Compared to the scenario with ionospheric correction disabled, in this data set 3D positioning errors are smaller in absolute values throughout the observed period, and error scatter plot is significantly flatter. Moreover, smaller time scale fluctuations due to seasonal effects of Sun declination are much less noticeable. Error standard deviation is also lower in this scenario, with the mostly notable difference being observed during solar maxima periods and less difference during calm periods of solar cycles.

Additionally, the analysis shows that positioning error and error standard deviation are both higher when ionospheric corrections are not applied, as expected. The results are presented in Table 2.

Table 2. Correlation of positioning errors with solar indices for defined scenarios

Station	**Available days***	**Average error**		**Error standard deviation**		**Pearson correlation coefficients**					
						Mean error vs solar indicators				**Error standard deviation vs solar flux**	
		IC ON	IC OFF	IC ON	IC OFF	IC ON		IC OFF		IC ON	IC OFF
						SSN	SFD	SSN	SFD		
Graz	6038	5.14	7.56	0.51	1.43	0.86	0.87	0.97	0.99	0.82	0.95
Medicina	5994	7.76	8.72	0.34	1.56	0.89	0.90	0.95	0.97	0.76	0.95
Ohrid	5888	3.31	4.87	0.76	1.82	0.70	0.70	0.95	0.96	0.70	0.93
Overall / Total	17920	5.40	7.05	0.53	1.60	0.82	0.82	0.96	0.97	0.76	0.94

* Data in RINEX format for some days within analyzed period is missing at IGS servers.

Average GPS 3D positioning error and its standard deviation are given for the whole observed period, both for data set created with enabled and with disabled ionospheric correction. Pearson correlation coefficients are given for correlation between SSN and 3D GPS positioning error and also for correlation between SFD and 3D GPS positioning error, again for both data sets with and without ionospheric correction. Finally, Pearson correlation coefficient of correlation between standard deviation error and 10.7 cm daily solar flux data sets is given, for both scenarios with and without ionospheric correction.

Another employed method for visualization of results was the Kernel Density Estimation (KDE). Besides specific correlation between variables, KDE indicates regions of higher or lower densities, being significant (shades concentrated in a thin area) and small (shades distributed in a more broad area) correlations, respectively. Correlation between positioning error and SSN is given on the following Figure, containing plots for all stations and both ionospheric scenarios. Curves surrounding each plot are representing the shape of datasets distributions, i.e. the density functions.

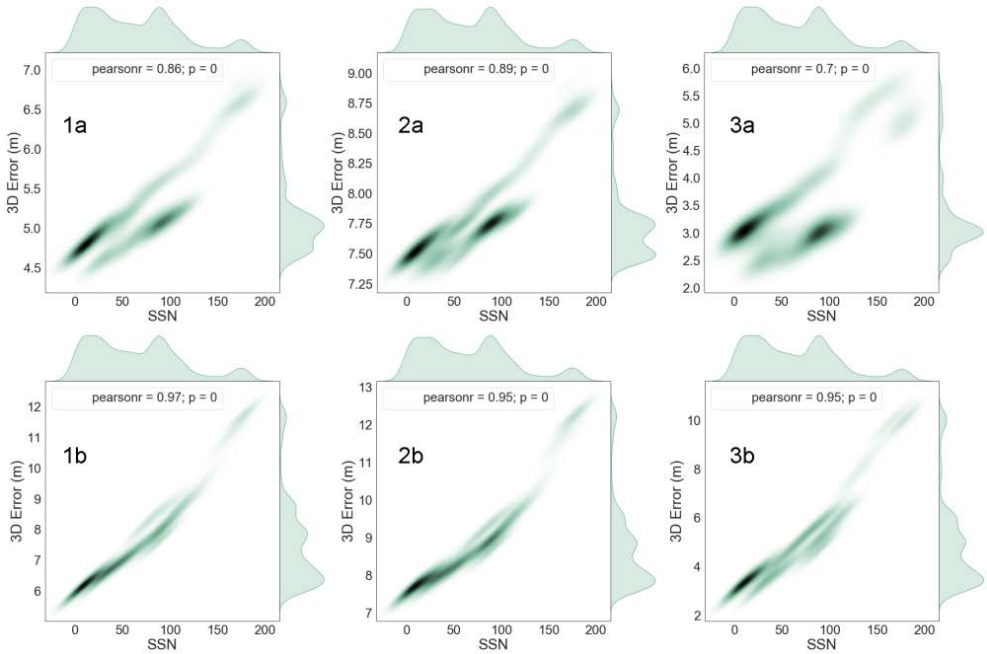

Figure 8. Kernel density estimates between values of 3D GPS positioning errors and SSN: IGS Graz with enabled (1a) and disabled (1b) ionospheric correction, IGS Medicina with enabled (2a) and disabled (2b) ionospheric correction, and IGS Ohrid with enabled (3a) and disabled (3b) ionospheric correction

Similarly, correlation of positioning error and SFD is given on the Figure 9.

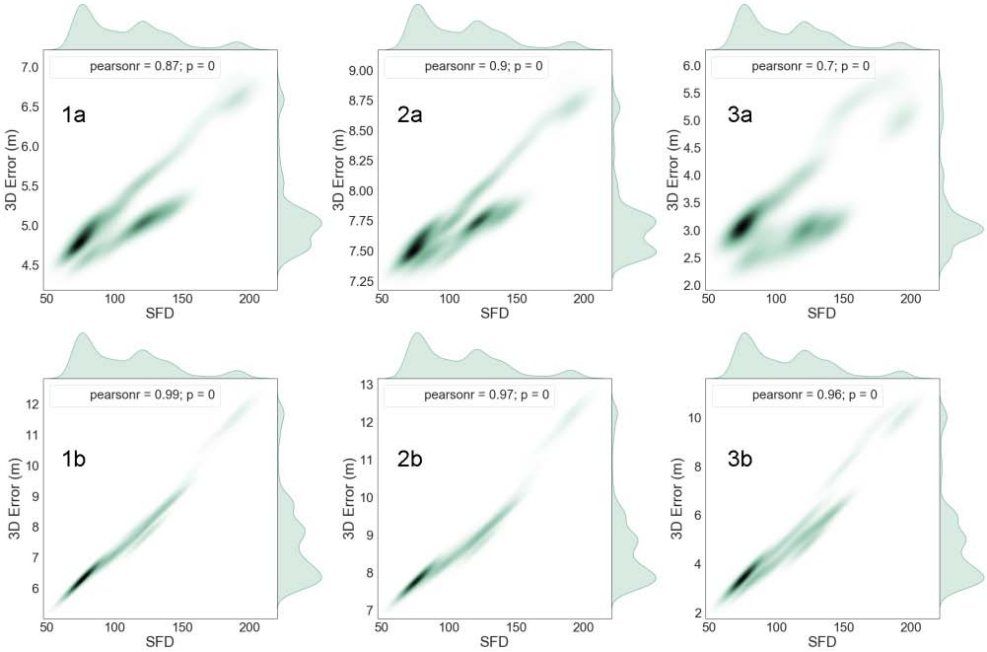

Figure 9. Kernel density estimates between values of 3D GPS positioning errors and SFD: IGS Graz with enabled (1a) and disabled (1b) ionospheric correction, IGS Medicina with enabled (2a) and disabled (2b) ionospheric correction, and IGS Ohrid with enabled (3a) and disabled (3b) ionospheric correction

6. 3D POSITIONING ERRORS IN CORRELATION WITH SEASONAL CYCLE

Seasonal periodic variation in three-dimensional positioning error is evident when ionospheric correction is not applied. In summer solstice positioning error is increased compared to the rest of the year. Most error increase occurs around June, and lowest errors can be observed around January. The following plot resembles an example of four years period, consisting of two years during the last sunspot cycle ending and two years of a calm period after the last cycle.

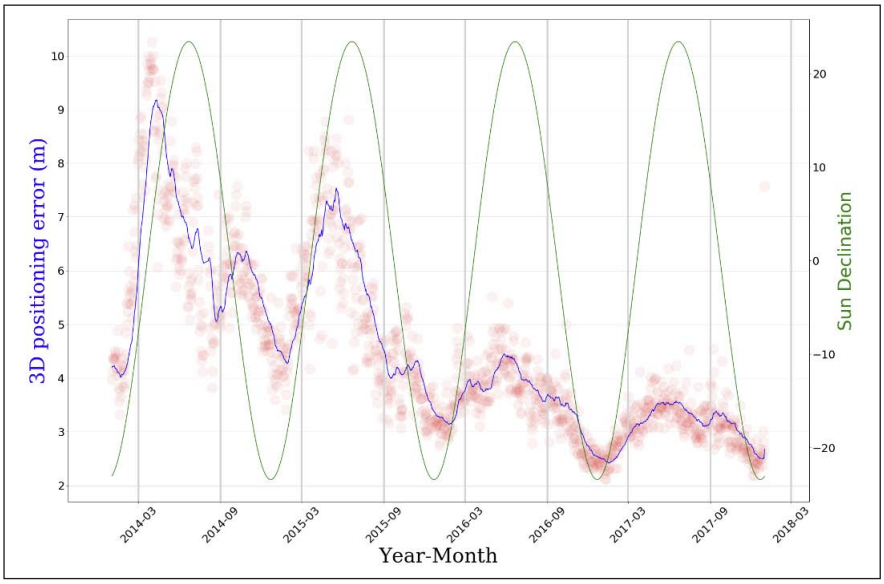

Figure 10. Presentation of seasonal variations positioning errors and declination of the Sun as determined for the IGS station Ohrid for four consecutive years (2014-2017). Ionospheric correction model disabled. Authors according to (IGS, 2017)

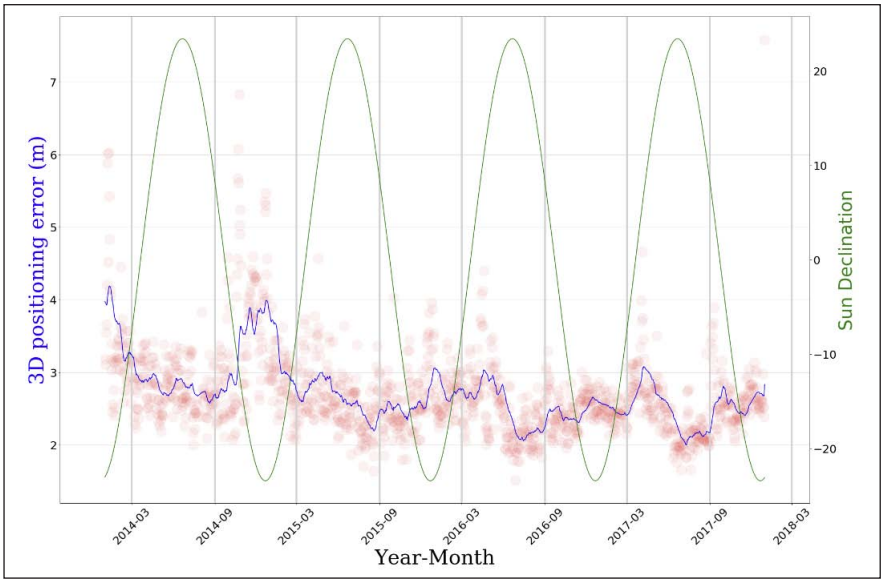

Figure 11. Presentation of seasonal variations positioning errors and declination of the Sun as determined for the IGS station Ohrid for four consecutive years (2014-2017). Authors according to (IGS, 2017)

Spearman correlation coefficients between 3D positioning error and Sun declination have also been determined (Table 3). To filter data noise, the rolling mean window (Fuller, 1976) of 30 days was introduced before calculating correlation.

Table 3. Correlation of positioning errors with Sun declination for defined scenarios

Station	Spearman correlation coefficients	
	IC OFF	IC ON
Graz	0.34	0.07
Medicina	0.24	-0.35
Ohrid	0.34	-0.27

When ionospheric correction is used, seasonal variations are almost completely indistinguishable. The following Figure resembles the same period as previous, with correction applied. There is a measurable increase in positioning error centred in May but is far from being obvious as when correction is not applied. With employment of the ionospheric model, largest positioning deviations appear slightly/one month before maximum Sun declination.

7. GPS L1 3D POSITIONING ERROR PREDICTION

Based on selected and analysed influential parameters, a machine learning approach (as described) was used to model the prediction of three-dimensional GPS positioning errors. Results are shown in Table 4. For data calculated without using GPS ionospheric correction, ElasticNet model was able to produce the mean value of R^2=0.61 from multiple runs using its default tuning parameters. Red/italic rows contain minimal and maximal SSN/SFD values recorded in the observed period. Bold/blue rows are examples of the hypothetical situation with extremely high SSN/SFD values that are not recorded in the observed period yet are likely to happen.

Model's R^2 value of 0.61 (without Klobuchar correction) and 0.38 (with Klobuchar correction) is not very high, but it should be noted that only 5589 samples (days) were available for model training, which is value on the low side for such tasks. With more available data, confidence in model's prediction should be higher. Model confidence is higher when Klobuchar correction is not applied, which is expected

because also data correlation is higher in such case. When correction is applied, the model doesn't have as good structure to fit as it has when processing data calculated without correction. However, even in correction applied case, simulated error values seem to be pretty reasonable (Table 3).

Table 4. GPS L1 3D positioning error prediction model based on solar indices input

SSN	SFD	3D error model prediction (m)	
		IC OFF	IC ON
0	0	5.16	4.75
0	66	5.56	4.92
20	70	5.98	5.05
50	80	6.62	5.26
100	100	7.72	5.61
100	150	8.03	5.74
150	100	8.70	5.91
150	150	9.00	6.04
195	178	10.05	6.39
200	200	10.29	6.47
300	300	12.85	7.33
400	400	15.42	8.19

On Figures 12 and 13, model's accuracy is presented comparing measured daily mean error from all three stations and model's prediction for given SSN/SFD combination for corresponding days. According to obtained results, larger values of both indices would significantly increase the amount of positioning error in both ionospheric scenarios. Although it mitigates the positioning error, the Klobuchar model could be improved based on the proposed approach and analyses of long-term solar activity influence.

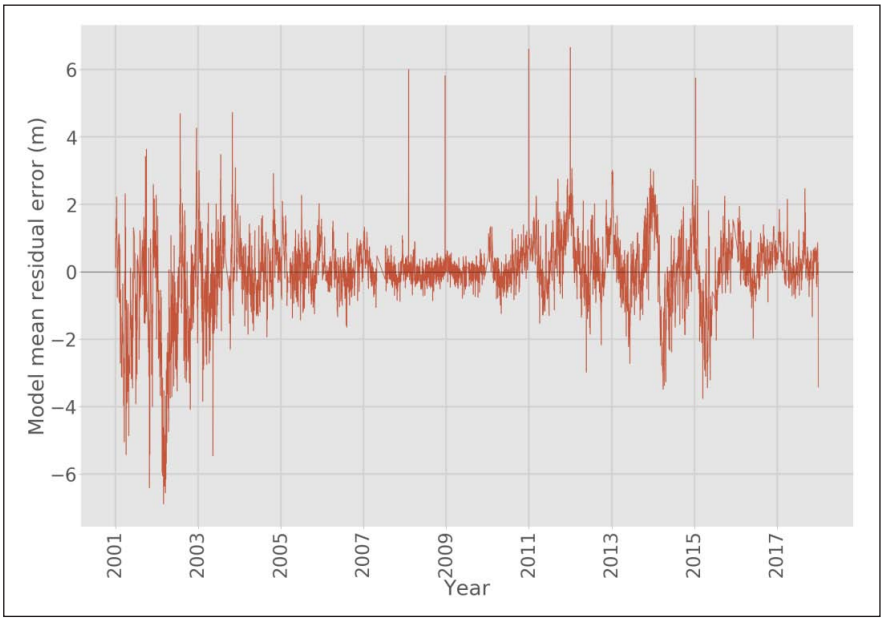

Figure 12. Model mean residual error. Ionospheric correction disabled.

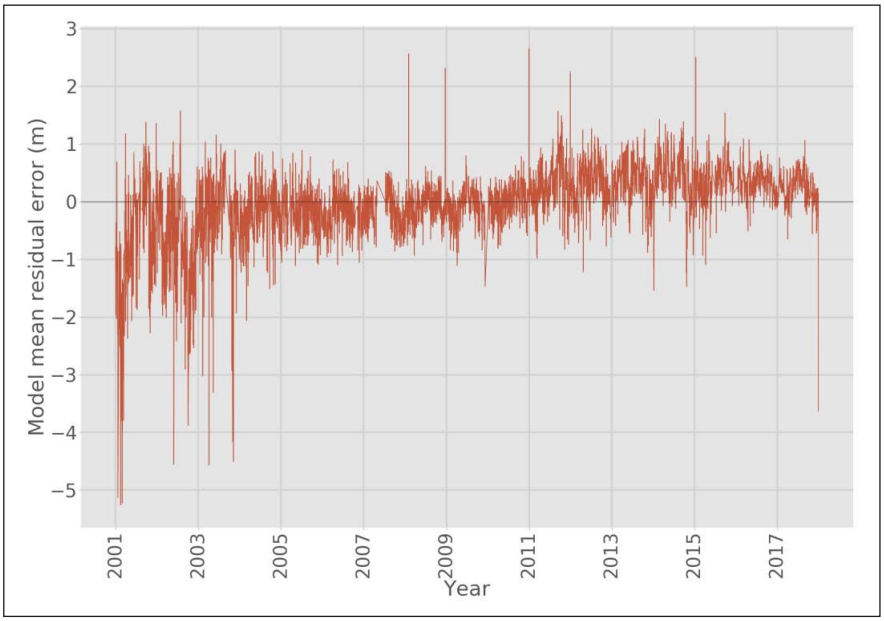

Figure 13. Model mean residual error. Ionospheric correction enabled.

The model's performance was further assessed with root mean squared error (RMSE) and mean absolute error (MAE). For a model variation without Klobuchar correction, RMSE was 1.12 m, and MAE was 0.75 m. With employment of the ionospheric model, RMSE amounted to 0.61 m, with MAE of 0.42 m, respectively.

8. CONCLUSIONS AND FURTHER TENDENCIES

In the proposed paper, solar impact on GNSS positioning was elaborated regarding long-term solar activity. Analyses have been made by comparing daily-averaged GPS L1 three-dimensional positioning errors and SSN and SFD indices through 17 years, as observed on three locations in the Adriatic region. A significant relationship has been found between solar cycle progress and GPS L1 positioning error, with and without employment of standard ionospheric correction model. Increased SSN and SFD strongly correlate with positioning error increase, expressed as mean error value and its standard deviation. With ionospheric correction, the correlation reduces, as expected; however not completely. Regularized regression method was used to perform positioning error predictive modelling, with employed solar indices as inputs. Validation of the model showed the successfulness in terms of determination coefficients 0.61 and 0.38, expressed with the R^2, for positioning solutions obtained with and without employment of the ionospheric correction, respectively.

Positioning errors were analysed in the function of declination, referring to annual variations of the Sun in the frame of LECS. The relation was observed when the ionospheric correction was not used, being stronger when the solar angle of incidence is more perpendicular to Northern hemisphere (positive declination) and vice versa (negative declination). Ionospheric correction removed most of seasonally induced errors; however measurable error persists with pronounced value in May. For the further work, employment and analyses of the second LECS coordinate are planned - the solar hour angle.

The paper presents preliminary results of the conducted research, both for seasonal and solar cycle periods. Long-term intervals were analysed for the sake of statistical acceptability in the function of previously set, daily parameters. Thus, the obtained results are based on daily intervals, i.e. positioning error mean daily values. For practical purposes it is necessary to analyse hourly intervals, implying an analysis of other solar indicators related to higher observation frequencies. Un-modelled positioning solutions were used as experimental, allowing for direct error observations

without modelling, as pure consequences of the long-term solar cycle activity. This can lead to the possible development of the ionospheric model based on observed regularities.

ACKNOWLEDGEMENTS. Research activities presented in this paper were conducted under the research project *Research into the correlation of maritime-transport elements in marine traffic: Satellite navigation segment*, supported by the University of Rijeka, Croatia.

References

Bent, R. B., Llewellyn, S. K. and Walloch, M. K. (1972). *Description and evaluation of the Bent Ionospheric model*. Volume 1. Melbourne: DBA Systems, Inc.

Clark, D. H. and Stephenson, F. R. (1978). An Interpretation of the Pre-Telescopic Sunspot Records from the Orient. *Quarterly Journal of the Royal Astronomical Society*. 19, pp. 387–410.

Dow, J.M., Neilan, R.E. and Rizos, C. (2009). The International GNSS Service in a changing landscape of Global Navigation Satellite Systems. *Journal of Geodesy*. 83, pp. 191–198.

Feynman, R. P., Leighton R. B. and Sands, M. (2011). *The Feynman Lectures on Physics*. New York: Basic Books.

Fuller, W. A. (1976). *Introduction to statistical time series*. Hoboken: John Wiley.

Goodman, J. (2005). *Space Weather & Telecommunications*. Heidelberg: Springer Science+Business Media, Inc.

Hathaway, D. H. (2010). *The Solar Cycle*. Cham: Springer Nature.

Institute of Electrical and Electronic Engineers (IEEE). (1998). *IEEE Standard Definitions of Terms for Radio Wave Propagation*. New York: IEEE.

International GNSS Service (IGS). (2018). Available at: http://www.igs.org, accessed on 15.04.2018.

International GNSS Service (IGS). (2017). The Receiver INdependent EXchange Format (RINEX). Available at: https://bit.ly/2uudFVe, accessed 22 April 2018.

Klobuchar, J. (1987). Ionospheric Time-Delay Algorithm for Single-Frequency GPS Users. *IEEE Transactions on Aerospace and Electronic Systems*. 3, pp. 325–331.

Kumar, S., Priyadarshi, S. and Gopi, K. S. (2012). GPS-TEC variations during low solar activity period (2007–2009) at Indian low latitude stations. *Astrophysics and Space Science*. 339(1), pp. 165–178.

Li, K. J., Kong, D. F., Liang, H. F. and Feng, W. (2014). What do the solar activity indices represent? *Astronomical Notes*. 335(3), pp. 371–377.

Lipovac, M. Š. (1981). *Astronomska navigacija*. Split: HIJRM.

National Oceanic and Atmospheric Administration (NOAA). (2018). Daily Sunspot Numbers. Available at: https://bit.ly/2NaVgo2, accessed 2 May 2018.

Petrovski, I. and Tsujii, T. (2012). *Digital Satellite Navigation and Geophysics*. Cambridge: Cambridge University Press.

Rodgers, J. L. and Nicewander, W. A. (1988). Thirteen Ways to Look at the Correlation Coefficient. The American Statistician. Available at: https://bit.ly/2JiFdCr, accessed 12 June 2018.

Subirana, J. S., Zornoza J. M. J. and Hernandez-Pajares, M. (2013). *GNSS Data processing, Volume I: Fundamentals and algorithms*. Noordwijk: ESA Communications.

Takasu, T. (2018). RTKLIB: An Open Source Program Package for GNSS Positioning. Available at http://www.rtklib.com, accessed 22 April 2018.

Tapping, K. F. (2013). The 10.7 cm solar radio flux ($F_{10.7}$). *Space Weather*. 11, pp. 394–406.

US Department of Defense (DoD). (2007). DoD Permanently Discontinues Procurement of Global Positioning System Selective Availability. Available at: https://bit.ly/2zHzVB9, accessed 9 July 2018.

Vallado, D. A. (2001). *Fundamentals of Astrodynamics and Applications*. El Segundo: Microcosm Press.

Wikimedia. (2018). Local equatorial coordinate system. Available at: https://bit.ly/2NV2pKn, accessed 4 April 2018.

Zou, H., and Hastie, T. (2005). Regularization and variable selection via the elastic net. *Journal of the Royal Statistical Society*. 67(2). pp. 301–320.

Sveučilište u Rijeci
POMORSKI FAKULTET
FACULTY OF MARITIME STUDIES
University of Rijeka

University of Zagreb
Faculty of Transport and Traffic Sciences

Royal Institute of Navigation
Science Technology Practice

12th Annual Baška GNSS Conference

GNSS PRECISE POINT POSITIONING FOR AUTONOMOUS ROBOT NAVIGATION IN GREEN-HOUSE ENVIRONMENT FOR INTEGRATED PEST MONITORING

Michael Pattinson[1], **Smita Tiwari**[1], **Yuheng Zheng**[1], **María Campo-Cossio**[2], **Raúl Arnau**[2], **David Obregón**[2], **Ander Ansuategui**[3], **Carlos Tubio**[3], **Iker Lluvia**[3], **Oscar Rey**[4], **Jeroen Verschoore**[5], **Libor Lenza**[6], **Joaquin Reyes**[7]

[1] Nottingham Scientific Limited, Nottingham, United Kingdom
e-mail: michael.pattinson@nsl.eu.com (Corresponding author)

[2] Centro Tecnológico CTC, Santander, Spain

[3] Fundación Tekniker, Eibar, Spain

[4] Inkoa Sistemas, Erandio, Spain

[5] Aerovision BV, Amersfoort, Netherlands

[6] Mendelova Univerzita v Brně, Brno, Czech Republic

[7] European GNSS Agency (GSA), Prague, Czech Republic

Abstract

GreenPatrol robot is an autonomous robotic solution for early detection and control of pests in greenhouses. The importance of robot precise positioning inside the greenhouse is a key aspect to endow the robot with the ability to scout the environment, precisely register the detected pest location into accurate maps and to allow the later treatment. Greenhouses are a challenging environment in terms of multipath and signal blockage due to its metal-reinforced complex structures of glass or polycarbonate. GreenPatrol

robot localization takes advantage of the higher accuracy and the multiple signal frequencies provided by the European Global Navigation Satellite System (EGNSS) of the Galileo constellation (E5Alt BOC), by means of precise positioning techniques combined with inertial measurement sensors, odometry and maps to provide an accurate global localization mechanism. This paper shows the results of a comparative analysis carried out in a Greenhouse environment in order to evaluate the performance of different processing techniques such as Precise Point Positioning (PPP) and Post Processed Kinematic (PPK). The purpose of this analysis is to study the advantages of the use of Galileo new signals and to determine the best global localization solution for the GreenPatrol robot. The results experimentally show that the use of PPP Galileo E5 AltBOC signal in a multi-constellation solution offers better signal quality and better positioning performance for the intended environment.

Keywords: *GNSS, Precise Point Positioning, Precision Farming, Integrated Pest Monitoring*

1. INTRODUCTION

Timely pest detection in agriculture increases the quantity of crop production and reduces the use of pesticides. Nowadays there are several automatic Integrated Pest Management (IPM) tools and techniques available (Ueka and Arima, 2015); nevertheless, there is no automatic method using robotic platforms for early and online pest detection in greenhouse crops.

There are different conventional ways to detect pests on crops. Eye observation methods have been extensively used until recent years, but they are not efficient in large crops. Automatic inspection by computer vision has become very common since it reduces the burden of repetitive tasks, improves the accuracy and leads to a productivity increase.

With this aim, the main objective of the GreenPatrol project is to design and develop an innovative and efficient robotic solution for IPM in crops, which has the ability to navigate inside greenhouses while performing pest detection and control tasks in an autonomous way. GreenPatrol navigation capability is enabled by EGNSS new signals and the implementation of sensor fusion techniques.

The additional use of external sensors can provide very precise measurements with good short-term stability that is not affected by external interference, multipath or obstructions. It can be an effective measure to help overcome some of the limitations of GNSS in urban areas:

- The additional sensors provide an independent measure of change in state – not affected by same errors as GNSS – so can be used to help detect problems with GNSS (fault detection, cycle slips),
- Once initialized, the additional sensors can provide a solution even when GNSS is not available (increase availability),
- Additional sensors can be combined with GNSS to improve accuracy and give greater confidence in results.

The goal is to get timely, accurate (in terms of pest detection but also in the location of the infested plants) and reliable scouting records in a cost-effective way to allow growers to exploit the IPM associated benefits.

To reach this goal, GreenPatrol relies on *1)* Robot precise positioning solution able to operate in the intended challenging environment, providing accurate and detailed pest maps for decision making about precise case-specific treatment, *2)* Integration of Galileo's new signals and modulation in light indoor environment, *3)* Perception with visual sensing for on-line pest detection, including reasoning mechanisms for efficient action selection and *4)* Control strategies for manipulation and motion planning based on pest monitoring system feedback.

The use of Galileo's new signal and modulation is a fundamental building brick in the development of the GreenPatrol solution as it provides the mechanism (i.e. new signals and modulations providing better performance) to cope with the inherent sources of error present in light indoor scenarios (multipath, signal blockage, etc.).

2. AUTONOMOUS NAVIGATION OF MOBILE ROBOTS IN AGRICULTURAL ENVIRONMENT

The problem of autonomous navigation of mobile robots is divided into three main areas: localization, mapping and path planning. Localization is the process of determining where a mobile robot is located with respect to its environment. Mapping integrates the partial observations of the surroundings into a single consistent model and path planning determines the best route in the map to navigate through the environment. Initially, these areas were studied separately, but they are closely dependent. In order to build a realistic map of the environment the robot must know its position and orientation all along, and to localize itself inside the environment, the robot needs an accurate map. This problem is known as Simultaneous Localization And Mapping (SLAM) (Berns and Puttkamer, 2009).

The solution to the localization, mapping and path planning of mobile robots strongly depends on the information that is available on the state of the robot and the environment. Many types of sensors have been used with this aim (inertial sensors, odometry, SONAR, LIDAR, etc.).

According to the source of the input data given, many popular SLAM implementations use laser range information as input to simplify the estimation process to a pure localization and registration since laser range finders estimate the 3D locations of the imaged points directly. Information about the current orientation changes relative to a previous estimate can be calculated from the encoder information in the odometry on the robot until a localization update becomes available again. The situation changes considerably with the introduction of a robot designed to operate in off-road environments where it can bounce from the ground and tilt in an unexpected way making any estimates of the odometry information nearly useless. As a consequence, an inertial system becomes necessary to deal with these alterations in the robot's movement since it provides a six degree-of-freedom motion sensing. However, these systems measure the velocities and accelerations directly so that the data has to be processed to obtain an absolute position and orientation, i.e. pose of the mobile platform. This estimation is susceptible to errors due to offsets and noise in the measurements, so an external system of localization should give accurate information for this purpose.

Autonomous navigation in an agricultural environment is a difficult task due to the inherent uncertainty in the environment where shapes, sizes and colors of plants, light intensity and overall surroundings vary. As a result, it's complicating to maintain a realistic and updated map with which a visual-based system can perform an efficient matching. For this reason, GreenPatrol proposes to use a method resistant to those limitations based on a combination of robot localization techniques with global positioning sources of information, such us global navigation satellite systems (GNSS). The fact that it calculates the pose based on the signals received from satellites makes the GNSS a good choice for the system localization as it is independent of the limitations of the environment.

3. GNSS POSITIONING

3.1 *GNSS techniques*. The main types of solution that have been analyzed for the experimentation in this paper include GNSS: Single point code solution, GNSS Post Processed Kinematic (PPK) and GNSS Precise Point Positioning (PPP).

3.1.1 Single point code solution. A single point code solution is robust and easy to compute but suffers from several limitations. Firstly, this code (or pseudorange) measurements suffer from noise and other errors that limit the performance and mean that the precision of the position solutions is ~1-2 m at best. This is fine for many types of applications but would not be good enough for the navigation of the robotic platform and geo-referencing of photographs or treatments.

3.1.2 Real Time Kinematic (RTK)/Post Process Kinematic (PPK). RTK has been used extensively over the years and can provide the positioning of high precision and accuracy (a few cms) with rapid convergence in both real-time (RTK) and post processing (PPK) mode. Basically, the main difference between the RTK and PPK is the mode in which the correcting takes place. RTK corrects in real time while PPK correct in post processing. However, it has two main drawbacks (Guo *et al.*, 2018). The first is the need for a dedicated base station, which means that either the user needs to set-up their own local base station (which can increase equipment costs) or else make use of existing reference stations that provide real-time corrections (either for a single reference station or using a network Virtual Reference Station VRS approach), although this incurs a service charge. Additionally, there is performance degradation with the distance between base station and users, and so if there are no nearby reference stations or the application covers a wide area then the performance of RTK is limited.

3.1.3 Precise Point Positioning (PPP). PPP is an efficient positioning technique that uses the undifferenced pseudorange and carrier phase measurements from a single (multi frequency) receiver, together with the precise orbit and clock corrections and the application of additional error models (earth tides, satellite phase wind-up, etc.), in order to compute a precise solution. This removes the need for a local reference station and means that PPP is applicable anywhere in the world as the accuracy is not dependent on the distance from a reference station. In addition, the user position can be computed directly in a global reference frame rather than positioning relative to a single reference station. However, PPP relies on external correction products (i.e. precise orbit and clock products) in order to get the best performance.

3.2 *GNSS constellations*. Different combinations of constellations and signals are also compared in this paper for GNSS processing: The United State GPS, Russian Glonass and the European Galileo. The potential advantage for a user of combining satellites from different constellations is that it increases the number of measurements available,

which can be critical in situations where there may be blockages or interruptions to the signal (like inside a greenhouse). Using multiple frequency measurements allows more accurate positioning, as the combination of two frequencies can remove errors caused by ionospheric refraction of the signals.

3.3 *Galileo new features in the light indoor environment.* GNSS positioning techniques provide real-time measurements that can be used in some scenarios as the primary sensor in agricultural robot navigation systems (Perez and Upadhyaya, 2012). However, in covered areas such as orchards or greenhouses, satellite signal occlusion and multiple reflections may degrade the solution. The effects of strong multipath and signal blockage, typical in greenhouses due to its metal-reinforced complex structures of polycarbonate and glass, can be alleviated by using the Galileo E5 broadband signal. This signal includes a new modulation scheme with higher power and better tracking performance, AltBOC, that can drastically reduce noise and multipath effects leading to a more robust and reliable precise positioning solution when the robotic system is operating under adverse conditions (Shivaramaiah and Dempster, 2009, Toho *et al.*, 2012).

4. TEST SCENARIO IN GREENHOUSE ENVIRONMENT

A greenhouse scenario usually consists of a metal structure with partially dielectric coverage that can cause signal attenuation, blockage, multiple reflections, etc. that can drastically hinder the navigation solution. Moreover, some crops are vertically grown (such as tomatoes) reaching more than 2 meters high which cause many times signal occlusion in the narrow corridors.

Figure 1. Greenhouse location and roof detail

The test scenario for this paper is a group of greenhouses located in Lezama, Bizkaia (Spain) on a flat zone limited by two mountains lines at coordinate 43°17’12.2” N 2°50’01.0” W. Tests were performed in an aluminum and glass building with rectangular shape and gabled roof where the plants grow in rows perpendiculars to the longest side.

5. EXPERIMENTAL SETUP

5.1 *GreenPatrol robot.* The robot platform used for the GreenPatrol solution is a Segway® Flex OMNI, a true holonomic mobile robot platform ideal for use in an environment with limited space that requires precise mobility and handling. Its four mecanum wheels allow it to move in any direction without needing to turn – and it can turn in place just as easily as it can drive sideways.

The platform carries wheel encoders and an Inertial Measurement Unit (IMU), whose data are combined to get an improved odometry estimation. It also has a Velodyne VLP-16 LiDAR, a Real-time, 3D distance and calibrated reflectivity measurements sensor. It has a 360° horizontal field of view and a 30° vertical field of view, with +/- 15° up and down.

Figure 2. GreenPatrol test robot

5.2 *Sensors.* Apart from the available sensors in the platform (INS and odometry), a high-grade Galileo-capable GNSS receiver and antenna have been selected for this test and mounted onboard the robot. It provides the core data for post-processing and assessment of different types of GNSS solution. This multi-frequency multi constellation GNSS receiver has the following features: GPS: L1, L2, L5, GLONASS: L1, L2, L3, Galileo: E1, E5a, E5b, E5ab (AltBOC), BeiDou: B1, B2, SBAS: EGNOS, WAAS, GAGAN, MSAS, SDCM (L1, L5), QZSS: L1, L2, L5, L6.

As well as the equipment of the robotic platform, a local GNSS reference receiver was installed during the data collection campaign. This receiver was installed in an open sky area to provide measurements for a short-baseline kinematic solution for comparison with other techniques.

5.3 *External data providers.* In addition to the sensor data from the robotic platform, some additional external data is required in order to generate all the required post-processing solutions.

For the static data performance assessment, a reference position is required for the points in order to be able to compute errors and generate statistics. For the outdoor location this is achieved by providing the RINEX data to the NRCan website where there is a service to process the data and provides an estimated accurate position. Also, to compute a Precise Point Positioning (PPP) solution, high quality satellite orbit and clock products are required. For this data collection and post-processing, it is sufficient to retrieve this data after the event[1]. In addition to precise orbit and clock correction, other products may also be useful: IONEX[2] and DCB[3].

6. STATIC TESTS

In order to understand the impact that the greenhouse has on the data quality, and ultimately on the position solution, static tests have been performed inside and outside the greenhouse. In addition, the performance of the Galileo E5 AltBOC signal compared to other signals is analyzed in this paper as it is hoped to offer improved performance in the greenhouse.

[1] ftp://cddis.gsfc.nasa.gov/gnss/products/mgex

[2] ftp://cddis.gsfc.nasa.gov/gnss/products/ionex

[3] ftp://igs.ign.fr/pub/igs/products/mgex/dcb

To assess the performance, various quality parameters, including the number of satellites tracked, cycle slip, multipath and signal to noise ratio (SNR) have been measured at GPS L1, Galileo E5a and Galileo AltBOC frequency.

The position solution at the receiver improves if there are more satellites available. In difficult environments some of these signals may be blocked, and this can affect the positioning performance. Comparing the number of satellites tracked indoors and outdoors allows us to see the impact of the greenhouse on tracking.

For PPP carrier phase measurements are the key parameter, they can be very precisely measured and hence are necessary to be used in order to get down to the performance required for robot navigation. Nevertheless, carrier phase measurements contain an unknown ambiguity term that must be solved. The success of resolving this ambiguity term relies on having continuous data, but if there are interruptions in tracking this causes a cycle slip and can make it more difficult to obtain a precise carrier phase solution. Therefore, having a low number of cycle slips is desirable. The number of cycle slips detected in the measurements inside and outside the greenhouse can help to give an idea of the difficulty and how feasible it is to use the carrier phase measurements.

Another important quality check parameter is multipath, in locations where there are reflective surfaces the GNSS signals from the satellites may be reflected. This can mean that the user antenna receives both direct and reflected signals from the satellites, and the measurements will, therefore, be contaminated by the reflected signals and contain errors. These errors will then affect positioning performance. And finally, SNR this provides a measure of how strong the satellite signal is compared to background noise and is important because a clear signal with high SNR is easier to track and less likely to be contaminated by multipath and other errors. Comparing the SNR values indoors and outdoors gives an idea of the impact of the greenhouse on the signal.

These metrics are used to compare the data from the multifrequency receiver for Test 1 (static open sky), Test 2 (static inside greenhouse).

Figure 3. Outdoor and inside greenhouse GNSS antenna locations

The following table summarizes the quality check test results.

Table 1. Quality Check Comparison

Cycle Slip			
Test Scenario\GNSS Constellation	L1 GPS	E5a Galileo	E5 AltBOCGalileo
Test 1 Outdoor Open Sky	20	5	3
Test 2 Greenhouse	4709	5	3
RMS Multipath (m)			
Test 1 Outdoor Open Sky	0.399	0.268	0.166
Test 2 Greenhouse	0.7158	0.639	0.499
Average SNR (dB)			
Test 1 Outdoor Open Sky	43.10	42.42	42.49
Test 2 Greenhouse	43.05	42.05	42.05
Average Number of Tracked Satellites			
	GPS		GALILEO
Test 1 Outdoor Open Sky	8.37		5.03
Test 2 Greenhouse	8.25		5.00

Results show that outdoors there is good satellite visibility for both GPS and Galileo. However, in indoors, the number of tracked satellites is lower but not by a large amount, indicating that the greenhouse structure does not fully block the satellite signals. This is important as it means that a positioning solution will still be possible indoors. It can be seen that in the outdoor case the average SNR for GPS L1 is slightly higher than for Galileo signals, but both are good. When moving indoors, there is some reduction in SNR for both GPS and Galileo signals, but it is not a very large reduction.

If we consider multipath, we can see that even outdoors there is a certain level of multipath error. The indoor tests show much larger levels of multipath though. This means that range errors are larger indoors and will likely affect the quality of the position solution. One interesting and encouraging point is that the Galileo signals have lower multipath errors than the GPS signals – both outdoors and indoors.

Finally, if we look at the registered number of cycle slips, the impact of the greenhouse can be appreciated, with more cycle slips in the indoor scenarios, and also shows the benefit of Galileo E5 AltBOC, with far few cycle slips reported than for GPS L1 signals.

In addition to looking at the signal quality in these static tests, the GNSS data has been processed to observe the effect of different frequencies and constellations on the position solution. NSL in-house software MSP3 has been used to produce precise point positioning (PPP). To be noted that the same RINEX data has been used to compute position using PPP, which has been used to compute the estimated accurate position. In this way we have two solutions; one which is generated by NRCan and one which is generated by NSL in house software. In order to check the accuracy of MSP3 generated PPP solution NRCAan generated position is used as a reference position.

For both the outdoor and indoor data, the position results from each epoch are compared against a reference position to compute errors and generate statistics. However, for indoor test we used the average position of the results as the reference coordinate to calculate position accuracy. This limitation means that the absolute accuracy values may not be entirely correct for the indoor tests, but the precision and convergence time results are still useful.

The following tables summarizes the position solution results (PPP and single point code) obtained from different combinations of constellations and signals. We obtain precise and orbit product from CDDIS MGEX product.

Table 2. Summary of Horizontal Position Accuracy (m) by single point code for static tests using RTKlib

Constellations	Signals	Horizontal Error Percentile							
		Test 1. Outdoor				Test 2. Greenhouse			
		50 %	68 %	95 %	99 %	50 %	68 %	95 %	99 %
GPS	L1	0.43	0.60	1.28	2.60	1.63	2.32	6.1	6.76
GPS+GAL	L1	0.41	0.55	1.14	2.34	1.82	2.58	5.57	6.29
GPS+GAL+GLO	L1	0.52	0.64	1.18	2.42	1.75	2.48	4.90	5.55

Table 3. Summary of Horizontal Position Accuracy (meters) by PPP for static tests using MSP3

Constellations	Signals	Horizontal Error Percentile							
		Test 1. Outdoor				Test 2. Greenhouse			
		50 %	68 %	95 %	99 %	50 %	68 %	95 %	99 %
GPS	L1/L2	0.15	0.17	0.22	0.23	0.69	0.79	1	1.21
GPS+GAL	L1/L2/E5a	0.05	0.06	0.11	0.13	0.31	0.38	0.56	0.56
GPS+GAL	L1/L2/E5 AltBOC	0.05	0.06	0.10	0.13	0.15	0.23	0.3	0.32
GPS+GAL+GLO	L1/L2/E5a	0.40	0.41	0.44	0.45	0.48	0.57	0.76	0.76

Statistical results show the advantages of PPP over a single point code solution. It also shows that the use of Galileo AltBOC signal not only improves the position solution by providing the 95 % accuracy of 10 cm but also shows an advantage in inside the green house.

In addition to accuracy of the solution, convergence time is also important. For the envisaged operations it is no good having a very accurate solution if it takes several hours of initialization before that best solution can be reached. It is well known that PPP solutions can take some time to converge, but the indoors performance is not something that has been widely studied. To show the convergence, the time series of position errors for each test are shown.

It appears from these results that indoors PPP solutions do converge to a stable solution in a timeframe similar to outdoors, but the positions errors are higher after convergence, i.e. the final solution is not as accurate in the greenhouse scenario.

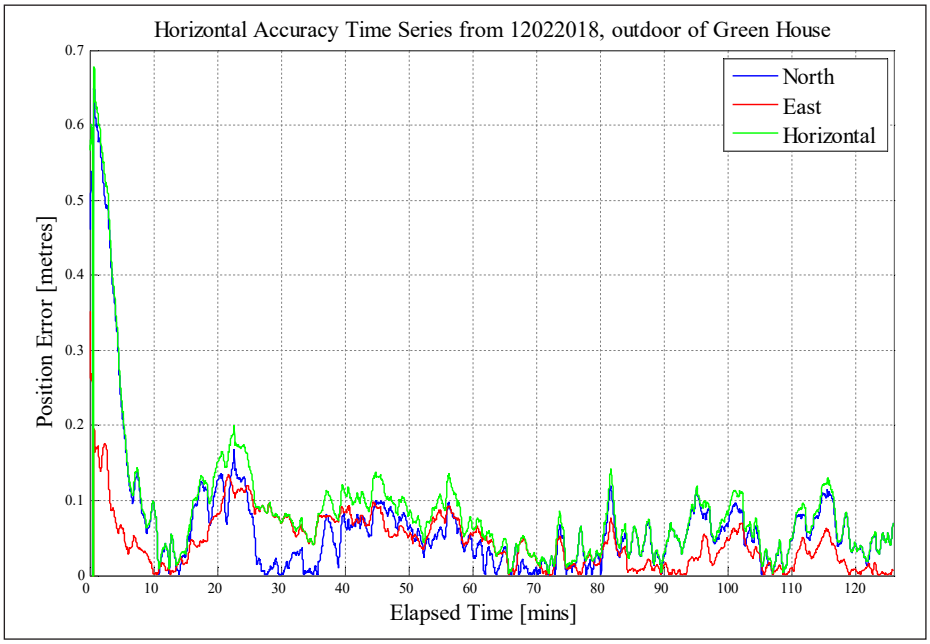

Figure 4. Horizontal accuracy produced by MSP3 using PPP, outside the greenhouse.

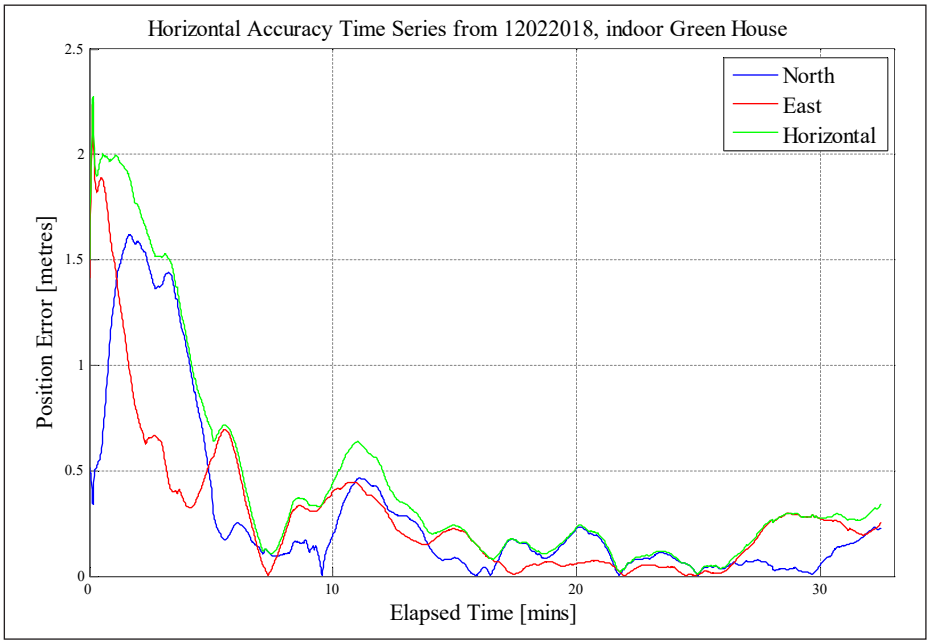

Figure 5. Horizontal accuracy produced by MSP3 using PPP, inside the greenhouse.

7. DYNAMIC INSIDE THE GREENHOUSE

For the dynamic tests, data from various sensors have been used:

- The core GNSS results are generated by processing multi-constellation, multi-frequency observations from the GNSS receiver mounted onboard the robot.
- In order to compare the PPK with PPP solution, a local base station (single frequency GNSS receiver) has been installed outside the greenhouse, with a known position. The onboard GNSS receiver is used as a rover for the PPK solution.

For this data collection no 'true' reference positions are available, and so the analysis is limited to inspection of the trajectory defined by the position solutions to see how well it describes the path of the robot during each test.

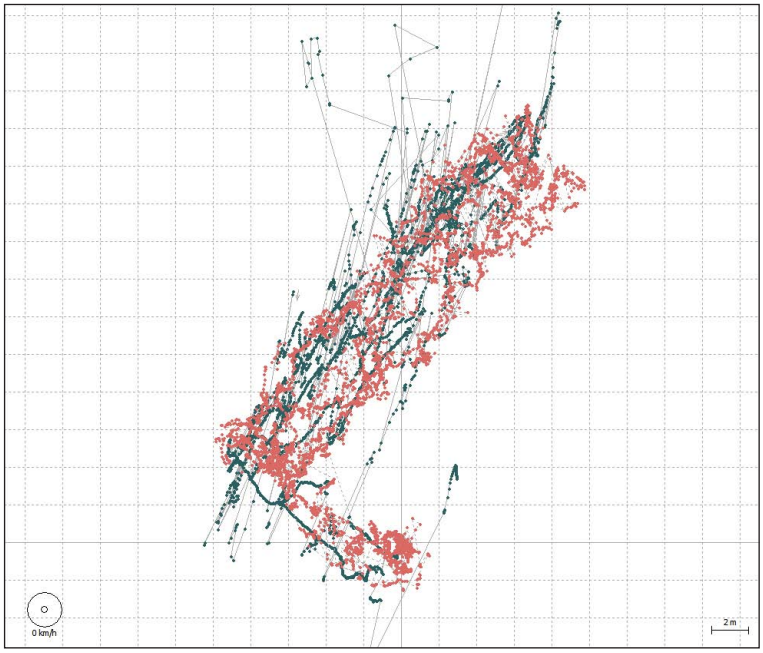

Figure 6. Scatter plot of GPS+GAL Code Solution (red) and GPS+GAL PPP (green) Solution for Test 3

In this test, the robot moved inside the green house along some of the side corridors and then returned to the start point. We can see again from the GPS+GAL code solution from RTKlib (red dots) the general movement of the robot. However, there

is a lot of scattering in the results, and it cannot be deduced the exact track on which the robot moved. The RTKlib GPS+GAL L1/L2/E5a solution (blue line) again shows some smooth parts but many jumps, and it is difficult to tell from that the robot route.

For the MSP3 GPS+GAL L1/L2/E5AltBOC solution, the trajectory is much smoother, and the route down the different side corridors is clear to see.

Figure 7. Google Earth plot of GPS+GAL L1/L2/E5AltBOC PPP Solution from MSP3 for Test 3 Dynamic

In this test corresponding to test 3, the dynamic, base station is also logging GNSS data, which further use in producing position solution using PPK via RTKLib. In the following figure, the red trajectory shows the position solution produced by PPK while blue trajectory is produced by PPP solution using MSP3.

It can be seen that both solutions show a common trajectory; however, PPP solution produces a very smooth solution, while sometimes PPK solution distracts from the trajectory and shows some jump. We can clearly see the advantage of using PPP over PPK.

Figure 8. Comparison of GPS+GAL L1/L2/E5AltBOC PPP Solutions from MSP3 (Blue) to the PPK (Red) for Test 3. Dynamic

8. CONCLUSION

From these results we can make the following conclusions: Various quality parameters have been measured at GPS L1, Galileo E5a and Galileo AltBOC frequency in order to assess the impact of the greenhouse roof. The number of tracked satellites is slightly lower when moving indoors, as well as the SNR for both GPS and Galileo signals, but the greenhouse structure does not fully block the satellite signals. This means that a positioning solution is still possible indoors.

The indoor tests show much larger levels of multipath than outdoors. This means that range errors are larger indoors and will likely affect the quality of the position solution. One interesting and encouraging point is that the Galileo signals have lower multipath errors than the GPS signals, both outdoors and indoors. This is most noticeable for Galileo E5 AltBOC signals and demonstrates the advantage of

this signal and the potential for using it in GreenPatrol. Tests also show the benefit of Galileo E5 AltBOC, with far few cycle slips reported than for GPS L1 signals inside the greenhouse.

Overall, therefore, we can see that, although tracking conditions are more difficult in the greenhouse, they are not insurmountable for providing a GNSS solution, and the performance of Galileo E5 AltBOC is especially encouraging as it shows the best performance indoors.

It can be seen that the Galileo E5 AltBOC signal offers clear advantages over the other signals in terms of better signal quality and better positioning performance and so the use of a receiver that can provide these measurements is highly recommended.

In terms of the type of solution, PPP has shown excellent performance outdoors, and the indoor tests (particularly the dynamic ones) are highly encouraging in terms of the performance that can be achieved. Test results confirmed that PPP also shows equivalent performance with respect to PPK. In a remote environment like Greenhouse where the possibility of nearest base station is rarer, PPP shows a significant alternative to PPK and shows better position performance.

FINANCIAL SUPPORT. The presented results have been achieved within the GREENPATROL project (http://greenpatrol-robot.eu). The project has received funding from the European Union's Horizon 2020 research and innovation programme under grant agreement No 776324.

References

Berns, K. and von Puttkamer, E. (2009). *Autonomous Land Vehicles*. Wiesbaden: Vieweg Teubner.

Ebrahimi, M. A., Khoshtaghaza, M., Minaee, S. & Jamshidi, B. (2017) Vision-based pest detection based on SVM classification method. *Computers and Electronics in Agriculture*. pp. 52–58.

Guo, J., Li, X., Li, Z., Hu, L., Yang, G., Zhao, C., Fairbairn., Watson, D. and Ge, M. (2018). Multi-GNSS precise point positioning for precise agriculture. *Precision Agriculture.* 19. pp. 895–911.

Hu A. P., Thomas, S., Jennings, B. and Mcmurray, G. (2014). Development and Testing of a Low-Cost Multi-Function Robotic Arm for Agriculture. *American Society of Agricultural and Biological Engineers Annual International Meeting (ASABE 2014)*. Montreal. pp. 4565–4574.

Huddar, S. R., Gowri, S., Keerthana, K., Vasanthi, S. and Rupanagudi, S. R. (2012). Novel algorithm for segmentation and automatic identification of pests on plants using image processing. Third International Conference on Computing, Communication and Networking Technologies (ICCCNT'12), Coimbatore. pp. 1–5.

Perez-Ruiz, M. and Upadhyaya, S. K. (2012). GNSS in Precision Agricultural Operations. In: Elbahhar, F. & Rivenq, A. (eds.) *New Approach of Indoor and Outdoor Localization Systems*. London: Intech Open. pp. 3–26.

Shivaramaiah, N. and Dempster, A. (2009). The Galileo E5 AltBOC: Understanding the Signal Structure, *International Global Navigation Satellite Systems Society IGNSS Symposium*. Qld. pp. 1–13.

Titterton, D. and Weston, J. D. (2004). *Strapdown Inertial Navigation Technology*. Reston: AIAA.

Toho, H., Bock, H., Schueler, T., Junker, S. and Kiroe, A. (2012). Exploiting the Galileo E5 Wideband Signal for Improved Single-Frequency Precise Positioning, *Inside GNSS*. pp. 64–73.

Ueka, Y. and Arima, S. (2015). Development of Multi-Operation Robot for Productivity Enhancement of Intelligent Greenhouses: For Construction of Integrated Pest Management Technology for Intelligent Greenhouses. *Environmental Control in Biology*. 53(2). pp. 63–70.

Xia, C., Chon, T. S., Ren, Z. and Lee, J. M. (2015). Automatic identification and counting of small size pests in greenhouse conditions with low computational cost. *Ecological informatics*. pp. 139–146.

Sveučilište u Rijeci
POMORSKI FAKULTET
FACULTY OF MARITIME STUDIES
University of Rijeka

University of Zagreb
Faculty of Transport and Traffic Sciences

Royal Institute of Navigation
Science Technology Practice

12th Annual Baška GNSS Conference

A STUDY ON MULTI--CONSTELLATION GNSS POSITIONING PERFORMANCE IN TERMS OF MARITIME REQUIREMENTS

Serdjo Kos[1], **Barbara Pongračić**[2], **David Brčić**[1]

[1] University of Rijeka, Faculty of Maritime Studies, Rijeka, Croatia
e-mail: skos@pfri.hr (Corresponding author)

[2] Satellite Navigation And Remote Sensing (SNARS) Research Group, Beihang University, Beijing, China

Abstract

Satellite navigation represents official positioning mean in maritime navigation. Importance of Global Navigation Satellite System (GNSS) increases with the emerging number of the world fleet, standard and critical services as well as the development of autonomous vessels. Quality of the GNSS positioning performance can be assessed by positioning accuracy, availability and Dilution of Precision (DOP), latter representing the influence of satellite geometry. DOP values depend on the relative position of the receiver and visible satellites. The GNSS positioning error is approximately equal to the product of the respective DOP value and the ranging accuracy. In maritime navigation where vertical positioning component can be omitted, DOP is reduced to the horizontal determination (HDOP). Limit values are defined in respective Performance Standards provided by the International Maritime Organization (IMO). The aim is to state the improvement of GNSS performance regarding employment and combination of different GNSSs as related to GPS, being the most commonly used system in maritime navigation. GPS, GLONASS, Galileo and BeiDou observations from four stations located in Italy, Peru, China and the United States were used. These stations were chosen due to their locations and the availability of positioning from all operational GNSSs. For each location, all possible combinations between

satellite constellations were made. The HDOP values, single frequency positioning solutions in a horizontal plane and positioning availability were analysed for December 2017. Analyses of HDOP values confirm improvements in satellite positioning compared to GPS. An insufficient number of BeiDou satellites over the United States resulted in large HDOP values at the MDO1 IGS station (Fort Davis, USA). For the same reason, the best average HDOP values were observed at the JFNG station (Jiufeng, China). Although not fully operational. the BeiDou system improved positioning performance when it was combined with a GPS system, as proved at the AREG IGS station, located in Arequipa, Peru. Moreover, the GPS/BeiDou combination had better performance at JFNG and PADO (Padua, Italy) stations when compared with GPS/GLONASS combination.

Keywords: *global navigation satellite systems, satellite positioning accuracy, horizontal dilution of precision, maritime navigation, GNSS applications*

1. INTRODUCTION

IMO recognises GNSS as a system which meets the carriage requirements for position-fixing equipment as a part of the World-Wide Radionavigation System (A. 1046(27), 2011, MSC. 915(22), 2001). Emerging autonomous vessels increase the importance of GNSS positioning solutions. The purpose of specific application demands for the required accuracy and integrity of the system. Current and future standard and critical applications in maritime navigation are calling for trusty and reliable GNSS services (Thomas *et al.,* 2011, Filjar, 2011).

With the recent revitalisation of GLONASS constellation and two newly emerging constellations of BeiDou and Galileo systems, multi-constellation positioning became a trend. To provide a credible indication of global positioning and navigation performance under the current GNSS constellations, the four-constellation positioning quality and performance should be investigated. The motivation for the research is to assess the positioning performance and availability of the combination of different GNSSs. The aim is to state the improvement of the positioning quality, accuracy and availability by the employment of different systems as related to GPS, which still represents the primary satellite positioning system in maritime navigation.

GNSS performance was evaluated regarding DOP, positioning accuracy, the availability of visible satellites, and the percentage of time span over which the position solutions can be acquired. DOP and RMS indices were calculated as defined in available GNSS standards (US DOD, 2008, CCS, 2016, CSNO, 2013).

DOP depends on relative positions of the receiver and the satellites. Positioning availability and mean horizontal positioning errors were calculated considering all combinations involved. GPS solutions were compared with other individual systems and combinations.

This study provides an approach of multi-GNSS satellite positioning performance assessment. The paper concludes with summarised findings and preferable continuation of the research regarding multiple GNSS constellations and their positioning performance.

2. BACKGROUND

This chapter presents the main constellation parameters and status of GNSS systems at the time of writing. IMO performance standards are described regarding maritime policies' guidelines for navigation purposes.

With the use of a mask angle of 5°, Medium Earth Orbit (MEO) satellite footprint covers approximately 33.9 % of the Earth surface (US DOD, 2008). Main features of GNSS space segments are presented further.

Table 1. Constellation parameters of operational GNSS systems (IAC, 2018, Teunissen and Montenbruck, 2017, CSNO, 2013)

	GPS	GLONASS	BDS	Galileo
Inclination	55°	65°	55°	56°
Period of revolution	11h 58m 00s	11h 15m 44s	12h 53m 24s	14h 04m 42s
Ground track repeat cycle	2 orbits/1 day	17 orbits/ 8 days	7 days	17 orbits/10 days
Altitude	20 180 km	19 100 km	21 528 km	23 222 km

Figures 1-4 present ground tracks of satellites of each GNSS constellation.

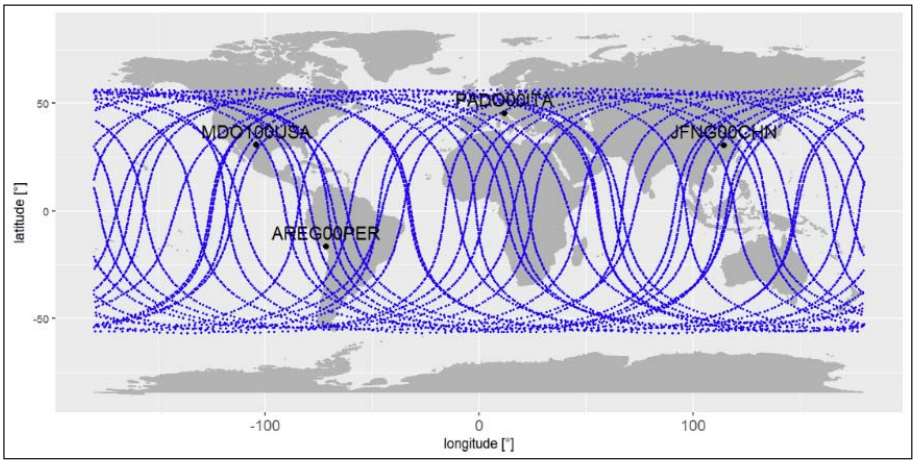

Figure 1. GPS constellation ground track during December 2017.
Authors according to (Johnston, Riddell and Hausler, 2017)

In general maritime navigation and respective applications, DOP is reduced to the horizontal determination (HDOP), limit values being required as defined in respective Performance Standards. Some of the navigation applications are port approach and restricted waters, automatic docking, automatic collision avoidance, ship-to-ship coordination (lightering), and aids to navigation management (A. 915(22), 2001).

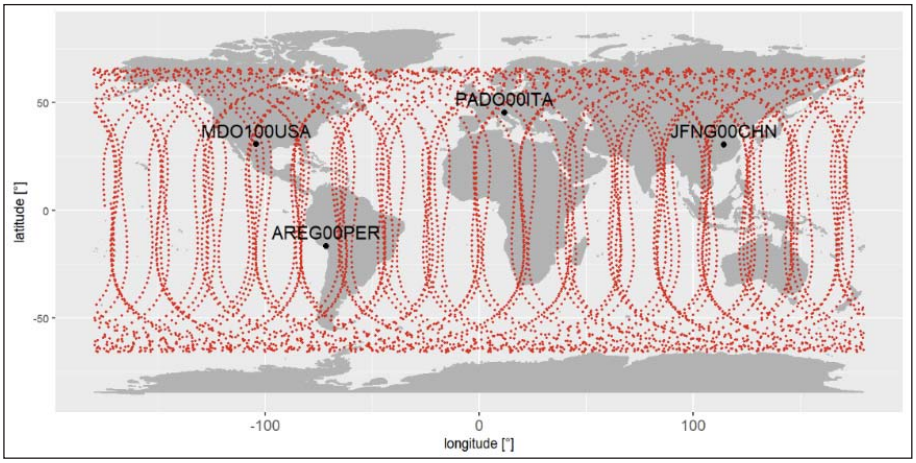

Figure 2. GLONASS constellation ground track during December 2017.
Authors according to (Johnston, Riddell and Hausler, 2017)

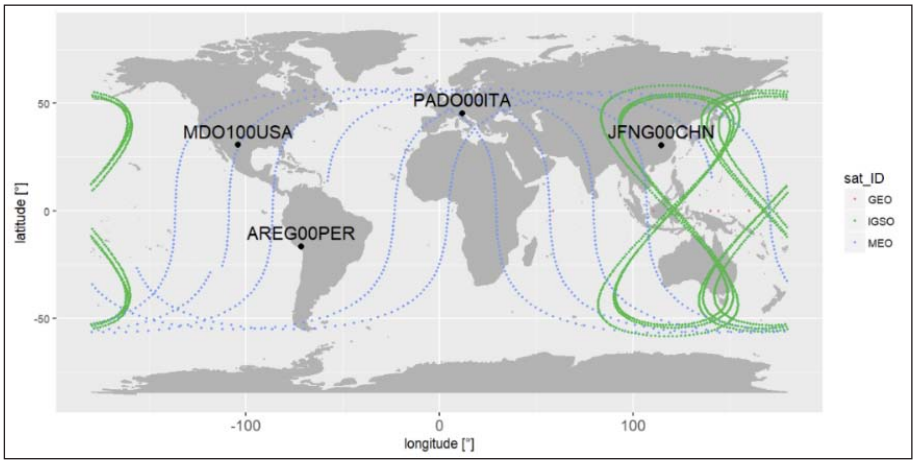

Figure 3. BDS constellation ground track during December 2017.
Authors according to (Johnston, Riddell and Hausler, 2017)

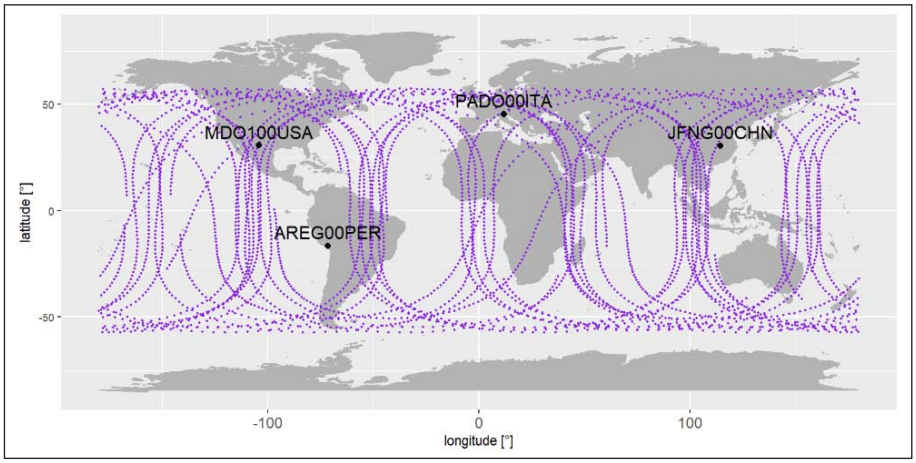

Figure 4. Galileo constellation ground track during December 2017.
Authors according to (Johnston, Riddell and Hausler, 2017)

Regarding full operability, the position should be determined with a HDOP equal or less than 4 or positioning dilution of precision of 6, for every system. For Galileo shipborne receiver, only PDOP limit value is defined equal or less than 3.5 (MSC. 233(82), 2006, MSC. 115(73), 2000, MSC. 53(66), 1996, MSC. 379(93), 2014). IMO recognises the combination of GPS and GLONASS equipment defined in

(MSC. 115(73), 2000), as well as other GNSSs (MSC. 401(95), 2015). Here, more stringent limit values for static and dynamic position accuracy are required; however, DOP requirements remain the same.

Maritime navigation GNSS applications are ranging from standard, where single frequency receivers satisfy the purpose, up to the provision of services requiring unquestioned integrity and high-accuracy (Thomas *et al.,* 2011, Brčić, 2012, A. 915(22), 2001, EC 308, 2010). Required performance for most specific maritime navigation critical applications is presented in Table 2 (A. 915(22), 2001).

Table 2. Minimum maritime user requirements for positioning: Search and rescue (SAR), hydrography, oceanography, marine engineering, construction, maintenance and management (MECMM) and aids to navigation management (ATONM) (A. 915(22), 2001)

Critical services and applications	System-level parameters			
	Accuracy (m)		Integrity	
	Horizontal	Vertical	Alert limit (m)	Time to alarm (s)
SAR	10	N/A	25	10
Hydrography	1 – 2	0.1	2.5 – 5	10
Oceanography	10	10	25	10
MECMM				
Dredging	0.1	0.1	0.25	10
Cable and pipeline laying	1	N/A	2.5	10
Construction works	0.1	0.1	0.25	10
ATONM	1	N/A	2.5	10

Service level parameters are required as follows (MSC. 401(95), 2015, A. 1046(27), 2011, A. 915(22), 2001). Speaking of general navigation categories, for navigation in ocean waters positioning with an error of ≤ 100 m is required with a probability of 95 %, signal availability of at least 99.8 % (per 30 days) and an update rate of computed position not less than 2 s. As for coastal, harbour and confined waters positioning error should not exceed 10 m with the service continuity of ≥ throughout 15 minutes.

3. EVALUATION OF MULTI-GNSS POSITIONING PERFORMANCE

Four stations were used in the study (Table 3); AREG (Arequipa, Peru), JFNG (Jiufeng, China), MDO1 (Fort Davis, USA) and PADO (Padua, Italy). These locations were chosen for several reasons: GNSS coverage, multi-constellation receivers and data availability during the assessed period. Regarding GNSS coverage, all possible cases were covered, e.g. the lack of visibility of BeiDou system in North America, its partial visibility in South America, visibility in areas where all of elaborated GNSSs provide their services, etc. All of the stations are part of the MGEX network (IGS 2018, Montenbruck *et al.,* 2017, Montenbruck *et al.,* 2014), meaning that they are equipped with required infrastructure for the reception, archiving and provision of satellite positioning data from all four constellations. Finally, all stations provide the most recent positioning data. GNSS constellation had 31 GPS satellites, 24 GLONASS satellites, 18 BeiDou satellites and 11 Galileo satellites in time of writing.

Table 3. Main features of employed IGS MGEX stations. Authors according to (Johnston, Riddell and Hausler, 2017)

Site ID	Location	Latitude	Longitude	Height (m)	GNSS
AREG	Arequipa, Peru	-16.465°	-71.493°	2489.34	GPS+GLO+GAL+ +BDS+SBAS
JFNG	Jiufeng, China	30.516°	114.491°	71.32	GPS+GLO+GAL+ +BDS+QZSS+SBAS
MDO1	Fort Davis, USA	30.681°	-104.015°	2004.48	GPS+GLO+GAL+BDS
PADO	Padua, Italy	45.411°	11.896°	64.70	GPS+GLO+GAL+ +BDS+QZSS+SBAS

IGS reference positions were used for deviations' determination. IGS site guidelines (IGS CB, 2013) require low multipath values (<0.3 m) and appropriate mounting of GNSS antenna regarding unobstructed sky and the possibility of tracking of a maximum of satellites. Locations and environments of employed IGS stations are presented in Figure 5.

Figure 5. Geographical features of AREG (upper left), JFNG (upper right), MDO1 (lower left) and PADO (lower right) IGS MGEX stations. Courtesy of ©Google Earth.

GNSS observation and navigation data were used as observed and archived in RINEX 3.02 format (US NGS, 2018, IGS MGEX, 2018, Dow, Neilan and Rizos, 2009). Single frequency positioning solutions were calculated using RTKLIB open source program package for satellite positioning with corresponding program library and RTKPOST application program for GNSS data post-processing.

The calculation of DOP values differs for single- and multi-constellation because of the different time scale of each system. Navigation (positioning) error can be expressed as (Teunissen and Montenbruck, 2017, Kaplan and Hegarty, 2006):

$$\sigma_T = \sigma_R \cdot DOP \tag{1}$$

where: σ_T ... total positioning (navigation) error, σ_R ... user equivalent range error, DOP ... dilution of precision.

Pseudorange to each visible satellite is (Subirana, Zornoza and Hernandez-Pajares, 2013):

$$R_i = \sqrt{\left(x_{S_i} - x_R\right)^2 - \left(y_{S_i} - y_R\right)^2 - \left(z_{S_i} - z_R\right)^2} + c\Delta t \tag{2}$$

where: R_i ... pseudorange R to the i-th satellite, where $i = 1, ..., n$, n ... number of satellites, $S(y_{S_i}, y_{S_i}, z_{S_i})$ ... coordinates of the i-th satellite, $R(x_R, y_R, z_R)$ ... coordinates of the receiver, c ... speed of light, and Δt ... the clock's offset.

Unit vectors between all visible GPS satellites and receiver form the matrix $\boldsymbol{H}_{GPS}$ containing partial derivatives of the range observations with the respect to the parameters (Dellago, Detoma and Duogo, 2003):

$$\boldsymbol{H}_{GPS} = \begin{bmatrix} \frac{x_{S_1} - x_R}{R_1} & \frac{y_{S_1} - y_R}{R_1} & \frac{z_{S_1} - z_R}{R_1} \\ & \vdots & \\ \frac{x_{S_n} - x_R}{R_n} & \frac{y_{S_n} - y_R}{R_n} & \frac{z_{S_n} - z_R}{R_n} \end{bmatrix}. \tag{3}$$

Receiver's clock offset is set by the vector $\boldsymbol{I}_{GPS}$:

$$\boldsymbol{I}_{GPS} = \begin{bmatrix} D_{t_1} = 1 \\ \vdots \\ D_{t_n} = 1 \end{bmatrix} \tag{4}$$

where: D_{t_i} ... clock offset of the receiver to the i-th satellite.

Matrix for range measurement residual equations for four or more satellites is composed of the unit vectors from the receiver to the satellite matrix $\boldsymbol{H}_{GPS}$ and the clock offset vector $\boldsymbol{I}_{GPS}$(Dellago, Detoma and Duogo, 2003):

$$\boldsymbol{A} = [\boldsymbol{H}_{GPS} \quad \boldsymbol{I}_{GPS}]. \tag{5}$$

The covariance matrix $\boldsymbol{Q}$ is:

$$\boldsymbol{Q} = (\boldsymbol{A}^{\mathrm{T}}\boldsymbol{A})^{-1} = \begin{bmatrix} NDOP & \cdot & \cdot & \cdot \\ \cdot & EDOP & \cdot & \cdot \\ \cdot & \cdot & VDOP & \cdot \\ \cdot & \cdot & \cdot & TDOP \end{bmatrix}. \tag{6}$$

Diagonal values represent variances of the estimated position. DOP components are:

$$GDOP = \sqrt{NDOP^2 + EDOP^2 + VDOP^2 + TDOP^2}, \tag{7}$$

$$PDOP = \sqrt{NDOP^2 + EDOP^2 + VDOP^2}, \tag{8}$$

$$HDOP = \sqrt{NDOP^2 + EDOP^2}, \tag{9}$$

where: *GDOP* ... geometric dilution of precision, *PDOP* ... positioning dilution of precision, *HDOP* ... horizontal dilution of precision.

The same analogy can be applied to calculate *DOP* from other GNSS systems, and forming matrices $\boldsymbol{H}_{GLO}$, $\boldsymbol{H}_{GAL}$, $\boldsymbol{H}_{BDS}$, and clock offset vectors $\boldsymbol{I}_{GLO}$, $\boldsymbol{I}_{GAL}$, $\boldsymbol{I}_{BDS}$. For the combination of systems, the additional *n* – dimensional null-vectors $\boldsymbol{O}_{GLO}$, $\boldsymbol{O}_{GAL}$, $\boldsymbol{O}_{BDS}$ are introduced. The design matrix $\boldsymbol{H}$ is (Dellago, Detoma and Duogo, 2003, Pan *et al.,* 2017):

$$\boldsymbol{H} = \begin{bmatrix} \boldsymbol{H}_{GPS} & \boldsymbol{I}_{GPS} & \boldsymbol{O}_{GPS} & \boldsymbol{O}_{GPS} & \boldsymbol{O}_{GPS} \\ \boldsymbol{H}_{GLO} & \boldsymbol{O}_{GLO} & \boldsymbol{I}_{GLO} & \boldsymbol{O}_{GLO} & \boldsymbol{O}_{GLO} \\ \boldsymbol{H}_{GAL} & \boldsymbol{O}_{GAL} & \boldsymbol{O}_{GAL} & \boldsymbol{I}_{GAL} & \boldsymbol{O}_{GAL} \\ \boldsymbol{H}_{BDS} & \boldsymbol{O}_{BDS} & \boldsymbol{O}_{BDS} & \boldsymbol{O}_{BDS} & \boldsymbol{I}_{BDS} \end{bmatrix} \tag{10}$$

Multi-constellation covariance matrix is:

$$\boldsymbol{Q} = (\boldsymbol{H}^{\mathrm{T}}\boldsymbol{H})^{-1}. \tag{11}$$

If the GNSS systems are inter-compatible, the $\boldsymbol{H}$ matrix can be simplified to:

$$\boldsymbol{H} = \begin{bmatrix} \boldsymbol{H}_{GPS} & \boldsymbol{I}_{GPS} \\ \boldsymbol{H}_{GLO} & \boldsymbol{I}_{GLO} \\ \boldsymbol{H}_{GAL} & \boldsymbol{I}_{GAL} \\ \boldsymbol{H}_{BDS} & \boldsymbol{I}_{BDS} \end{bmatrix} \tag{12}$$

Galileo and GPS broadcast time-offset, which can be used in the receiver since their time reference system is kept in the order of nanoseconds. For the research, it is assumed that GNSS systems are inter-compatible, as defined in (Dellago, Detoma and Duogo, 2003).

Single point positioning algorithm used for positioning solutions is described in detail in (Takasu, 2018). Usual GNSS receiver mask angles are 15°, 10°, 7.5°, 5°, 2°, and 0° (US DOD 2008). This parameter was set to 10°, which represents a compromise

between satellite availability and signal accuracy. All (15) possible combinations of satellite constellations were evaluated during 31 days of December 2017, with the calculation of respective HDOP values and single frequency positioning solutions over respective areas.

4. RESULTS AND DISCUSSION

Mean HDOP values for all stations and all system combinations are shown in Table 4 and on Figure 6, respectively. The best average HDOP values were measured at the JFNG station, while the worst values were at the MDO1 station. This is due to an insufficient number of BeiDou satellites over the USA. Station AREG had better HDOP values than MDO1 due to the visibility of several BeiDou satellites. Although the stand-alone BeiDou positioning at AREG station is not yet possible, HDOP values decreased when compared to the HDOP values of GPS solely. The combination of GPS and BeiDou already has better HDOP values at JFNG and PADO than the combination of the GPS and GLONASS.

Table 4. Mean HDOP values as calculated for each IGS station considering all possible GNSS combinations: BDS – BeiDou, GAL – Galileo, GLO – GLONASS, GPS – GPS, ALL – a combination of all systems.

System combination	Station			
	AREG	JFNG	MDO1	PADO
ALL	0.6449	0.5513	0.7918	0.6081
BDS	N/A	2.351	N/A	8.8446
BDS+GAL	8.369	0.9201	4.206	2.393
GAL	10.888	4.3559	4.206	22.39
GLO	8.755	1.589	7.929	3.871
GLO+BDS	6.198	0.7658	7.929	1.017
GLO+BDS+GAL	1.868	0.6795	1.297	0.8268
GLO+GAL	1.95	1.035	1.297	1.058
GPS	2.065	1.15	1.359	1.162
GPS+BDS	1.972	0.7275	1.359	0.8756
GPS+BDS+GAL	1.514	0.6431	1.0182	0.7456
GPS+GAL	1.557	0.8898	1.0182	0.9096
GPS+GLO	1.418	0.7801	0.9107	0.7753
GPS+GLO+BDS	1.385	0.5944	0.9107	0.6661
GPS+GLO+GAL	1.226	0.6869	0.7918	0.6891

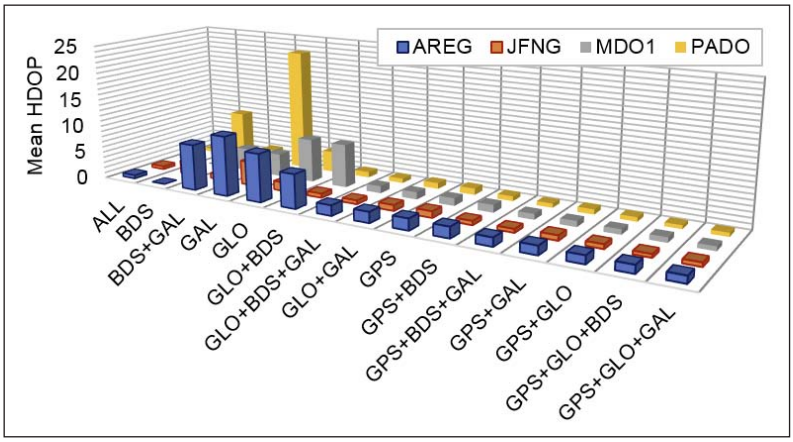

Figure 6. Mean HDOP values of the different combination of systems: BDS – BeiDou, GAL – Galileo, GLO – GLONASS, GPS – GPS, ALL – a combination of all systems

In Figure 7, mean HDOP values for the case *all* (combination of all four systems) are shown.

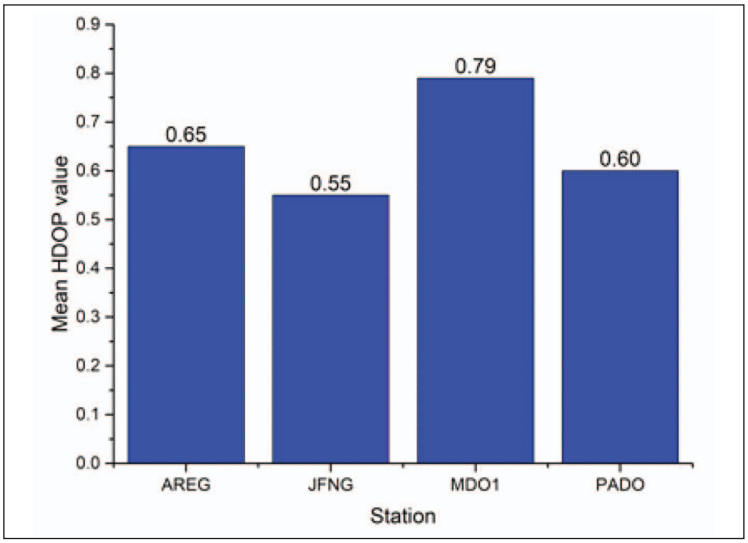

Figure 7. Mean HDOP values – a combination of all systems

Mean HDOP values were calculated by integrating GPS data with all other GNSSs, as presented in Figure 8. This was conducted to present the HDOP improvement of GPS when supported with another system. JFNG station had the best HDOP values.

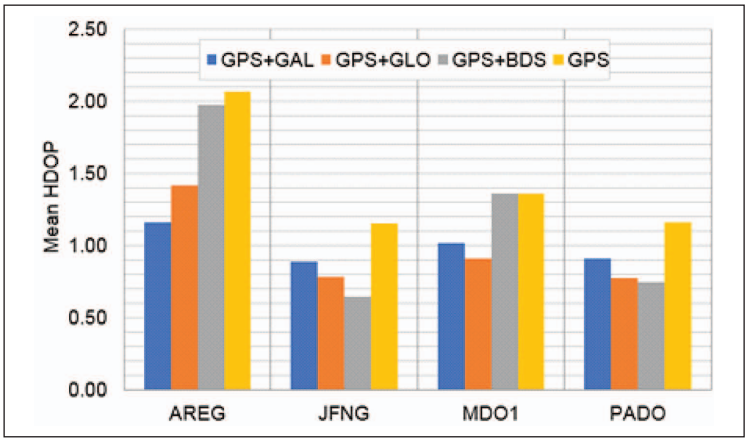

Figure 8. Mean HDOP values of the combination of GPS with another GNSS system

Positioning availability and horizontal positioning errors are presented in Figure 9.

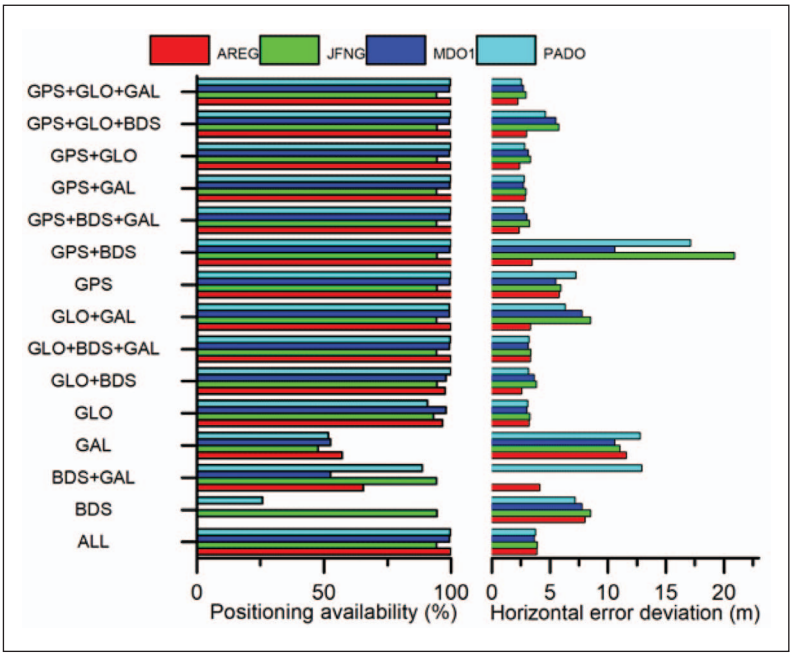

Figure 9. Positioning availability (left image) and mean horizontal error deviation (right image) as calculated on AREG (red), JFNG (green), MDO1 (blue) and PADO (cyan) stations

Positioning with BeiDou system solely was not possible at MDO1 and AREG stations, while at the PADO station it was possible for 25.7 % of the assessed period. At the JFNG station, positioning was always possible using BeiDou. Galileo positioning was possible for 57.2 % of the time at the AREG station, 47.6 % at JFNG station, 52.6 % at the MDO1 station, and 51.8 % at the PADO station.

Positioning deviations in the horizontal plane are the smallest for the combination of all systems at the JFNG station (2.22 m) which corresponds to the smallest average values of HDOP.

As of fully operational GNSSs, GPS and GLONASS positioning performance exceeds the requirements. For the time being, Galileo and BeiDou are still partially operational to meet those requirements. However, when integrated with other operational systems, Galileo and BeiDou contribute to overall improvement of GNSS services both regarding coverage of specific areas and positioning performance and availability.

5. CONCLUSIONS

Improvement of satellite positioning performance was analysed considering GNSS single and multi-constellations. It has been conducted regarding satellite coverage and availability using DOP and RMS in the horizontal plane. The study was conducted as the presentation of improvement of different GNSS combinations regarding satellite positioning for maritime navigation.

Presented results are reflecting the current state of GNSS. The assessment of satellite positioning performance as conducted should be carried out frequently as the systems further develop. This can be achieved using available IGS and other satellite positioning data, especially in coastal areas, in function of the reliability of emerging maritime services and applications based on satellite navigation.

The results showed that combined GNSS positioning exceeds minimum requirements for maritime GNSS equipment. It opens a basis for consideration of Performance Standards' revision for maritime policy and requirements for future global navigation satellite systems.

ACKNOWLEDGEMENTS. Research activities presented in this paper were conducted under the research project *Research into the correlation of maritime-transport elements in marine traffic: Satellite navigation segment*, supported by the University of Rijeka, Croatia.

References

Brčić, D. (2012). Ensuring sustainability through utilization of satellite navigation technology. In: Zanne, M. and Bajec, P. (eds.) *Proceedings of the 2012 International Conference on Transport Sciences (ICTS)*. Portorož: Faculty of Maritime Studies and Transport. pp. 1–14.

China Classification Society (CCS). (2016). *N-10 Multi-system Shipborne Radionavigation Receivers*. Beijing: CCS.

China Satellite Navigation Office (CSNO). (2013). *BeiDou Navigation Satellite System Signal in Space Interface Control Document: Open Service Signal*. Beijing: CSNO.

Dellago, R., Detoma, E. and Luongo, F. (2003). Galileo-GPS interoperability and compatibility: a synergetic viewpoint. *Proceedings of ION GPS/GNSS 2003*, 9-12 September 2003, Portland, OR, USA, pp. 542–548.

Dow J. M., Neilan R. E. and Rizos C. (2009). The International GNSS Service in a changing landscape of Global Navigation Satellite Systems. *Journal of Geodesy*. 83(3-4). pp. 191–198.

European Commission (EC). (2010). *COM(2010)308: Action Plan on Global Navigation Satellite System (GNSS) Applications*. Brussels: EC.

Filjar, R. (2011). GNSS: What can go wrong and what are the risks? *Risk Management In GNSS Malfunctioning Consultation meeting '11*. Rome: International Institute for the Unification of Private Law (UNIDROIT).

Information and Analysis Center for Positioning, Navigation and Timing (IAC). (2018). Available at: https://www.glonass-iac.ru/en/guide/beidou.php#og, accessed 31 January 2018.

International GNSS Service Infrastructure Committee Central Bureau (IGS CB). (2013). *IGS Site Guidelines*. Pasadena: IGS and JPL.

International GNSS Service (IGS). (2018). The Multi-GNSS Experiment and Pilot Project (MGEX). Available at: http://mgex.igs.org/index.php#MGEX, accessed 21 March 2018.

International GNSS Service Multi-GNSS Experiment and Pilot Project (IGS MGEX). (2017). GNSS observation data in RINEX format. Available at: ftp://cddis.gsfc.nasa.gov/pub/gps/data/campaign/mgex/daily/rinex3, accessed 23 January 2017.

International Maritime Organization (IMO). (1996). *Resolution MSC. 53(66): Adoption of the revised performance standards for shipborne GLONASS receiver equipment*. London: IMO.

International Maritime Organization (IMO). (2000). *Resolution MSC. 115(73): Adoption of the revised performance standards for shipborne combined GPS/GLONASS receiver equipment*. London: IMO.

International Maritime Organization (IMO). (2000). *Resolution MSC. 112(73): Adoption of the revised performance standards for shipborne Global Positioning System (GPS) receiver equipment*. London: IMO.

International Maritime Organization (IMO). (2006). *Resolution MSC. 233(82): Adoption of the performance standards for shipborne Galileo receiver equipment*. London: IMO.

International Maritime Organization (IMO). (2015). *Resolution MSC. 401(95): Performance Standards for Multi-system Shipborne Radionavigation Receivers.* London: IMO.

International Maritime Organization (IMO). (2011). *Resolution A.1046 (27): Worldwide Radionavigation System.* London: IMO.

International Maritime Organization (IMO). (2014). *Resolution MSC. 379(93): Performance standards for shipborne Beidou satellite navigation system (BDS) receiver equipment*. London: IMO.

International Maritime Organization (IMO). (2001). *Resolution A.915 (22): Revised maritime policy and requirements for a future Global Navigation Satellite System (GNSS)*. London: IMO.

Johnston, G., Riddell, A., Hausler, G. (2017). The International GNSS Service. In: Teunissen, Peter J. G. & Montenbruck, O. (Eds.) *Springer Handbook of Global Navigation Satellite Systems. 1st Edition.* Cham: Springer International Publishing. pp. 967–982. doi:10.1007/978-3-319-42928-1.

Kaplan, E. D. and Hegarty, C.J. (eds.) (2006). *Understanding GPS: Principles and Application*. Second edition. Boston: Artech House.

Montenbruck, O. *et al*. (2014). IGS-MGEX: Preparing the Ground for Multi-Constellation GNSS Science. *InsideGNSS*. 9(1). pp. 42–49.

Montenbruck, O. *et al*. (2017). The Multi-GNSS Experiment (MGEX) of the International GNSS Service (IGS) – Achievements, Prospects and Challenges. *Advances in Space Research.* 59(7). pp. 1671–1697.

Pan, L. *et al*. (2017). Satellite availability and point positioning accuracy evaluation on a global scale for integration of GPS, GLONASS, BeiDou and Galileo. *Advances in Space Research*, doi: 10.1016/j.asr.2017.07.029.

Subirana, J. S., Zornoza J. M. J. and Hernandez-Pajares, M. (2013). *GNSS Data processing, Volume I: Fundamentals and algorithms*. Noordwijk: ESA Communications.

Takasu, T. (2018). RTKLIB: An Open Source Program Package for GNSS Positioning. Available at http://www.rtklib.com, accessed 22 April 2018.

Teunissen, P. J. G. and Montenbruck, O. (eds.) (2017). *Springer Handbook of Global Navigation Satellite Systems*. Cham: Springer Nature.

Thomas, M. *et al.* (2011). *Global Navigation Space Systems: Reliance and Vulnerabilities*. London: The Royal Academy of Engineering.

US National Geodetic Survey (US NGS). (2017). *Continuously Operating Reference Stations (CORS): GPS navigation messages in RINEX format*. Available at: https://www.ngs.noaa.gov/CORS/standard1.shtml, accessed 23 January 2017.

USA Department of Defense (US DOD). (2008). *Global Positioning System: Standard Positioning Service Performance Standard*. Washington, DC: US DOD.

Sveučilište u Rijeci
POMORSKI FAKULTET
FACULTY OF MARITIME STUDIES
University of Rijeka

University of Zagreb
Faculty of Transport
and Traffic Sciences

Royal Institute of Navigation
Science Technology Practice

12th
Annual
Baška GNSS
Conference

SENSING SDR-BASED GNSS JAMMERS

Matej Bažec, Franc Dimc

University of Ljubljana, Faculty of Maritime Studies and Transport, Portorož, Slovenia

e-mail: matej.bazec@fpp.uni-lj.si (Corresponding author)

Abstract

The increased use of satellite-navigation-based systems (tracking, geo-fencing, fleet optimization, landmark identification, location-based gaming, etc.) has led to the development of devices that are capable of interfering with them or even fraudulently impersonating them. The talk is about GNSS (almost exclusively GPS) jammers and spoofing devices, respectively. The former are of particular concern because they are mass-produced and have a relatively low price, although they are illegal in most countries. GPS jammers typically work by producing a strong noise signal (virtually all produce chirp signals around the main L1 band) that drowns out the genuine satellite signal. Although the jamming signal needs to be strong close to the device being attacked, the signal decreases rapidly with an increasing distance from the jammer. This presents a challenge when it comes to detecting such a signal. In this study, a solution based on software-defined radio (SDR) is presented. SDR is essentially a device that acquires a raw electromagnetic signal in the frequency band of interest, converts it into digital form and then sends it to a computer. All the post-processing is then done using the software. Such an approach has many advantages because it provides a detailed insight into the jamming signal. Since a large amount of data acquired by such a system cannot all be saved on a mass storage device, it is essential to spot the presence of a disturbing signal in order to save just the relevant data that is suitable for subsequent analysis. In the first part, the various algorithms used to discriminate the signal will be presented. In the second part, a proposal for classifying the jammers will be described. Although virtually all the jammers emit chirp signals centered on the GPS L1 frequency (1575.42 MHz), their stability is

typically very poor. For this reason, interesting patterns in their power spectral distribution can be observed on different time scales, providing a means for their classification. The data was acquired in a controlled environment, as well as at the roadside.

Keywords: *jamming detection, software-defined radio, spectrum analysis*

1. INTRODUCTION AND BACKGROUND

Satellite-navigation-based services have expanded rapidly in the past two decades, mainly due to the significant drop in the price of GPS-acquisition devices. The arrival of smart phones with embedded GPS receivers also gave this expansion an extra boost. Many of the GPS services have increased the level of control (mostly legitimate, but illegitimate as well) over the current position of vehicles and people. For example, a cargo-fleet owner is able to track the position of the company's vehicles. A construction company can confine its building machines to a particular building site. A car owner is able to know the exact position of his/her car, and so be alerted about its movement in the case of attempted theft. There have also been plans to use satellite positioning for highway tolls.

Such a level of control has stopped abuse by drivers, preventing them from doing extra work on their own with the company's vehicle. On the other hand, the potential for abuse of such systems has increased concerns about protecting the privacy of individuals. In addition, with an ever-increasing number of applications designed to know a particular current position, the demand to somehow circumvent this technology has arisen.

The market has responded with the mass production of low-cost devices for jamming GPS signals. Although the legislation about whether owning such a device represents an offense varies from country to country, it is illegal to use them almost everywhere (for example, we required special permission from the Slovenian telecommunication authority AKOS in order to perform these experiments). In recent times there have also been many events that could be attributed to GPS signal spoofing. However, such devices are limited to the research and military domains, and as such, they are less accessible, and their impact can be considered as negligible, so far.

The detection of jamming, its monitoring, resilience and even mitigation has been addressed many times by academic and industrial research, e.g. Thombre (2018), Glomsvoll (2017), Borio (2018) and De Wilde (2018). As such, the research

presented in this paper should not be seen as yet another attempt to detect and classify jamming devices. In order to enhance usability, a data-processing algorithm must be selected to preserve the processor's load low. Due to the very low cost of the equipment involved, our configuration aims to bring the receivers to a price level that could allow the mass installation of detection devices for the purpose of jammer localization, time-pattern analysis, etc.

Keeping this in mind, a low-end software-defined radio (SDR) connected to an embedded device was sought. For that purpose, a RTL 2830U chipset-based USB dongle (the popular RTLSDR) was chosen with the R820T2 tuner connected to a Raspberry PI (RPI). According to the tuner's specification, the frequency limit is set slightly above 1 GHz, which is not surprising, since these tuners are manufactured for use with DVB-T receivers. However, it has been shown that if the proper precautions are put in place (heat dissipation), then it can be tuned up to 1.6 GHz and even more, although with a drastic increase in the level of noise.

Another disadvantage of using such a configuration is that the sampling rate of the in-phase and quadrature signals is limited to 2 MHz if the dropped samples are to be kept below some reasonable value. However, the majority of GPS jammers typically work in the frequency band from 10 to 20 MHz around L1. Keeping this in mind, it is impossible to reproduce the original jamming signal from the sample. However, effects on a larger time scale can easily be observed, and it will be shown that some straightforward classification based on this analysis can be performed.

The detector was first tested on a local road near Črnotiče, Slovenia. Then it was set up at a toll station on a Slovenian highway. In order to identify and to get rid of detector artifacts a parallel BladeRF SDR acquisition device with a larger sampling rate and a better ADC (analog to digital converter) resolution was connected to a computer.

2. SETTING THE ACQUISITION THRESHOLD

Although the RTLSDR ADC resolution is only 8 bit and the used sampling rate was 2 MHz, it produces 4 MB of data per second. This is just enough to fill the local storage capacity within a few hours. For this reason, a simple algorithm (a RPI has limited computational power) was sought in order to be able to efficiently identify a jamming event. The positive outcome of the algorithm would then identify the jamming event and store the signal for subsequent analysis.

Roughly speaking, SDR devices receive the radio signal in chunks (to be more correct, the SDR driver core library implementations use this approach). In this case a chunk of twice the 262144 samples was used, matching a sampling time of 0.13 ms. These samples could then be used as the input to an algorithm that would decide whether the signal in the chunk is jammed and trigger the saving procedure.

For this purpose, four algorithms were chosen. Virtually all the jammers drown out the genuine signal in a very intrusive way by emitting a noise-like signal (typically a chirp) that is an order of magnitude stronger than the typical background. This should be done because the Gold code is very prone to noise. If a more sensible approach was used, targeting the GPS's PRN (pseudo random number) sequence itself, then the power emitted could be much lower. However, this would require a more intelligent jamming approach. On the other hand, if the jamming signal is supposed to be strong locally, close to the GPS receiver, it does not mean that the same signal is strong at the detector's location, which could be a hundred meters away.

That being said, it seems a logical choice to base the algorithms on the received power. Two of the triggering algorithms are straightforward. The first calculates the total power T of the chunk:

$$\sum_{n=0}^{N-1} |I_n + iQ_n|^2 = \sum_{n=0}^{N-1} I_n^2 + Q_n^2 \tag{1}$$

where: T... the algorithm level, I_n, Q_n ... the in-phase and the quadrature signal samples, respectively, and N... the number of samples in a chunk.

The other algorithm uses just the maximum power in the chunk:

$$\boldsymbol{T = max(I_n^2 + Q_n^2)}. \tag{2}$$

Of course, the threshold value is yet to be selected. This will be addressed shortly.

The third algorithm is slightly more sophisticated. The SDR receivers usually have an artifact that produces higher values at the intermediate frequency, known as the DC offset. This is because it is hard to get rid of the DC component of the mixer's output completely. As a consequence, the total measured power of the chunk will be much greater than the signal's total power in the same frequency and time window. This means that a weak jamming signal would produce a much smaller relative

measured power increment than it is in reality. In order for the increment to be more pronounced, the DC component was carried out in the total power computation.

It might look as if such an approach would increase the computational complexity. However, this is not the case. Two properties of the Fourier transform (FT) should be taken into account. First, the Parseval's identity can be used for the total power computation; instead of calculating the power in the frequency domain, it can be performed in the time domain. And second, the DC component that is to be removed from the total power is just the total sum of all the collected samples. With this approach, there is no need to involve the Fourier transform directly. Instead, the out-of-band power is calculated as:

$$T = \sum_{n=0}^{N-1} |I_n + iQ_n|^2 - \frac{1}{N}\left|\sum_{n=0}^{N-1} I_n + iQ_n\right|^2 \tag{3}$$

The last algorithm is computationally more intensive since it uses the FT. As such, it should only be used in combination with some of the simpler algorithms that would serve as a preliminary test, while the algorithm itself could be used as a decisive trigger mechanism. It is based on the maximum power density in the frequency domain, but with the preselected frequency bands omitted. In such a way the detector is able to exclude some interference from various sources that are quite frequent, but very narrow, weak and always at a selected frequency.

Figure 1. Preparations for the jamming-detection tests at Črnotiče

Figure 2. Location of the testing site near Črnotiče, Slovenia

To select the most efficient algorithm a test was performed on a local road near Črnotiče, Slovenia (Figures 1 and 2). The detector was set near the road in the middle of a straight section. The jammer was then put in a car that was driven at various speeds, passing by the detector. In order to compare all four algorithms, all the values were normalized so that their initial position was 1. In the presented results (Figures 3 and 4) the car was driving in the direction of Podgorje at 80 km/h.

It is clear from Figures 3 and 4 that the increment of the triggering parameter in the first algorithm is only 10 %, in the second it is 2.4 times, and in the last two it is almost 40 times. The height of the maximum also has some implications for how low the threshold can be set. It is desirable to be as low as possible, since this would mean a more sensitive detector. The background noise and its stability should play an important role in setting the minimal boundary. While in the case of the first algorithm a value of 1.05 seems a bare minimum, with no margin for false-positive detections, the values of 1.2, 1.5 and 2 for the other algorithms, respectively, seem to provide quite a safe value (Figure 4).

Assuming the speed of the car to be 80 km/h and using the above values for the threshold, an estimate for the detection range can be calculated: 5 m, 20 m, 30 m and 20 m for each of the algorithms, respectively. Of course, in the case of the last three algorithms, the threshold value can be slightly lowered, thereby improving the range but raising the window for eventual false-positive events.

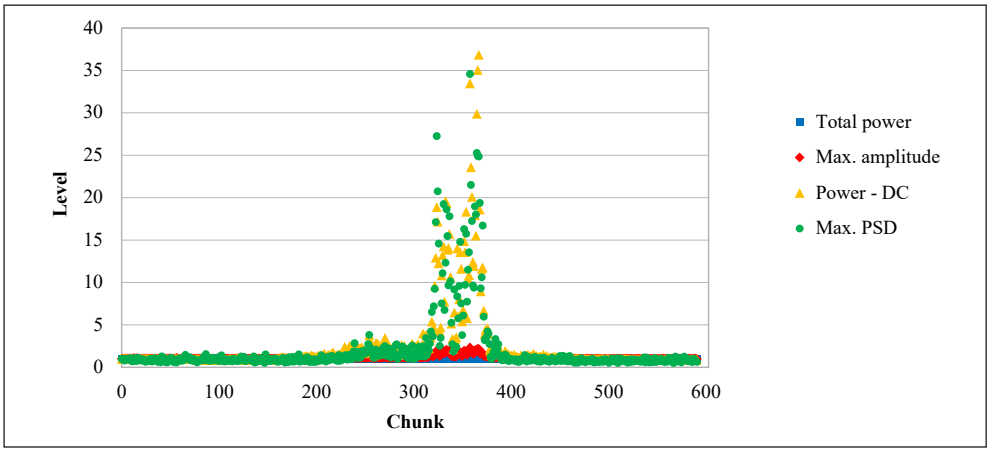

Figure 3. Comparison of the tested triggering mechanisms. The superiority of the last two is obvious. A chunk is equivalent to 0.13 s.

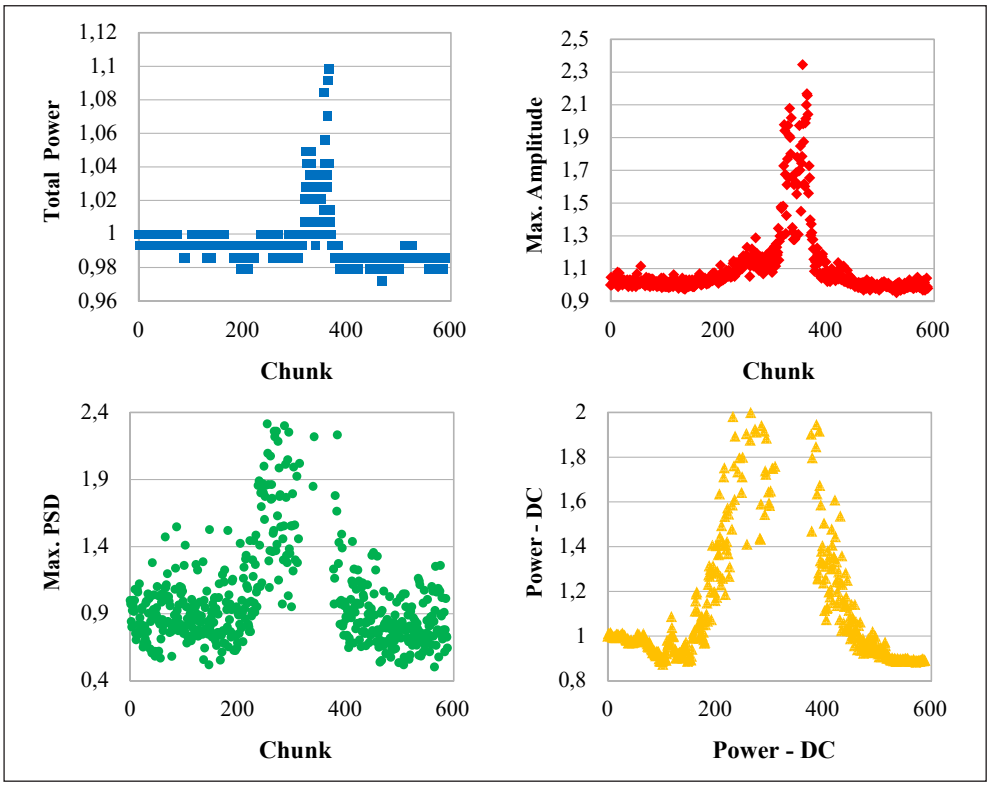

Figure 4. A detailed view of a particular triggering mechanism. Note that the scale for the last two is magnified in order to demonstrate their superiority.

It seems a reasonable choice to use the third algorithm, i.e., the total power with the DC component removed. With the threshold set from 20 % to 50 % above the background, the detector is supposed to be on the safe side for false-positives. The idea was to modify the background dynamically. In this case, the threshold could be set as low as 10 % or even less. However, it has not yet been implemented.

3. DETECTING JAMMERS

After the initial testing, the detector was put close to the Log toll station from 14 February 2018 to 13 March 2018 on the Slovenian A1 highway. The RPI was connected to the internet via an SSH (secure-shell protocol) channel. A cron-job script ran once a day to upload the measured data to a storage server, where the data was post-processed. A log periodic antenna was connected to the detector.

Based on the reasoning in the previous section, it seemed a sensible choice to use the total power of the acquired chunk with the DC component removed as the triggering mechanism. If two or more consecutive chunks exceeded the given threshold, they were merged and treated as a single event.

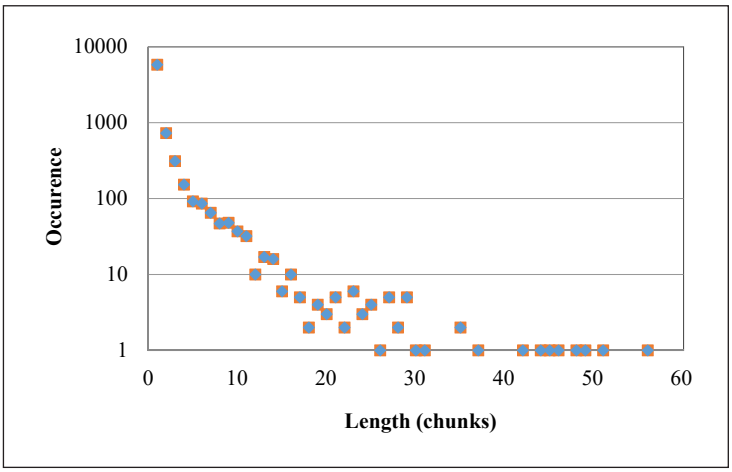

Figure 5. Distribution of events according to their length

A length-based distribution was then constructed (Figure 5). A longer event could mean slower driving through the toll station, driving on a lane that is closer to the detector position or a stronger emitted signal. If it is assumed that all three cases are uncorrelated, then the jammer emitting power distribution can be expected to have

a similar shape. However, the assumption could be too rough, since the trucks have to drive on the outermost lane (the closest to the detector or the most distant, depending on the driving direction). Furthermore, they had to make a stop in order to proceed with the payment (although this situation has changed since the test were carried out), while cars can just drive through.

4. DETECTED SIGNAL CLASSIFICATION

Some of the acquired signals were manually inspected in order to find some of the most characteristic patterns. It should be stressed again that the sampling rate of the detector (2 mega samples per second) does not allow for detailed signal analysis. It is not expected to be able to extract the jamming signal's shape (usually a chirp-like signal). Instead, it aims at retrieving some kind of instability, oscillation, etc. on a time scale that does not make it possible to see all the details of the signal, but rather its mid-scale average.

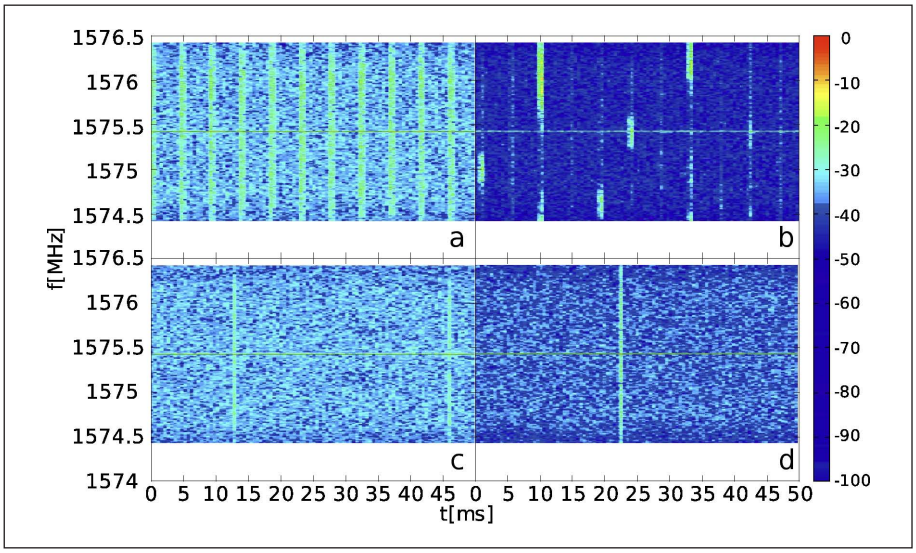

Figure 6. Waterfall representation of the four classes of detected jamming signals

As can be seen on Figure 6, there are four major classes found. The first class (type *a* in the figure) showed a periodic oscillation of the power of the emitting signal with a period having an order of magnitude of a few tens of milliseconds. However, the frequency distribution was almost even within those peaks as well as outside of them.

The signals in the second class (type *b*) were jammed only in short pulses (approximately 1 ms). The frequency distribution of these pulses had very pronounced maxima, and it fell rapidly through the rest of the frequency band. The third class (type *c*) of jammers emitted almost evenly in time and frequency, with eventual randomly dispersed peaks. The fourth class (type *d*) is made of single short time pulses. It is believed that these signals do not originate from intentional jamming sources since the signal is too short to jam the GPS signal effectively. Nevertheless, they could still reduce the precision of the position.

Unfortunately, the above classification was performed using manual inspection of approximately 100 events. In order to efficiently classify all of the acquired samples, an automatic pattern-recognition algorithm would be needed. In this way, some other classes could be found as well. The development of this algorithm is currently in progress and is part of our current research.

5. CONCLUSION

It has been shown that even with simple, low-cost equipment a jamming detector can be constructed that is able to make some basic classifications of the jammers. However, some work remains to be done.

So far, not much attention was given to the antenna. Although it is known that the genuine GPS signal is circularly polarized (in order to minimize the effect of a single reflection), this does not mean that the same holds for the jamming signal. That raises the question of an optimal choice for the antenna. As mentioned earlier, an automatic classification algorithm is yet to be developed.

Once the above issues are solved, the low price of such a configuration would make it possible to construct an array of detectors, allowing for the jammer's localization. Such an approach would open many issues and is far from being trivial. However, it would lead to many possible applications.

ACKNOWLEDGEMENTS. The authors would like to thank Mr. Marko Korošec from the Motorway Company in the Republic of Slovenia (DARS) for providing all the needed support. An authorization for the tests near Črnotiče issued by the Agency for Communication and Services of Republic of Slovenia (AKOS) is acknowledged. For the loan of the Blade RF the European Commission Joint Research Centre is gratefully acknowledged.

References

Thombre, S. *et al*. (2018). GNSS Threat Monitoring and Reporting: Past, Present, and a Proposed Future. *The Journal of Navigation*. 71. pp. 513–529.

Borio, D., Li, H. and Closas, P. (2018). *Huber's Non-Linearity for GNSS Interference Mitigation*. *Sensors*. 18(7), 2217; https://doi.org/10.3390/s18072217.

Glomsvoll, O. and Bonenberg, L. K. (2017). GNSS Jamming Resilience for Close to Shore Navigation in the Northern Sea. *The Journal of Navigation*. 70. pp. 33–48.

De Wilde, W., Cuypers, G. and Willems, T. (2018). Interferentie en Spoofing Tegenmaatregelen in Septentrio Ontvangers, *Workshop GNSS Interferentie en Authenticatie*, 31 January 2018, Haarlem. Available at: http://www.navnin.nl/new/2017/12/26/workshop-gnss-interferentie-en-authenticatie-3112018-haarlem/ http://www.navnin.nl/new/wp-content/uploads/2018/02/WSIA-3-Septentrio-NIN-Interferentie-en-Spoofing_SUBMITTED.pdf, accessed 18 August 2018.

12th Annual Baška GNSS Conference

PARTICULARITIES OF DETERMINING THE VESSEL POSITION, COURSE AND SPEED AND THE IONOSPHERIC ERROR BY USING DUAL-BAND GLONASS RECEIVERS

Serdjo Kos[1], **Mario Bakota**[2], **David Brčić**[1]

[1] University of Rijeka, Faculty of Maritime Studies, Rijeka, Croatia

[2] University of Split, Faculty of Maritime Studies, Split, Croatia
e-mail: mbakota@pfst.hr (Corresponding author)

Abstract

The paper presents the application of the pseudo-spatial model of the GLONASS system in determining the navigation parameters of the vessel's movement together with the applied ionospheric model accuracy. The atmosphere affects the signal reception causing signal delay, which leads to the error of determining the navigation parameters of the ship, with ionosphere causing the greatest impact on error values. By forming and solving the system in which the number of equations corresponds to the number of visible satellites, with the input data of pseudo-range, the constant error of distance measurement and the known satellite coordinates, the current position of the vessel is obtained. Differentiating this system of equations results in a system that gives the velocity of the vessel concerning the three spatial coordinates. By reducing velocity change with respect to the two spatial coordinates, the final speed of the vessel is obtained. Utilizing a known velocity of the vessel with respect to the x and y coordinates, the direction of navigation is also possible to be determined. Various satellite systems with different mathematical algorithms predict the state of the ionosphere and the value of the incurred error. Dual-band receivers of the GLONASS system perform simultaneously receiving, processing and comparison of signals at two frequencies to which the ionosphere has a different level of interaction.

Keywords: *ionospheric error, GLONASS, dual-band receiver, pseudo-Doppler frequency*

1. INTRODUCTION

The introduction of navigation satellite systems has enabled the real-time positioning of vessels, along with their speed and course. The accuracy of the obtained data is affected by errors generated by satellite systems (error in inter-satellite synchronisation, ephemeris error), errors due to signal propagation through the atmospheric layers (tropospheric error, ionospheric error), and errors occurring while receiving signals (multipath error and noise error). Various systems of satellite constellation determine, in various ways, the size of atmospheric errors, with the ionospheric error being the most relevant (Anđelini, Lučić and Filjar, 2016), The Global Positioning System (GPS) makes use of Klobucharev model, the Galileo system uses Nequick model for determining the errors caused by ionosphere, whereas the EGNOS model is applied for determining the ionospheric impacts at individual locations across Europe.

This paper provides an insight into determining a vessel's course and speed by using the *GLObalnaya NAvigationnaya Sputnikovaya Sistema* (GLONASS) navigation system and into ways of determining ionospheric errors and their values using dual-band GLONASS receivers. Also, one of this study's objectives is to establish whether the position given by the dual-band GLONASS receiver is accurate enough for potential application in ocean navigation (excluding offshore vessels).

2. GLONASS OVERVIEW

Global Navigation Satellite System (GNSS) consists of different satellite networks, emitting radio signals for navigation and positioning anywhere in the world. The GNSS will incorporate four satellite networks: existing GPS and GLONASS, and after reaching global coverage, GALILEO and BEIDOU. The importance of GNSS reflects in fact, that despite that systems differ due to jurisdiction and management (military and civilian), civilian users can freely use it without any hesitation regarding the origin of each system. GNSS offer their common compatibility and operability even those systems possess different technical characteristics. As a main principle, all satellite systems consist of four segments: space segment, the medium of propagation, the control segment and user segment.

GLONASS consists of no less of 24 satellites (2018), equally positioned in three orbits with the 120° between each equatorial plane, and with the nominal altitude of 19,100 km (RSS, 2016). In each band of GLONASS-M satellites, 12 pairs of carrier

frequencies are used for 24 satellites. The signals of satellites on the opposite sides of the globe, when satellites operate at the same frequencies, will be separated superficially due to spatial and Doppler selection and will not interfere with each other. It enables a reduced number of used frequencies.

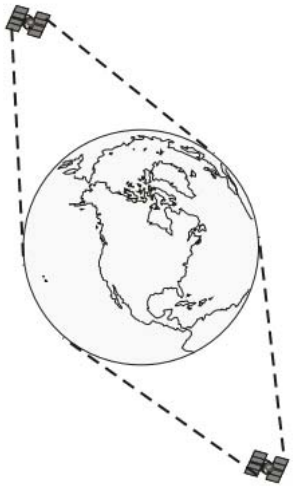

Figure 1. Antipodal position of GLONASS satellites. Source: (Langley, 2007)

GLONASS-M uses the Frequency Division Multiple Access (FDMA) method of signal separation, which is the main difference from GPS and GALILEO that use Code Division Multiple Access (CDMA). FDMA method provides more noise immunity (Gorobtsov *et al.,* 2016). This enables that all GLONASS satellites emit the same code at different frequencies. Carrier frequencies of GLONASS signals are located in two radio bands: L1 band from 1598.0625 to 1604.25 MHz with the step size between the frequencies Δf_1 = 0.5625 MHz, and L2 band from 1242.9375 to 1247.75 MHz with step Δf_2 = 0.4375 MHz (IAC, 2018).

The following relations determinate the nominal values of the carrier frequencies:

$$f_1 = f_{10} + \Delta k f_1 \tag{1}$$

$$f_2 = f_{20} + \Delta k f_2 \tag{2}$$

where: f_{10} = 1602 MHz, f_{20} = 1246 MHz, k = -7, ..., 4... a conditioned serial number of the carrier frequencies f_1 and f_2.

It enables satellites to emit signals on their frequency, separated by multiples of 562.5 and 437.5 kHz from the frequency of other satellites.

The wavelengths are, respectively λ_{10} = 18.72 cm, λ_{20} = 24 cm.

Except for differences in signals features, other significant differences between GLONASS and GPS are in features C/A-code Navigation Message parameter, given in Table 1.

Table 1. Main differences in C/A-code Navigation Message parameter (Langley, 2007)

	GLONASS	**GPS**
Technique for broadcast satellite ephemeris	Geocentric Cartesian coordinates and their derivatives	Keplarian orbital elements and perturbation factors
Time reference	UTC (SU)	UTC (USNO)
Position reference (geodetic datum)	PZ-90	WGS 84

The first generation of GLONASS systems did not allow civilian application of the dual-band receiver (only L1 channel was available). Since 2009, the new generation of GLONASS allows the reception of L1 and L2 channels for civilian use, while the future series of GLONASS K satellites is supposed, during 2018, to make L5 channel for the use in aviation. It is expected that accuracy will be enhanced, along with the improved synchronisation of time oscillators in satellites and ground control centres (Bogdanov *et al.,* 2016). It will also be possible to receive distress signals from the COSPAS – SARSAT system.

3. PARTICULARITIES OF DETERMINING VESSEL'S NAVIGATION PARAMETERS

Determining radio-navigation parameters of the satellite signals for defining a vessel's course and speed relies on the applied system: the long-range systems determine the distance; the pseudo-range systems define the pseudo-distance, whereas Doppler systems measure Doppler frequencies. The range-finding systems use an active method where the reference object has to emit signals. In a pseudo-dimensional system, the distance is determined by passive measurement of the distance between the upper and lower values recorded on the time scale. As the time

scale is not reduced, the pseudo-distance systems measure the pseudo-distance, not the distance (Afanasjev *et al.,* 2009):

$$R_{pr,i} = \Delta t_{pr,i} \cdot c \tag{3}$$

where: Δt_{pr} ... the measured time period to the i-th satellite, and c ... the velocity of radio wave propagation. Constant error in distance measurement is expressed as:

$$R_c = \Delta t_o \cdot c \tag{4}$$

where: Δt_o ... the size of the time non-synchronisation.

It is possible to use three algorithms for calculating components of vector velocity and position for the observed satellite for given t_i (instant time) in MT (Moscow Time) timescale, using ephemeris data (RSS, 2016):

- precise algorithm (precise calculation for a 30-minute interval of an orbit),
- simplified algorithm (simplified calculation for a 30-minute interval of an orbit),
- long-term algorithm (precise calculation for a four-hour interval of an orbit).

Unlike ground control segment that performs the calculation of satellite's trajectories using complex models that include a high number of disturbances, user receivers apply significantly simpler models to predict the position of a satellite.

To calculate satellite's position prediction errors based on ephemeris data, numerical integration using the Runge-Kutta forth-order method is used. The method applies one minute increment for various intervals of observation for the same initial data. There are four numerical integration intervals: 5 min, 10 min, 15 min and and 4 hrs integration intervals. Depending on applied algorithms (precise or simplified) and observed interval, the prediction error of satellite positioning is varying from 0.03-0.77 m. A long-term algorithm is suitable for accurate calculation within four hours observation interval where it gives an error of 0.25-1 m. Precise and simplified algorithms for 4 hrs interval give significantly higher errors (over 30 m and 100 m).

To determine the speed of a vessel, it is necessary to measure the velocity of the mutual approach between the vessel and the satellite. This is achieved by measuring Doppler frequency that is emitted by the satellite. Since the nominal transmitter frequencies that form the upper and lower recorded values on the time scale are not reduced (Gorobtsov

et al., 2016), the system measures pseudo-Doppler frequencies instead of Doppler frequencies. The pseudo-velocity of the mutual approach is expressed as:

$$V_{ps} = \Delta f_{KDP} \lambda \tag{5}$$

where: $\lambda = c/f$ ... the wavelength, f ... the carrier wave frequency, Δf_{KDP} ... the measured pseudo-Doppler frequency.

Almanac data and t_i (MT) transmitted in navigation message can be used to compute satellite position coordinates and velocity vector parameters to predict visibility and ID of satellites and to enable targeting and receiving of the signal.

For prediction interval supported methodological errors are given in Table 2.

Table 2. Prediction errors for the SV's position and velocity (RSS, 2016)

Prediction interval	**1 day**	**2 days**	**5 days**	**15 days**	**30 days**	**2 months**	**3 months**
Maximum magnitude of position error vector [km]	2	4	7	16	25	60	120
RMS projection of position error vector on SV-to-receiver line of sight [km]	0.5	0.8	2.5	6	11	25	51
Maximum magnitude of velocity error vector [m/s]	0.5	0.8	1	2	3	8	25
RMS projection of velocity error vector on SV-to-receiver line of sight [m/s]	0. 1	0.2	0.6	1.3	2.5	5	10

Determining the position of a vessel by measuring the pseudo-distance from three or four satellites, and bringing it into the geocentric coordinate system, requires solving a system composed of four pseudo-distance equations:

$$\begin{aligned}
\sqrt{(x_{sat1} - x_c)^2 + (y_{sat1} - y_c)^2 + (z_{sat1} - z_c)^2} &= R_{pr1} + R_0, \\
\sqrt{(x_{sat2} - x_c)^2 + (y_{sat2} - y_c)^2 + (z_{sat2} - z_c)^2} &= R_{pr2} + R_0, \\
\sqrt{(x_{sat3} - x_c)^2 + (y_{sat3} - y_c)^2 + (z_{sat3} - z_c)^2} &= R_{pr3} + R_0, \\
\sqrt{(x_{sat4} - x_c)^2 + (y_{sat4} - y_c)^2 + (z_{sat4} - z_c)^2} &= R_{pr4} + R_0,
\end{aligned} \tag{6}$$

where: x_c, y_c, z_c ... unknown coordinates of the vessel, R_o ... the constant error in distance measuring,

x_{sat}, y_{sat}, z_{sat}, (i = 1, 2, 3, 4) … coordinates of the satellites obtained with the aid of the ephemeris data, R_{pri} ... the results produced by the GLONASS receiver.

The result comprises temporary coordinates x_c, y_c and z_c, as well as the correction of the value of the time non-synchronisation $\Delta t_o = R_o/c$. If more satellites are visible, then the number of equations is increased, resulting in a higher accuracy of the obtained position. In order to define a vessel's velocity it is necessary to derive this equation system (RSS, 2016):

$$\begin{aligned}
\frac{(x_{sat1}-x_c)\cdot(\dot{x}_{sat1}-\dot{x}_c)+(y_{sat1}-y_c)\cdot(\dot{y}_{sat1}-\dot{y}_c)+(z_{sat1}-z_c)\cdot(\dot{z}_{sat1}-\dot{z}_c)}{\sqrt{(x_{sat1}-x_c)^2+(y_{sat1}-y_c)^2+(z_{sat1}-z_c)^2}} &= \lambda(\Delta f_{KDP1}+\Delta f_{det}),\\
\frac{(x_{sat2}-x_c)\cdot(\dot{x}_{sat2}-\dot{x}_c)+(y_{sat2}-y_c)\cdot(\dot{y}_{sat2}-\dot{y}_c)+(z_{sat2}-z_c)\cdot(\dot{z}_{sat2}-\dot{z}_c)}{\sqrt{(x_{sat2}-x_c)^2+(y_{sat2}-y_c)^2+(z_{sat2}-z_c)^2}} &= \lambda(\Delta f_{KDP2}+\Delta f_{det}),\\
\frac{(x_{sat3}-x_c)\cdot(\dot{x}_{sat3}-\dot{x}_c)+(y_{sat3}-y_c)\cdot(\dot{y}_{sat3}-\dot{y}_c)+(z_{sat3}-z_c)\cdot(\dot{z}_{sat3}-\dot{z}_c)}{\sqrt{(x_{sat3}-x_c)^2+(y_{sat3}-y_c)^2+(z_{sat3}-z_c)^2}} &= \lambda(\Delta f_{KDP3}+\Delta f_{det}),\\
\frac{(x_{sat4}-x_c)\cdot(\dot{x}_{sat4}-\dot{x}_c)+(y_{sat4}-y_c)\cdot(\dot{y}_{sat4}-\dot{y}_c)+(z_{sat4}-z_c)\cdot(\dot{z}_{sat4}-\dot{z}_c)}{\sqrt{(x_{sat4}-x_c)^2+(y_{sat4}-y_c)^2+(z_{sat4}-z_c)^2}} &= \lambda(\Delta f_{KDP4}+\Delta f_{det}),
\end{aligned} \tag{7}$$

where: x, y, z … the unknown values that include the rate of change in the vessel's coordinates, Δf_{det} ... the value of the transmitter frequency non-conformity.

Through solving the above system, actual vessel velocity is determined by taking into account all three coordinates and values of the transmitter frequency non-conformity. Given the fact that a real-life vessel moves only with reference to the planes x and y: it is assumed that the value of z equals to 0.

Regarding the x, y plane (V_{pl}), the vessel's velocity is defined by the expression:

$$V_{pl} = \sqrt{x_c^2 + y_c^2} \tag{8}$$

marking $\dot{x} = V_x$, $\dot{y} = V_y$, leads to

$$V_{pl} = \sqrt{{V_x}^2 + {V_y}^2} \tag{9}$$

Establishing a vessel's course is performed with regard to the vessel's velocity concerning the coordinates x and y, according to the following relation (Afanasjev *et al.,* 2009):

$$\Theta = arctg\frac{V_x}{V_y} \tag{10}$$

Assuming the same mean square error (MSE) through the measurement of velocity along the coordinates x and y,$\sigma(Vx) = \sigma(Vy) = \sigma_{MSE}$, an accidental error in the course Θ in reference with errors ΔV_x, ΔV_y can be defined as the result of deriving the expression (10), from which it follows

$$\Delta\Theta = \frac{\Delta V_x V_y - \Delta V_y V_x}{V_y^2\left(1+\frac{V_x^2}{V_y^2}\right)} = \frac{\Delta V_x V_y - \Delta V_y V_x}{V_{pl}^2} \tag{11}$$

Accidental errors ΔV_x and ΔV_y are independent so error variations are the same:

$$\Delta\bar{\bar{V}}_x^2 = \Delta\bar{\bar{V}}_y^2 = \sigma_{SKP}^2 \tag{12}$$

then

$$\overline{\Delta\Theta^2} = \frac{\Delta\bar{V}_x^2\, V_y^2 + \Delta\bar{V}_y^2\, V_x^2}{V_{pl}^2} = \frac{\sigma_{SKP}^2}{V_{pl}^2} \quad [\mathrm{rad}^2] \tag{13}$$

and the measured MSE is inversely proportional to the vessel's velocity.

4. PARTICULARITIES OF DETERMINING THE IMPACT OF THE IONOSPHERIC ERROR BY GLONASS DUAL-BAND RECEIVERS

Two factors are affecting the error in determining the parameters of navigation: the horizontal dilution of precision (HDOP coefficient) and the MSE, measurements of the satellite pseudo-distance and pseudo-velocity. The MSE value is affected by four pseudo-constant errors (ephemeris accuracy error, mutual satellite synchronisation error, tropospheric and ionospheric errors), and by two random errors – multipath error and noise error (Hofmann, Lichtenegger and Wasle, 2007). When using a dual-band receiver, the value of the ionospheric error ΔR_{ion} is inversely proportional to the square of the signal of the carrier wave frequency (Gorobtsov *et al.,* 2016):

$$\Delta R_{ion} = \frac{A}{f^2} \tag{14}$$

where: A... the constant coefficient whose value remains unchanged during a 15-minute interval. The dual-band receiver performs two measurements of the pseudo-distance:

$$\begin{cases} \Delta R_o = \Delta R_{chg1} + \frac{A}{f_1^2}, \\ \Delta R_o = \Delta R_{chg2} + \frac{A}{f_2^2}, \end{cases} \tag{15}$$

where: ΔR_o ... the pseudo-distance not affected by the ionospheric error, ΔR_{chg1}, ΔR_{chg2} ... the pseudo-distance measurement results at frequencies f_1 and f_2, respectively, considering the ionospheric error. Solving of the equation system results in:

$$\Delta R_o = \frac{\Delta \mathrm{R}chg1 \cdot f_1^2 - \Delta \mathrm{R}chg2 \cdot f_2^2}{f_1^2 - f_2^2} \tag{16}$$

$$= \Delta R_{chg1} \frac{1}{1-m^2} - \Delta R_{chg2} \frac{m^2}{1-m^2} \tag{17}$$

$$= 2.53 R_{chg1} - 1.53 R_{chg2} \tag{18}$$

As the dual-band GLONASS system uses frequencies f_1 =1602 MHz, f_2 =1246 MHz, then $m = f_2 / f_1$ = 7/9. Unlike GPS systems, where it is assumed that the ionospheric error contributes to the overall signal propagation errors with up to 50 % (Anđelini, Lučić and Filjar, 2016), in single-band GLONASS receivers this error is up to 7 metres, whereas in dual-band receivers the error is reduced to 7 cm, and the total MSE to 5 m (Gorobtsov *et al.,* 2016). Hereby the standard position deviation (σ_{PSN}) for dual-band receivers at $HDOP$ = 2 is determined by the expression:

$$\sigma_{PSN} = \sigma_{SKP} HDOP = 10 \text{ m} \tag{19}$$

By joint measurement of Doppler frequencies at the output of both receiver bands and by solving the system comprising two equations, the pseudo-constant ionospheric error in pseudo-distance measurement is removed, i.e.

$$\begin{cases} \Delta V_0 = \Delta V_{\mathrm{chg1}} + \frac{B}{f_1}, \\ \Delta V_0 = \Delta V_{\mathrm{chg2}} + \frac{B}{f_2}, \end{cases} \tag{20}$$

where: ΔV_0 ... the pseudo-velocity not affected by the ionospheric error, ΔV_{chg1}, ΔV_{chg2} ... the measured pseudo-velocity at frequencies f_1 and f_2, B ... the constant coefficient.

The system solving results in:

$$\Delta V_0 = \Delta V_{chg1} \frac{1}{1-m} - \Delta V_{chg2} \frac{m}{1-m} \tag{21}$$

as m – 7/9,

$$\Delta V_o = 4.5 \Delta V_{chg1} - 3.5 \Delta V_{cgh2} \tag{22}$$

Using the dual-band receiver, the pseudo-velocity error determined in this way reduces the error caused by the ionosphere from $4 \cdot 10^{-2}$ to $0.04 \cdot 10^{-2}$ [m/s] (Gorobtsov *et al.,* 2016).

5. ADEQUACY OF USING DUAL-BAND GLONASS RECEIVERS IN OCEAN NAVIGATION

Single-band satellite receivers that are widely available at the market and installed on board merchant vessels provide the maximum accuracy of 15 meters in most favourable sailing conditions. In practice, however, the accuracy can be considerably degraded, depending on the sailing area and the state of the atmosphere. For this reason, vessels are typically equipped with Differential Global Positioning System (DGPS) which, supported by land-based transmitters, enhances the accuracy of the GPS position. In this way, the accuracy can be measured in centimetres, depending on the atmospheric conditions and the distance between the user and the DGPS base station. Considering maritime navigation requirements, the obtained DGPS accuracy is up to 3 metres (Lapucha and Kurtis, 1992, Kuter and Kuter, 2010). Unlike GPS service, the reception of DGSP signals is not free of charge, and the annual costs per vessel may amount to thousands USD (JA, 2018).

Since the dual-band GLONASS receivers enable the accuracy of the 2D position within the range of 10 m (19), it is obvious that their potential onboard application, instead of DGPS, is entirely justified. As part of the GNSS system, these receivers are fully compatible with the existing navigation equipment on the bridge (ECDIS, gyro-compass, ARPA radar, etc.). Although the initial cost of the dual-band receivers is higher compared to single-band GNSS receivers, the application of the dual-band receivers would eliminate the costs of the DGPS service, which would enable shippers to make considerable savings in the long run.

6. CONCLUSION

The dual-band GLONASS receiver applies the specific approach in calculating and eliminating the effects of the ionosphere on the accuracy of position determination. The approach is based on the simultaneous processing and comparison of the values received by two independent frequencies. Compared to the results obtained by single-band receivers, the introduction of the dual-band version considerably reduces the impact of ionospheric error to an absolute value of 0.1 meters. The performance features of the existing dual-band receivers have practically eliminated the effects of the ionosphere on the accuracy of position, thereby enabling the users to achieve the satisfactory position accuracy. The application of these receivers on board vessels is entirely justified as it is no longer necessary to bear additional expenses and costs of the DGPS service.

ACKNOWLEDGEMENTS. Research activities presented in this paper were conducted under the research project *Research into the correlation of maritime-transport elements in marine traffic: Satellite navigation segment*, supported by the University of Rijeka, Croatia.

References

Afanasjev, V. V., Marinich, A. N., Pripotnyuk, A. V. and Ustinov, U. M. (2009). *Ship radar systems*. Saint Petersburg: Velenara. (in Russian).

Anđelini, M., Lučić, A. and Filjar, R. (2016). Satellite positioning error model for location – based services. In: Kos, S., Filjar, R. and Brčić, D. (eds.) *Proceedings of the 10th Annual Baška GNSS Conference*. Baška, Croatia. pp. 105–110.

Bogdanov, P., Druzhin, A., Primakina, T. and Feoktistov, A. (2016). Approaches to GLONASS time accuracy improvement. In: Kos, S., Filjar, R. and Brčić, D. (eds.) *Proceedings of the 10th Annual Baška GNSS* Conference. Baška, Croatia. pp. 111–116.

Gorobtsov, A. P., Marinich, A. N., Pripotnyuk, A. V. and Ustinov, U. M. (2016). *Technical means of navigation*, volume 3. Ship electronic navigation devices. Edited by Ustinov, U. M. Saint Petersburg: Morsar. (in Russian).

Hofmann, W.B., Lichtenegger, H. and Wasle, E. (2007). *GNSS – Global Navigation Satellite Systems GPS, GLONASS, Galileo, and more*. Wien: Springer-Verlag.

Information Analytical Center (ИАЦ/IAC). (2018). Available at: https://glonass-iac.ru/, accessed 10 April 2018.

Johnny Appleseed GPS (JA). (2018). *DGPS – CORS Subscriptions.* Available at: https://www.ja-gps.com.au/DGPS/CORS-Subscriptions, accessed 12 July 2018.

Kuter, N. and Kuter, S. (2010). Accuracy comparison between GPS and DGPS: A field study at METU campus. *European Journal of Remote Sensing*. 42(3). pp. 3–14.

Langley, B. (2007). *GLONASS Overview*. Geodetic Research Laboratory University of New Brunswick, Fredericton.

Lapucha, D. and Kurtis L. M. (1992). *Investigation of the Real-Time Accuracy of the DGPS Method.* LA: John E. Chance and Associates.

Russian Space Systems, JSC (RSS). (2016). *General Description of Code Division Multiple Access Signal System Edition 1.0*. Moscow: RSS.

Sveučilište u Rijeci
POMORSKI FAKULTET
FACULTY OF MARITIME STUDIES
University of Rijeka

University of Zagreb
Faculty of Transport
and Traffic Sciences

Royal Institute of Navigation
Science Technology Practice

12th
Annual
Baška GNSS
Conference

OPTIMAL BEACON POSITIONING FOR INDOOR DRONE NAVIGATION

Franko Hržić, Diego Sušanj, Kristijan Lenac

University of Rijeka, Faculty of Engineering, Rijeka, Croatia

e-mail: fhrzic@riteh.hr (Corresponding author)

Abstract

In this manuscript an approach for determining optimal positions of Bluetooth Low Energy (BLE) beacons for maximizing coverage is presented. Beacons emit a unique signal which is detectable in the part of the environment. The proposed method, based on Gradient descent with Nesterov momentum, minimizes the cost function in order to find the optimal positions of beacons in a virtual environment. The cost function, or in case of this manuscript the loss function, describes coverage of the environment by the beacons.

Key words: *Gradient descent, Bluetooth Low Energy, Indoor positioning*

1. INTRODUCTION

With rising interest in drone usage, especially in drone racing and industry drones, information about indoor drone position becomes indispensable. Basic method to determine a position involves use of the Global Navigation Satellite System (GNSS), but this is usually unavailable indoors as the GNSS receivers on the drones are out of range of satellite signals.

In this manuscript the primary focus is put on the sensor placement problem, where the goal is to find the optimal position and, depending on the sensor type, orientation of the sensors in the target environment. Optimal sensor placement is an important issue as it, based on overall coverage of the environment, directly affects drone performance.

There are multiple types of coverage measures, usually defined by usage, as the sensors are placed with specific use in mind (Cardei and Wu, 2006, Meguerdichian *et al.*, 2001). Used coverage measures are: area coverage, point coverage, barrier coverage, *k*-coverage and least exposure coverage. Most widely used measure is the area coverage which is defined as the ratio of the area covered by the sensors to the total target area. As special cases of area coverage there are point and barrier coverages, where some special locations in the target environment have higher importance in the coverage problem. The objective of the *k*-coverage is to cover each location in the target environment by at least *k* sensors. There are multiple reasons to use *k*-coverage, for example, robustness and positioning. Least exposure coverage has an objective to find a path within the environment with low observability. The focus of this manuscript is on the area coverage but with specific application in mind.

The common assumption is related to the detection ability and coverage area of the sensor (Huang and Tseng, 2005). Detection is usually modelled using binary coverage for each sensor (Hefeeda and Ahmadi, 2009), but probabilistic coverage provides a more refined model (Akbarzadeh *et al.*, 2011, Akbarzadeh *et al.*, 2012). Coverage area of the sensor depends on the sensor type. The assumption of omnidirectional sensing ability is only true for some types of sensors (Bluetooth beacons, Wireless beacons…), while others have directional sensing ability (cameras, ultrasonic sensors…). In this manuscript omnidirectional sensing ability with probabilistic coverage model is used but the algorithm allows also other types of sensors to be added to create a heterogeneous sensor network.

The final assumption concerns the dimensionality of the target environment. Two-dimensional problem is easier to calculate (Dhillon and Chakrabarty, 2003) but could lead to an overestimation of the coverage in real environment. Three-dimensional problem is more realistic and leads to much better results, but with an inherent problem of the higher computing price. In any case, the calculated covered area of each sensor should take into consideration both the topography of the environment and existing obstacles which occlude the sensing area of each sensor (Akbarzadeh *et al.*, 2010).

In this manuscript, a sensor placement optimization method based on gradient descent is proposed and described. As already mentioned, probabilistic sensing model with existing topography of the environment and sensor specific behaviour are used. The manuscript is organized as follows: first BLE beacons and the corresponding sensor model are described. After that, the gradient descent algorithm and the used cost function are described with connection to the sensor model. Finally, the results are shown and conclusions are drawn.

2. SENSOR MODEL

2.1 *Bluetooth low energy beacons*. Bluetooth low energy beacons are signal transmitters devices. They emit identifier signals into the nearby space that other electronic devices can receive. As they are emitting unique signals for each sensor they are frequently used for indoor localisation and fingerprinting. Among many manufactures of BLE beacons, in this research Estimote BLE beacon devices were used (Faragher and Harle, 2010).

Estimote BLE beacon is a battery powered device which allows more flexible placement into the environment since it doesn't need constant power supply. It emits 2.4 GHz radio wave signal at intervals of 200 milliseconds into the space using an omnidirectional antenna. The Received signal strength at one-meter distance from Estimote beacon is -75 decibels. Received signal strength indicator (RSSI) is used in visibility calculation for each voxel in the environment. This formula, eq. 2, is a key element of coverage calculus and later in the Cost function calculation.

2.2 *Voxel visibility.* In the proposed case sensors with omnidirectional antennas were simulated but with the assumption of perfect single point and equal dissipation rate. With this assumption in mind, sensor orientation is not important for the voxel visibility and can be removed from the calculation. Non-convex topographies and

obstacles in the environment create occlusions in the environment. Therefore, the first step in a visibility calculation for each voxel is to determine if there is a line of sight between the sensor and the targeted voxel. Distance between the sensor (s_j) and the voxel (v_i) is then used to determine the voxel visibility. As shown in eq. 1, the distance depends on x, y, and z coordinates of both sensor and target voxel:

$$d_{vs}(v_i, s_j) = \sqrt{(v_{ix} - s_{jx})^2 + (v_{iy} - s_{jy})^2 + (v_{iz} - s_{jz})^2} \tag{1}$$

Voxel visibility is defined using strength of the received signal (RSSI) at the target voxel distance. RSSI is calculated from the distance information and information about base signal strength or RSSI at distance of one meter. RSSI is calculated using the standard formula, eq. 2, using previously calculated distance, eq. 1, between each sensor and voxel. RSSI at one meter, as a base parameter, for the emulated Estimote BLE sensor is –75 dB.

$$rssi(v_i, s_j) = -20 \cdot log_{10}\left(d_{vs}(v_i, s_j)\right) + rssi_{1m} \tag{2}$$

The dependence between signal strength and distance is shown in Figure 1.

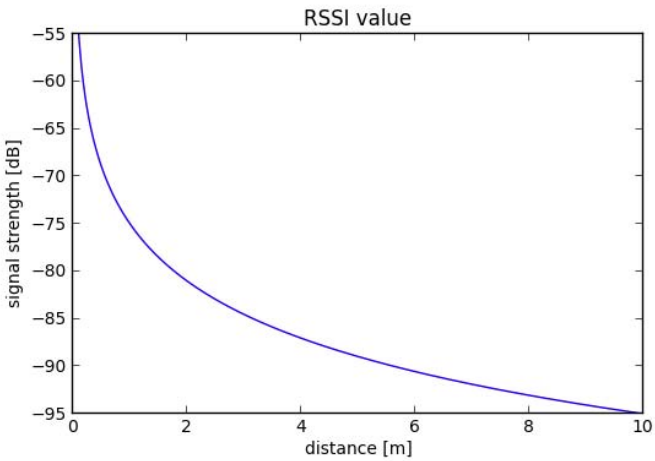

Figure 1. Signal strength depending on the distance between sensor and target voxel

If the distance between sensor and target voxel exceeds certain amount and the signal strength falls below a noise level, that information becomes unusable and

cannot be used to determine distance. The defined noise level for normal usage is –85 dB. Signal to noise ratio (SNR), or the difference between signal strength and noise level, shown in eq. 3 is used in further calculations.

$$snr(v_i, s_j) = \begin{cases} rssi(v_i, s_j) - noise & \text{iff } rssi(v_i, s_j) > noise \\ 0 & \text{iff } rssi(v_i, s_j) \leq noise \end{cases} \tag{3}$$

In case that a signal is equal or lower than noise level, the result becomes zero, which in this case means that the voxel is not visible from the sensor. Dependence between SNR and the distance is shown in Figure 2.

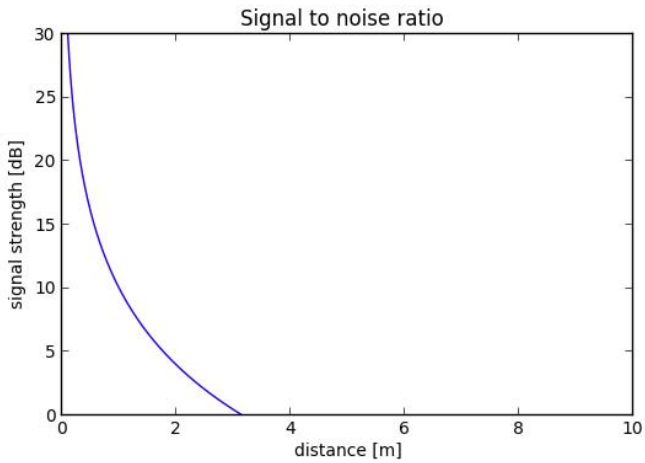

Figure 2. Signal to noise ratio depending on the distance between sensor and target voxel

To have usable information in further calculations, results from the SNR calculation were scaled between zero and one by dividing the resulting SNR value with SNR to the voxel closest to the sensor. Maximum SNR, or in case of this manuscript a visibility, is calculated using maximum RSSI, eq. 3. Maximum RSSI, eq. 2, is calculated using minimal distance that depends on the spatial resolution of the voxels which describes the environment. Visibility formula is shown in eq. 4, and values of visibility depending on the distance are shown on Figure 3.

$$v_{vs}(v_i, s_j) = \frac{snr(v_i, s_j)}{rssi_{max} - noise} \tag{4}$$

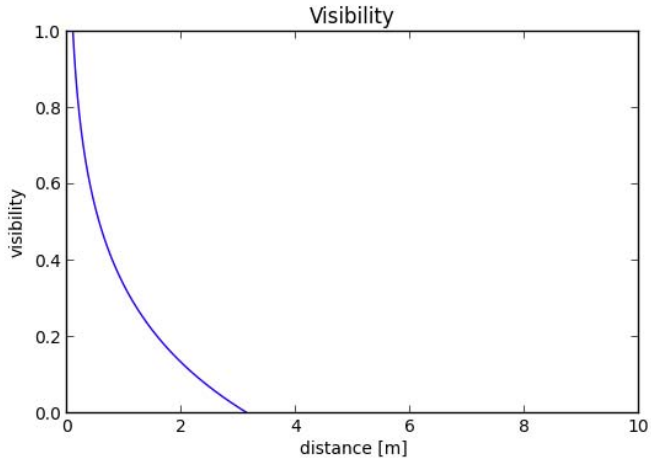

Figure 3. Visibility for the voxels depending on the distance from the sensor

3. PROPOSED METHOD

In this manuscript Gradient descent algorithm is proposed for optimal beacon positioning. A gradient descent algorithm is a first order iterative optimization algorithm for finding the minimum of a function. To find the minimum of a function, the algorithm takes steps in the direction of the minimizing gradient (Goodfellow *et al.*, 2016).

Gradient descent requires a cost function, or in the case of this manuscript a loss function that measures the goodness of beacons positions. The proposed loss function calculates the coverage of each voxel using the visibility from each beacon. There are two main constraints that must be taken into account. The first one is the number of beacons and their initial positions. The second one is the spatial resolution of the voxels describing the space. Both constraints are treated as hyperparameters and are set based on previous experience. Since the number of voxels can be measured in thousands, the basic gradient descent algorithm is slow. To solve this problem, a Gradient descent with Nesterov momentum was used. Gradient descent with Nesterov momentum requires several parameters:

1. Learning rate: ε,

2. Momentum parameter: α,

3. Initial parameter: θ, which represent the initial positions of vectors,

4. Initial velocity: ϑ.

Learning rate ε limits the algorithm from taking big steps in any direction when updating gradient because it might overleap the best solution. Same is with the momentum parameter α, it creates the effect that the calculated momentum updates the gradient from the previous iteration step instead of replacing it completely. Initial parameter ϑ represents the positions of the sensors in the room and it is chosen empirically or placed randomly. The initial velocity ϑ is set to zero. Also, worth mentioning is that the Gradient descent with Nesterov momentum calculates the gradient at the approximated new position. This is in contrast to the ordinary method which calculates the gradient in current position. The method follows the intuition of velocity – the position of the sensor in the next step is already known based on the current position and velocity.

Gradient descent with Nesterov momentum pseudocode is as follows:

While stopping criterion not met **do**:

Apply interim update: $\theta' \leftarrow \theta + \alpha\vartheta$

Compute gradient: $g \leftarrow \Sigma_i L(f(x(i); \theta'), y(i))$

Compute velocity update: $\vartheta \leftarrow \alpha\vartheta - \varepsilon g$

Apply update: $\theta \leftarrow \theta + \alpha\vartheta$

The goal of the gradient descent algorithm is finding the minimum of a function. In this manuscript the loss function is introduced. Loss value for each sensor – voxel pair is defined in eq. 5, as a complementary value of the visibility, defined in eq. 4:

$$l_{vs}(v_i, s_j) = 1 - v_{vs}(v_i, s_j). \tag{5}$$

As one voxel can be "seen" from multiple sensors in the environment, a loss for each voxel is defined as a product of the loss values from each of the m sensors in the sensor set S, eq. 6:

$$L_v(v_i, S) = \prod_{j=1}^{m} l_{vs}(v_i, s_j) \tag{6}$$

This results in lower loss value if that voxel can be "seen" from multiple sensors.

A global loss value, eq. 7, is defined as the arithmetic mean of loss values of all n voxels in the environment V:

$$L(V,S) = \frac{1}{n}\sum_{i=1}^{n} L_v(v_i, S). \tag{7}$$

4. RESULTS AND CONCLUSION

To evaluate the proposed method a set of tests were defined. Tests differ in the topography of the environment and obstacles, number of beacons and spatial resolution of the voxels which describe the environment.

The presented evaluation was done on the artificial "L" shaped environment with two beacons and low voxel spatial resolution. Each beacon was set to the opposite corner of the environment as it can be seen in Figure 4a). For these two beacons the calculated value of the loss function was 0.90913. After running the proposed method until convergence, the beacons were repositioned to a new position, as shown in Figure 4b). The loss function value at the new position was 0.74737.

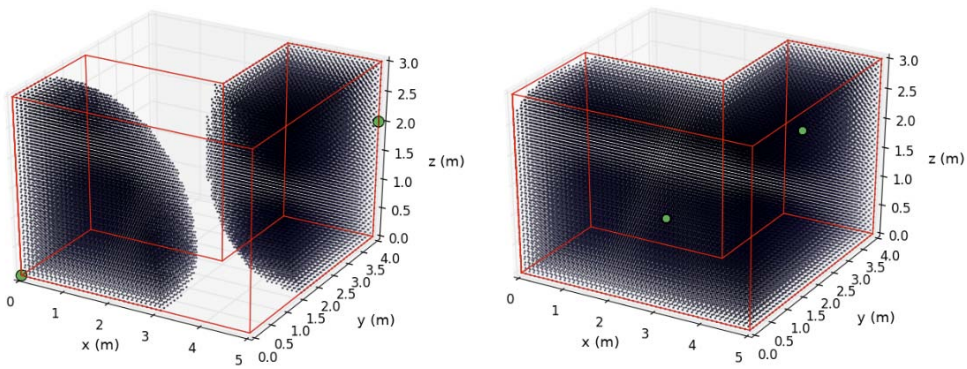

a) **b)**

Figure 4. Sensor positions and visible voxels in the environment:
a) before the simulation; b) after the simulation

To conclude, the proposed method successfully positioned the beacons while minimizing the defined cost function using the Gradient descent with Nesterov momentum algorithm. The performed simulation shows that the proposed method successfully positioned the beacons in a simulated three-dimensional space. Good

positioning of beacons is important for reliable indoor drone navigation. Since the proposed method is based on the received signal strength, it can be easily adjusted to other devices and similar problems.

References

Cardei, M. and Wu, J. (2006). Energy-efficient coverage problems in wireless ad-hoc sensor networks. *Comput. Commun.* 29. pp. 413–420.

Meguerdichian, S., Koushanfar, F., Potkonjak, M. and Srivastava, M. (2001) Coverage problems in wireless ad-hoc sensor networks. In *Proceedings of the Twentieth Annual Joint Conference of the IEEE Computer and Communications Societies* (*INFOCOM 2001*). 3. pp. 1380–1387.

Huang, C. and Tseng, Y. (2005). The coverage problem in a wireless sensor network. *Mob. Netw. Appl.* 10. pp. 519–528.

Hefeeda, M. and Ahmadi, H. (2009). Energy Efficient Protocol for Deterministic and Probabilistic Coverage in Sensor Networks. *IEEE Trans. Parallel Distrib. Syst.* 99. pp. 579–593.

Akbarzadeh, V., Gagné, C., Parizeau, M. and Mostafavi, M. (2011). Black-box optimization of sensor placement with elevation maps and probabilistic sensing models. In *Proceedings of the International Symposium on Robotic and Sensors Environments* (*ROSE*). pp. 89–94.

Akbarzadeh, V., Gagné, C., Parizeau, M., Mostafavi, M. and Argany, M. (2012). Probabilistic Sensing Model for Sensor Placement Optimization based on Line-of-sight Coverage. *IEEE Trans. Instrum. Meas.* 62. pp. 293–303.

Dhillon, S. and Chakrabarty, K. (2003). Sensor placement for effective coverage and surveillance in distributed sensor networks. In *Proceedings of the IEEE, Wireless Communications and Networking Conference* (*WCNC*). 3. pp. 1609–1614.

Akbarzadeh, V., Ko, A., Gagné, C. and Parizeau, M. (2010). Topography-Aware Sensor Deployment Optimization with CMA-ES. In *Proceedings of the International Conference on Parallel Problem Solving from Nature* (*PPSN*). 6239. pp. 141–150.

Faragher, R. and Harle, R. (2015). Location Fingerprinting With Bluetooth Low Energy Beacons. *IEEE journal on selected areas in communications*. 33(11). pp. 2418–2427.

Goodfellow, I., Bengio, Y. and Courville, A. (2016). *Deep Learning*. Cambridge: The MIT Press.

Sveučilište u Rijeci
POMORSKI FAKULTET
FACULTY OF MARITIME STUDIES
University of Rijeka

University of Zagreb
Faculty of Transport
and Traffic Sciences

Royal Institute of Navigation
Science Technology Practice

12th
Annual
Baška GNSS
Conference

COMPARISON OF HEADING INFORMATION OBTAINED WITH MODERN GPS-BASED NAUTICAL INSTRUMENTS

Takashi Kubota[1], **Nobuyoshi Kouguchi**[2], **Yoshihiro Kurihara**[3]

[1] National Institute of Technology, Oshima College, 1091-1 Oaza-Komatsu, Suo-Oshima, Oshima, Yamaguchi, Japan
e-mail: kubota@oshima-k.ac.jp (Corresponding author)

[2] Kobe University, Faculty and Graduate School of Maritime Sciences, Japan

[3] Nippon Kaiji Kentei Kyokai, Japan

Abstract

There has been a proliferation in the diversity of navigational instruments available to maritime shipping vessels with the recent advances in telecommunications technology. Navigators must now prioritise information obtained from various instruments. The danger of confusion is particularly acute when several navigational instruments provide overlapping information. To assess the reliability of modern instrumentation, this study compares a large volume of heading data obtained with two instruments that use global positioning system (GPS) data, the well-established GPS compass and the more-advanced GPS speed log. The information from these instruments is compared with data from a gyrocompass, which is traditional and can be presumed to be reliable.

Keywords: *GPS compass, GPS speed log*

1. INTRODUCTION

Marine accidents are common among the domestic vessels sailing along the Japanese coast, with the most-recent data including reports of 2137 cases in 2015 (JCG, 2015). Human error is a factor in 90 % of marine accidents. Human error can occur with incorrect judgements derived from navigational instruments. Although modern instruments were developed to reduce the potential for human error, modern navigators must make decisions based on overlapping information from instruments that may have varying levels of error. Modern instruments should be compared among themselves and with traditional equipment to understand how reliable the instruments are relative to each other.

This article reports tests to compare navigational information acquired using the now-common global positioning system (GPS) compass and a GPS speed log, a more-advanced instrument. GPS devices are very useful, but they have different levels of accuracy, and redundant information may confuse navigators.

The overlapping information provided by GPS compasses and speed logs include the heading, pitch angle and roll angle; this study focuses on the heading data. The information recorded from the GPS devices is compared with that from the ship's built-in gyrocompass, which is reliable. Data from an expedition are compared to characterise the instruments and rate their reliability.

Figure 1. Experimental ship Kodamukimaru

2. EXPERIMENTAL METHOD

Experiments to test the information provided by different navigational systems were performed from 10 September to 25 October 2016 as the test vessel navigated from Naruohama to Oki. The vessel, experimental instruments and marine environment are described below.

2.1 *Experimental ship.* Figure 1 shows the ship used for the field tests, and Table 1 lists its specifications. This experimental ship Kodanukimaru is used for multipurpose work and it has the full complement of modern navigational instruments due to the need for high-accuracy positioning during research operations.

Table 1. Specifications of the experimental ship

LOA (length overall)	89.9 m
Breadth	27.0 m
Gross tonnage	4831 ton
Navigation full speed	12.0 knots
Draft full/ballast	3.95 m/2.76 m
Propulsion device	CPP 1471 kW, 2 axles
Main thruster	Controllable-hoisting type, two sets
Auxiliary thruster	Tunnel type, one set

2.2 *Instruments.* The experiment tested two GPS-based instruments. The first instrument was the GPS speed log. GPS speed logs are the latest navigational instruments that use GPS. They enclose two antennae in a dome and provide many types of information besides speed. Table 2 lists the types of navigational information that can be measured with a GPS speed log.

Table 2. Navigational information measurable by a GPS speed log (ODR, 2018)

GPS message		Measurable navigational information
$GPGGA		Latitude, longitude, Height of antenna, Horizontal dilution of precision etc.
$PFEC	GPatt	Heading, pitch angle, roll angle
$PFEC	GPhve	Heave height
$VDROT		Rate of turn etc.
$VDVBW		Speed over the ground, Longitudinal Water Speed, Transverse Water Speed etc.

Figure 2 shows the location of the GPS speed log on board. One GPS antenna is fixed on the deck behind the bridge. A long cable is used to supply electrical power to the antenna from the bridge. The navigational data logs are recorded via a USB port beneath the display of the GPS speed log. The sampling rate of the speed log we tested was 100 ms.

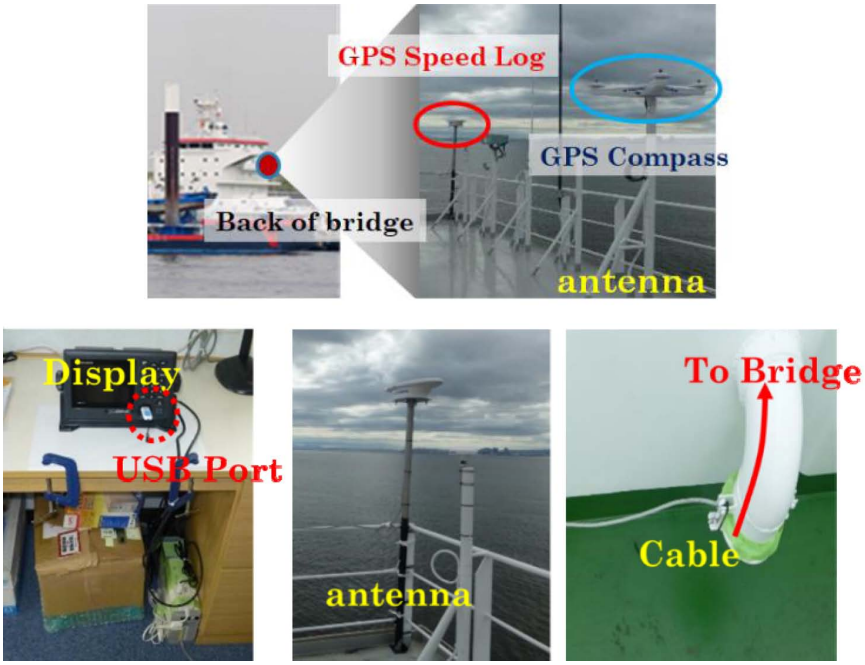

Figure 2. Setting of the GPS speed log

The second instrument was a newly installed GPS compass. This instrument is also able to independently measure the course over the ground, speed over the ground, latitude, longitude and basic three-dimensional movements such as roll, pitch angle (Hashimoto *et al.*, 2012) and height angle. The sampling rate is also every 100 ms. The GPS compass has three antennae because it is designed to measure changes in the ship's direction with high precision. The present study sought to determine whether this difference in number of antennae significantly affects the accuracy of the data output. Figure 3 shows the layout of the instruments on the deck of the ship. The gyrocompass and GPS compass were installed on the bridge. The GPS antenna is placed behind the bridge. The distance of cable connecting the antennae to the receivers of the GPS instruments were about 30 m.

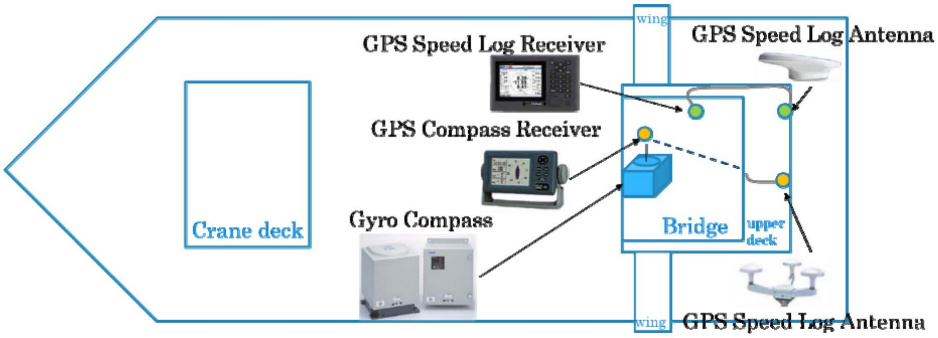

Figure 3. Ground plan with instruments

2.3 *Experimental area.* Figure 4 shows the route that the test voyage followed. The experimental vessel departed from the port of Naruohama in Hyogo Prefecture for Oki Island on 10 September, intending to set artificial fishing bank. The ship arrived at the port of Saigo on Oki Island on 12 September. After carrying out research and preparing for work, the ship departed from Saigo for an area to the north of Oki Island, and work began on 25 September. After the work was completed, the ship returned to Saigo and then left for the port of Naruohama on 26 September.

Figure 4. Area navigated during the experiment

3. ANALYSES

***3.1** Comparative instruments.* Heading data was used to compare the gyrocompass and speed log in the same terms. According to (IMO, 2000), a gyrocompass should be installed in all ships of gross tonnage more than 500 tonnes. The rule also specifies that a Transmitting Heading Device (THD) that provides true heading information also be installed in ships of this size. In the IMO rule, three methods of heading detection are included: a magnetic compass, gyrocompass, or the radio waves from a global navigation satellite system (GNSS).

Navigators usually have absolute faith in their gyrocompass, as it has been used as the most reliable instrument to indicate the heading for over 100 years. The reliability of gyrocompass is generally very high. According to navigational report of Tokyo University of Marine Science and Technology, the average of dynamic error by gyrocompass was 0.08° for the true heading (OACIS, 2006).

Table 3 lists each instrument performance indicator and the IMO standards for THDs. In Table 3, the performance of all instruments is nearly the same and each instrument satisfies the IMO requirements. Therefore, gyro compass is used to assess the reliability of the heading derived from the GPS devices.

Table 3. List of instruments' performance

	THD (Standards of IMO)	**Gyro compass**	**GPS compass**	**GPS speed log**
Static error	±1.0°	±0.3°	±0.5°	±0.5°
Dynamic error	±1.5°	±0.5°	±0.5°	±0.5°
Follow-up speed	-	75°/s	45°/s	45°/s
resolution performance	-	0.1° analog display	0.1° digital display	0.1° digital display
Others	Transfer error ±0.2	No interface, only inner circuit for Repeater compass, Auto pilot system and etc.	IEC61162 IN×2,OUT×3, Ethernet, USB (maintenance only)	IEC61162 IN×3,OUT×3, Ethernet, USB (maintenance only)

***3.2** Period of analysis.* Figure 5 shows Navigation diagram and Table 4 lists a timeline of relevant data from the test voyage. The navigation covered in Table 4 occurred over the course of about 2 weeks; therefore, a large quantity of data was obtained. Five phases of navigation were selected for analysis: In-berth, ordinary navigation, narrow channel navigation, port-entering and working.

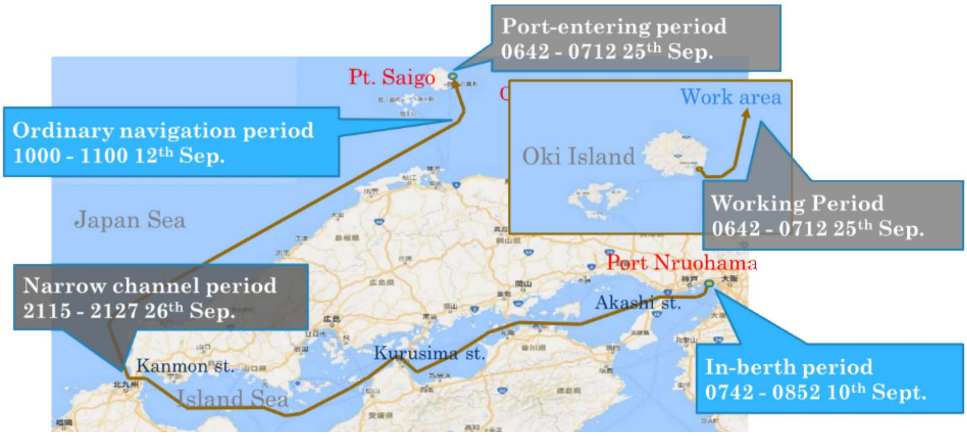

Figure 5. Navigation diagram

Table 4. Timeline of navigation with circumstance

Date	Time (JST)	Timeline of Voyage	Vessel state		Sea state		
			Course (°)	Speed (knots)	Wind Direction	Wind speed (m/s)	Height of wave (m)
10 Sep	09:00	Departed from Port Naruohama	020	var	NE	2	-
	11:00	Entered Akashi strait	300	10.4	South	1	0
	21:03	Entered Kurushima strait	Variously	10.3	South	3	0
11 Sep	12:00	Entered Kanmon straight	Variously	7.3	SE	2	0.5
12 Sep	11:20	Arrived at Port Saigo	Variously	2.0	NE	5	-
24 Sep	21:00	Departed from Port Saigo	175	6.5	NW	4	-

Date	Time (JST)	Timeline of Voyage	Vessel state		Sea state		
			Course (°)	Speed (knots)	Wind Direction	Wind speed (m/s)	Height of wave (m)
25 Sep	06:40	Started Working	112	0	East	1	0.4
	10:15	Finished Working	343	0	East	1	0.3
	17:35	Arrived at Port Saigo	192	9.4	North	2	-
26 Sep	08:15	Departed from Port Saigo	Variously	Variously	North	1	-
27 Sep	20:00	Entered Kanmon straight	Variously	5.5	NW	3	0
	17:00	Entered Kurushima strait	Variously	10.3	South	3	0
28 Sep	04:00	Entered Akashi strait	064	6.5	East	4	0
	09:00	Arrived at Port Naruohama	020	Variously	NE	2	-

In-berth period: The period selected was while the ship was berthing at the port of Naruohama from 07:42 to 08:52 on 10 September.

Ordinary navigation period: The ship was navigating near the Shimane offing, with steady speed and course and calm seas, from 10:00 to 11:00 on 26 September.

Narrow channel navigation period: When the ship was passing through the Kanmon Straights from 21:15 to 21:27 on 26 September. At that time, she changed course by more than five knots against a tidal stream, under domestic regulation (JCG, 2016).

Port-entering period: When the ship was entering the port of Saigo, there were frequent speed changes. This occurred from 17:50 to 17:57 on 25 September.

Working period: The crew were setting fish bed blocks 60 km off north Oki Island 60 km, from 06:42 to 07:12 on 25 September.

Conditions were calm at all times during the experiments; therefore, navigation was not affected by adverse weather.

4. RESULTS

***4.1** In-berth period.* Figure 6 shows the ship's heading as given by each navigational instrument during the in-berth period. In Figures 8 to 12, the ship's course is on the vertical axis, and time elapsed in seconds is on the horizontal axis.

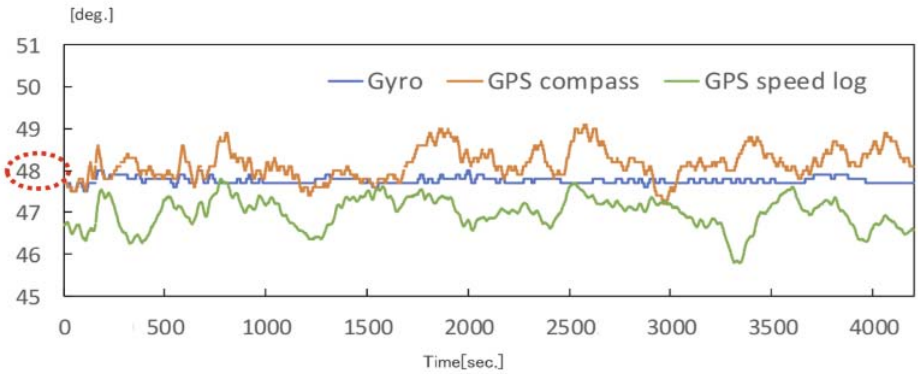

Figure 6. Heading during the in-berth period

Figure 6 shows that the gyrocompass indicated an almost fixed course of 048° as the ship was in berth. Table 5 lists the different readings from each instrument. Each of the average headings was within about 1°. The standard deviation of the gyrocompass was 0.07°, much smaller than the GPS heading. The standard deviations of the GPS instruments were about 0.4°, also adequately small. To compare the difference of each instrument's readings from the gyrocompass heading, the difference of the GPS compass was 0.9° and of the GPS speed log was 1.9°.

Table 5. Difference of each instrument

Difference	**Gyro compass**	**GPS compass**	**GPS speed log**
Average heading (°)	47.8	48.2	47.0
Standard deviation	0.07	0.37	0.38
Maximum difference from gyro heading (°)	-	0.9	1.9
Sample size	4200		

***4.2** Ordinary navigation.* Figure 7 shows the heading data given by the different instruments during ordinary navigation. Each heading is synchronised and shows that the ship yaws gently within 1°.

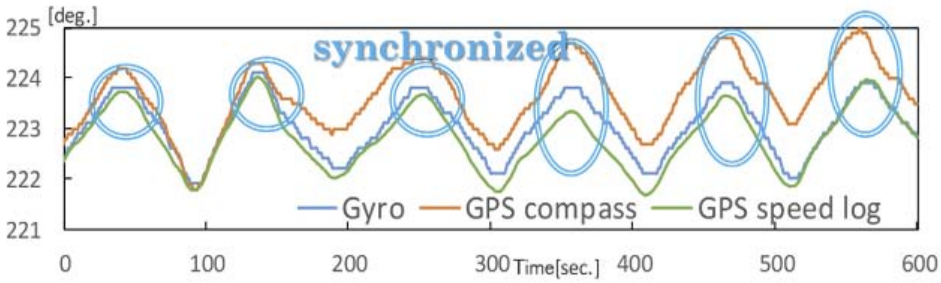

Figure 7. Heading during the ordinary navigation period

***4.3** Narrow channel navigation period.* Figure 8 shows the headings given by the different instruments during the period of ordinary navigation when the course was being altered. The dotted red circle highlights the moment at which the heading obtained by the GPS speed log changes later than the heading from the GPS compass. Presumably, the gyrocompass and GPS compass base their data from recordings in the same voyage recording system, but the GPS speed log records data directly and could not follow this minute change.

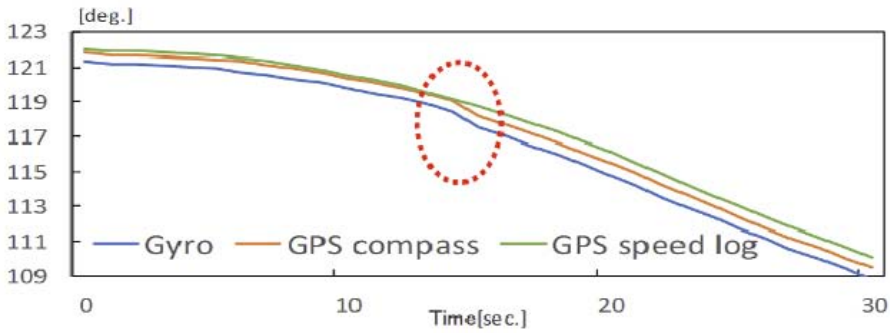

Figure 8. Heading during the narrow channel navigation period

***4.4** Port-entering.* Figure 9 shows the headings given by the different instruments and the ship's speed while entering port. These data derive from the period when the ship was reducing speed from dead-slow ahead to zero.

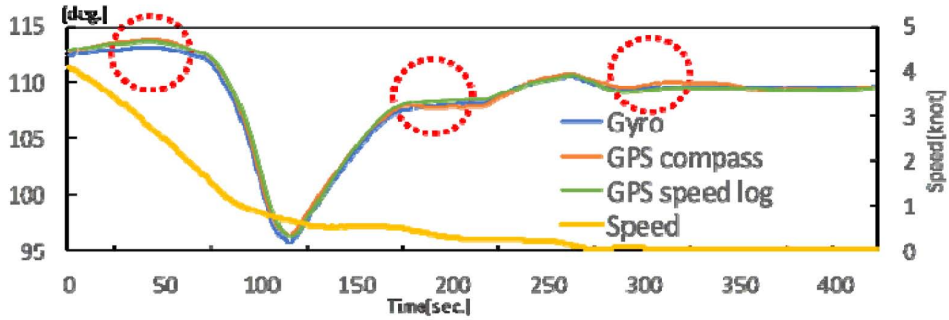

Figure 9. Heading during the port-entering period

The heading according to the gyrocompass and GPS compass became non-synchronized due to network error. As when passing through the narrow channel, the difference in the heading became larger when the ship altered course. In this period, this occurred just before and after altering course by a large angle of about 10°.

4.5 *Working period.* Figure 10 shows the headings obtained by the different instruments while working. The headings given by the gyrocompass and the GPS compass also came out of sync in this period. The heading from both GPS instruments peaked in periods that the gyrocompass readings were stable. This suggests that the GPS devices are unable to effectively process heading data during sudden stabilisation or accelerations, since the following speeds of the GPS instruments are 45° per second.

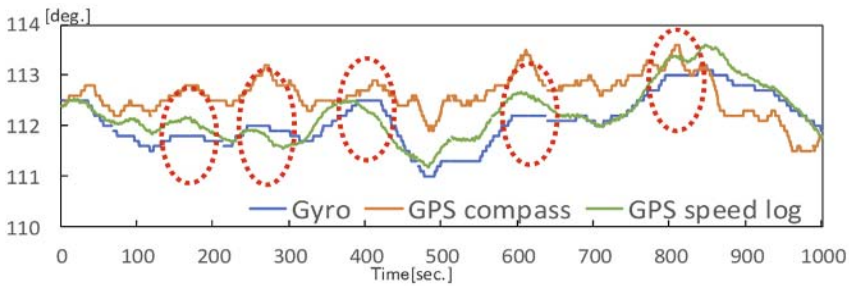

Figure 10. Heading during the working period

4.6 *Summary.* Table 6 summarises the heading results. The average and standard deviation from the gyrocompass heading every second, the maximum difference from the gyro heading, and the number of samples are indicated for each phase of

navigation. The characteristics shown below indicate that the headings from the GPS devices are accurate, because the average generally differs by less than 1°. However, the ship's movement must be considered carefully when using heading data from these instruments, since maximum differences can arise unexpectedly during the working period. In this case, the GPS instruments are not suitable for precise navigation.

Table 6. Summary of results for heading

Difference from Gyro heading	Ordinary		Narrow channel		Entering port		Working	
	GPS compass	GPS speed log	GPS compass	GPS speed log	GPS compass	GPS speed log	GPS compass	GPS speed log
Average (°)	0.3	0.6	0.4	0.4	0.4	0.3	0.7	0.2
Standard deviation	0.4	0.2	0.2	0.3	0.2	0.2	0.3	0.2
Maximum (°)	1.3	1.4	1.2	1.4	0.8	1.0	1.3	0.8
Sample size	3600		720		420		1800	

4.7 *Reliability index.* In the absence of more-reliable heading information, the data from the gyrocompass are used as the basis of the reliability model. The heading obtained with the gyrocompass can be expressed as in Equation (1):

$$G_C(t) = T_C(t) + \Delta d + G_E \tag{1}$$

where: G_C ... gyro course that changes every second, T_C ... true course, i.e. exact ship's direction on the chart, which is not affected by external force (e.g. centrifugal force and daily rotation), Δd ... the drift as the ship is swept by the current and wind that usually affects G_C, G_E ... intrinsic error due to instrumentation, which cannot be eliminated, but is negligible in case of the gyrocompass.

The gyrocompass has a static error of ±0.3° and a dynamic error of ±0.5° (Table 3). The static error is caused by daily rotation of the earth and changes in the latitude. The dynamic error is caused by alterations to the ship's course and speed (Seiki, 1997). The gyrocompass uses an integrated gyroscope and is able to indicate headings without any transfer time. Equation (2) expresses the heading obtained using a GPS device:

$$GP_C(t) = T_C(t') + GP_E, \quad t' = t_0 + \Delta t \tag{2}$$

where: GP_E ... the measurement error (e.g. due to tropospheric and ionospheric delay, multipath, etc), t_0 ... the time as logged by the gyro compass.

The GPS data has some transfer delays versus the gyro data because of the long distance from antenna to receiver; therefore, the GPS receiver gives the heading with a short time delay. The transfer delay is calculated from the capacity of the interface as connecting with the antennae and receiver. In this experiment, the data interface connecting the GPS compass and GPS speed log to the data recorded are identical (Table 3), and both distances are about 30 m. According to standards of the International Electrotechnical Commission, the transfer speed of GPS devices used for navigation should be about 9.6 kbps (Sokei, 2017). Table 7 lists the transfer times calculated from data volume and transfer speed at different levels of supposed transmission efficiency (CMAN, 2017).

Table 7. Calculated transfer time along the 30 m cable length

Transmission efficiency (%)	GPS compass Transfer time (s)	GPS speed log Transfer time (s)	Transfer speed	
			(kbps)	(kB/s)
100	0.2	0.1	9.6	1.2
90	0.2	0.2	8.6	1.1
80	0.2	0.2	7.7	0.96
70	0.2	0.2	6.7	0.84

However, the transfer times in this table are only theoretical, and should be repeatedly verified since they will change with circumstances. Additionally, differences in the sequences of the GPS data due to data processing should be researched (i.e. Kalman filtering, relation with number of antennae).

The terms outlined above allow a model of GPS instrument reliability to be proposed. This model is illustrated in Figure 11.

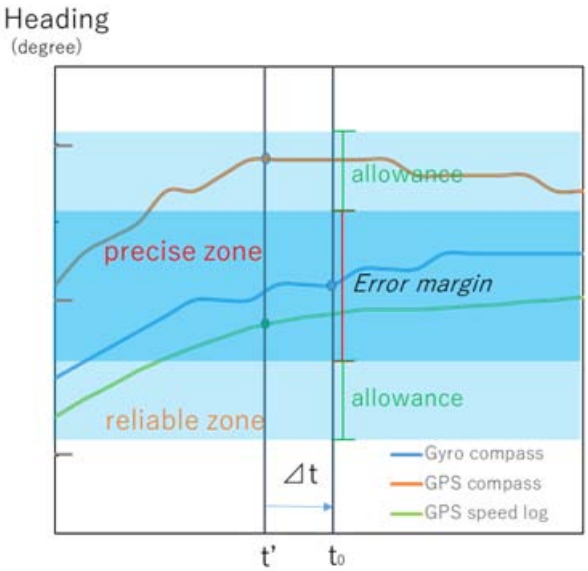

Figure 11. Reliability index

In Figure 11, the vertical axis gives the heading in degrees and the horizontal axis represents the time elapsed. On each heading curve, the points from the GPS instruments, taking the time delay effect into account, indicate information received at the same time as the gyrocompass. As noted previously, the navigator usually has faith in gyrocompass and would evaluate the gyro heading as absolutely true. In this case, the data from the gyrocompass is set as standard to assess the other instruments. The red bar shows the *error margin*. It must be used for the error margin by static error when the ship is at berth or the dynamic error when she is moving under the Table 3. If the heading is within the error margin, it can be deemed as the precise range. However, *allowance* must be made for reliable (usable) range even if the heading data is differing precise range. The allowance should be judged by the navigator in each situation. In the case of Figure 11, the point of GPS speed log is inner the precise zone and the point of GPS compass is in reliable zone. The GPS speed log is more precise than the GPS compass.

Figure 12 shows an application of the reliability index. In Figure 12, each curve gives actual recorded data when the ship is moving for 1 second. The transfer time Δt of both GPS instruments are assumed to be 0.2 second in Table 7. GPS instruments have transfer delays; therefore, the indicated times are 0.2 seconds later than the gyrocompass. The dynamic error of gyrocompass is ±0.5°. The precise

zone is set ±0.5°. The dynamic error of THD in IMO standards is defined as ±1.5°. The allowance is 1° from the end of precise zone ±1.5° from the end of the reliable zone.

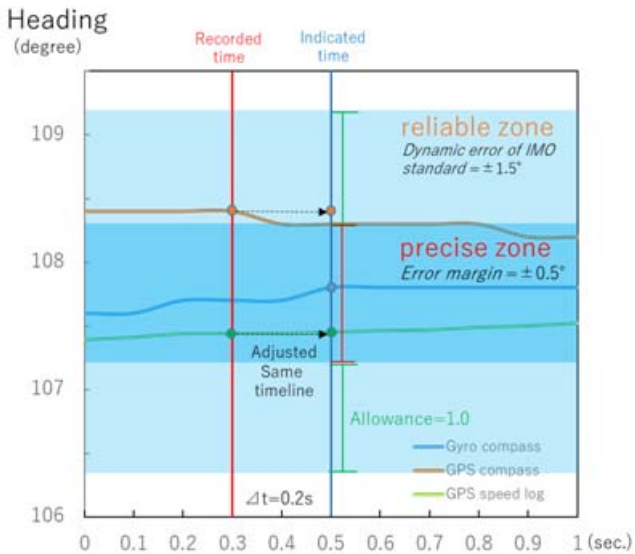

Figure 12. Application of the reliability index

Thus, assessments that the value is precise or reliable can be defined according to Equation (3):

$$Vp = \frac{|\,GP_C(t') - G_C(t_0)|}{|\;E_M\;|}$$
$$Vr = \frac{|\,GP_C(t') - G_C(t_0)|}{|\;E_M + a\;|} \tag{3}$$

where: E_M ... the error margin, a ... constant allowance judged by the navigator, V_p ... precise value, V_r ... reliable value. For each, the maximum acceptable value is 1.0; if it is over 1.0, the heading data is judged imprecise or unreliable.

Table 8 shows the results regarding the assessment of the heading values as precise or reliable. The reliable zone included allowance was set to 1.0° and the reliable zone included allowance except the in-berth period was set to 1.5°, according to the IMO standards.

Table 8. Results for assessment as precise and reliable

		In-berth	Ordinary	Narrow channel	Port-Entering	Working
GPS Compass	Precise assessment	0.7	0.9	2.2	1.5	1.9
	Reliable assessment	0.2	0.3	0.7	0.5	0.6
GPS Speed log	Precise assessment	3.4	0.4	1.3	1.0	0.5
	Reliable assessment	1.0	0.1	0.4	0.3	0.2

The results show that when the ship is berthed, both of the assessment values for the GPS speed log are over 1.0; however, as the ship does not move while berthed, it is not necessary to use these data for navigation. During ordinary navigation, all the assessment values are less than 1.0, indicating that GPS devices can be used for heading determination during ordinary navigation. When navigating a narrow channel, entering port and working, some assessments exceed 1.0. In particular, the assessment value for the GPS compass reaches more than double.

These three situations call for frequent alterations to the course. The GPS compass intrinsically measures the changes of positions of three antennas, and finally the orientation of this system in the earth-centred earth-fixed (ECEF) reference system; therefore, this may explain the difference between the GPS headings and the gyrocompass headings. Thus, the suitable allowance for the navigational situation at hand should be considered when assessing instrumental reliability.

5. CONCLUSIONS

This study presents an experiment carried to compare the reliability of a GPS compass and a GPS speed log for giving heading data, which is supplied by both of these instruments. The information obtained from these instruments was referenced against data from gyrocompass.

Both GPS-based instruments provided similar heading information to the gyrocompass, indicating that they can be used equally well for ordinary navigation. However, note that the accuracy of these instruments is decreased during periods of sudden stabilisation and acceleration while the ship changes course.

This experiment has revealed several patterns that will require further experiments to understand more fully. The relationship between the heading and sudden stabilisation and acceleration of the ship should be evaluated. Second, experiments can be made more accurate with more-reliable ground-truth instrument. Third, additional data should be collected in poor weather.

In this experiment, the relationship between the heading shown and stabilization and acceleration of the ship was not clear. A more accurate experiment with the more-reliable reference instrument and exploring the origins of GPS delays may help reveal the reason for the observed differences. To do this, the static and dynamic error of all instruments will need to be analysed in further detail. Furthermore, no data were obtained during foul weather, since the weather was clear during the test voyage, even though the voyage was scheduled in typhoon season. Another voyage is planned for later this year, in the hope that data will be recorded under poor weather conditions.

ACKNOWLEDGEMENTS. We are grateful to Mr. TSUTAE, of TOYO CONSTRUCTION CO., LTD, for helpful discussions, and we gratefully acknowledge the work of past and present members of our laboratory.

References

CMAN (2017). Web convenience note, network transfer time and speed calculation. Available at: https://note.cman.jp/network/speed.cgi, accessed 6 July 2018.

Hashimoto, S. *et al.* (2012). *Basic of ship handling*. 2nd Edition. Tokyio: Kaibundo.

International Maritime Organization (IMO) (2000). *Resolution MSC.116(73): Performance Standards for marine transmitting heading devices(THDs)*. London: IMO.

Japan Coast Guard (JCG) (2016). *Tide table Volume I*. Tokyo: JCG.

Japan Coast Guard (JCG). (2015). The present state and prevention of the sea disaster. Available at: http://www.kaiho.mlit.go.jp/info/kouhou/h28/k20160316/k160316-1.pdf, accessed 19 August 2016.

OceanDataRat (ODR). (2018). NMEA String Reference. Available at: http://www.oceandatarat.org/?page_id=723, accessed 19 September 2018.

Seiki, T. (1997). *Gyro-sensor technology*. Tokyo Electrical University Publication. pp. 108–109.

Sokei, D. (2017). International standard of connection cable and connector. Available at: http://denso.sokei.co.jp/sekkei_kouji_data/7.3.html, accessed 6 July 2018.

TUMSAT-OACIS Repository (2006). Note on gyro compass error comparison with Ring laser gyro from Pohnpei to Tokyo. Tokyo University of Marine Science and Technology.

Sveučilište u Rijeci
POMORSKI FAKULTET
FACULTY OF MARITIME STUDIES
University of Rijeka

University of Zagreb
Faculty of Transport
and Traffic Sciences

Royal Institute of Navigation
Science Technology Practice

12th
Annual
Baška GNSS
Conference

INTEGRATED APPROACH TO SAILING BOAT CONTROL PROBLEM

Alan Mahne Kalin, Dejan Žagar, Peter Vidmar

University of Ljubljana, Faculty of Maritime Studies and Transport, Portorož, Slovenia

e-mail: alan.mahne.kalin@fpp.uni-lj.si (Corresponding author)

Abstract

The standard rudder autopilot algorithms usually use a mix of PID and fuzzy algorithms to control the rudder input signal. Usually, the heading data (and error) are taken from an electronic magnetic compass and GPS receiver, so the whole system is based on the heading parameter only and the cyclic disturbances due to external forces are "unknown" to the autopilot. From a dynamic point of view, an increasing roll angle increases the weather helm, which can overcome the maximum reacting force of the rudder, causing a broach. Such a problem redirected us to a more integrated approach to the control system, with the aim to detect and possibly avoid such dangerous situations. In this paper, an integrated approach to sailing boat control problem is described. The approach is based on the modelling of forces and torques acting on the sail boat, at each instant, using inverse dynamics. Based on this model an optimal solution for rudder angle is found and inserted in the PID calculation as an added term. To test this approach, a simulator was built using the same mathematical model, reacting to the external weather conditions in the time domain. To test the approach, two simulations were ran using a PID control loop and a control loop based on inverse dynamic, for the same external conditions and course-keeping orders. The simulation emulated a gust, to which the boat with classical PID broached, while the other didn't.

Keywords: *sailing boat, kinematic sensor, dynamic model, PID*

1. INTRODUCTION

There are many authors that tackled the control problem of a sailing boat, hereby are stated the ones that inspired this approach. (Santos *et al.*, 2016) used a proportional-integral-derivative (PID) controller for rudder and a fuzzy control set of rules for sails of a robotic boat. Stelzer (2012), in his thesis used the Mamdani type fuzzy inference system to control rudder and sails simultaneously. Both authors aimed to manoeuvring capability of the boat for various robotic competitions. In (Stelzer, 2012) weather helm was counteracted by manoeuvring the sails based also on the rolling angle. He chose not to use PID control algorithms mainly because of (Stelzer, 2012):

1. It is difficult to adjust manually because the operator usually lacks the necessary insight into control theory.
2. The optimal adjustment varies and is not known by the user. Changing circumstances require manual readjustment of a series of settings.

as found in (Burns, 1995) and (Van Amergoen, 1984). The last statement can be taken as the leading motivation for this work.

Stenersen (2016) designed a small scale autonomous sail boat that used a moment mapping function for genoa and main-sail to control the weather helm. Our aim was to give more dynamics related feedback to the control algorithm, and so we developed our mathematical model based on (Mahne Kalin *et al.*, 2018), that uses kinetic sensors. A thorough mathematical modelling of motions of a sailboat can be seen in (Angelou and Spyrou, 2017).

The integrated approach is based on the inverse dynamic of a rigid body. The boat is virtually divided in components, which in our cases are: hull, keel, rudder and two sails. Each component has its own model that calculates the resulting external forces from available measured data. Sail, rudder and keel are treated as lifting surfaces, so the external force is calculated giving a resulting fluid velocity vector. The hull calculates the stability moment from roll and pitch, where the assumption of flat water is taken. The hull resistance is calculated from available measurement data using interpolation. The inverse dynamic calculates the forces and torques acting on the sailboat; of special interest in the control problem is the torque acting around the z-axis in the global coordinate (the one pointing up). This torque is the actor that gives rise to the angular acceleration that turns the boat off-course. Having that information at hand, the autopilot can react properly to some special

situations, where the weather helm would prevail. A special situation like this was tested in the numerical simulation experiment.

2. SIMULATOR

2.1 *Simulator Details*. Since we have not yet an available robot sailing boat, a simulator of she was composed to test our approach to control problem. The simulator is written in MATLAB® using classes.

The simulator is based on forward dynamics (Featherstone, 2008), using first order time discretization, where the governing equations are

$$\sum \vec{F} = m\vec{a} \tag{1}$$

$$\sum \vec{\tau} = I\dot{\vec{\omega}} + \vec{\omega} \times (I\vec{\omega}) \tag{2}$$

where: m ... the mass, $\vec{a}$ the acceleration, $\vec{\omega}$ ... the angular velocity, I ... the mass inertia matrix, $\vec{F}, \vec{\tau}$ ... forces and torques acting on the boat, respectively, which are computed using mathematical models. All forces and torques are transformed to the boat frame of reference before being used in equations (1) and (2). Linear and angular accelerations resulting from these equations are integrated using Euler's method to get linear and angular velocity and position in the next time step. Updated orientation is computed according to (Fossen, 2011). The time step was set to 0.01 seconds.

The boat has its own class object[1] that carries the mass, inertia and hydrostatic data. It provides a calculation of righting moment and water resistance based on orientation and velocity. Here the assumption is made, that the water surrounding the boat is still, so the moment of stability is calculated directly from pitch and yaw. Random wave effects are inserted in the simulator as added pitch and roll in the hydrostatic stability calculator routine. Roll and pitch damping torques are included in the model to prevent chaotic resonances of boat dynamics. Damping torques are nonlinear and depend on the local omega and its square value taking inspiration from (Piehl, 2016). The hydrostatic righting moments were calculated directly from

[1] in programming language sense

the integration of submersed volume. The mass and inertia data were taken from computer aided design (CAD) model. The drag coefficients were calculated from computational fluid dynamics (CFD) simulations. Simulations were carried out in FLUENT® using the Volume of the fluid model (VOF), 2 degrees of freedom (DOF) dynamic model (heave and pitch motion only) with incoming speeds of 0.5, 1, 1.5 and 2 m/s. Turbulence modelling was carried out with the *k*-omega SST model. The simulation was carried out with the transient formulation until the drag force took a time-constant value and the absolute residuals were below 10^{-4}.

The sails, rudder and keel share a common class of control surfaces. The class carries data and functions to calculate reaction forces acting on the control surface and then passes results to the main program, where forces and moments are summed, to calculate the dynamic. The lift and drag coefficients $c(\alpha, V)$ for sails were calculated from CFD simulations, for selected speeds and angles of attack using k-omega turbulence model. The lift and drag coefficients of the keel and rudder were computed using a steady vortex lattice method code (VLM). The results for the coefficients were compared to the ones obtained by using equations stated by (Jiang *et al.*, 2014). The surface force acting on the control force is therefore calculated using the following equation structure

$$F = \frac{1}{2}\rho c(\alpha, V) A V^2 \tag{3}$$

where: ρ, A, α, V ... density, reference area, the angle of attack and local fluid velocity, respectively.

The local fluid velocity takes into account the tangential velocity of the centre of the area, to give a more realistic condition due to manoeuvring.

The main routine of the simulator can be described with the following procedure:

1. Initialization: the user defines constant parameters, weather and initial state of the boat;
2. Computation of forces and moments: the program computes forces and moments in local coordinate system for the boat and all the components attached to it, then sums them to the damping torques and external torque noises;
3. Computation of accelerations: based on mass and inertia data computes the resulting acceleration of a rigid body;

4. Displacement: does a time integration of acceleration to get velocity and position (angular and linear);
5. Refreshment of the state of the system passing the new state to all the components;
6. A measure of the state of the boat: this step returns the data that are added to noise and piped to the autopilot subroutine;
7. Autopilot subroutine calculates the reaction on control surfaces;
8. Application of autopilot reactions and go to (2) until reaching max iterations.

2.2 *Boat Model Details*. The boat model design was aiming toward and autonomous sailing boat, that can sustain rough weather, open seas and long voyages. Main properties of the model used in the simulator are 240 kg of mass, 2.4 m long, 0.9 m wide and 0.6 m of the draft. She carries two sails of 1.6 m^2 area each. The sails are rigid wings, which can rotate and are connected to the actuator through a spring system. The springs act as a safety measure; the sail eases itself when subject to a growing wind speed conserving the lift orientation. This feature was modelled in the simulator. It was the spring mechanism that allowed the boat to proceed also on the other tack (after the broach), and have still a propulsive force, as can be seen in Figure 3 (right).

3. IDOPID AUTOPILOT

3.1 *Overview and Motivations.* The ordinary rudder autopilot present on sailing boats is a PID control loop with heading error as input. That was our starting point.

PID control loop takes the error from the input and then computes the derivative (from previous time step) and integral (summing to previous time step). The each of the 3 parameters (error, derivative and integral) is multiplied by a proper gain. The sum of the results is the output signal, that is sent to the rudder actuator. The proportional part tracks the current error, the derivative tracks the changes, while the integral behaves as a memory.

Observing skippers steering the boat, we observed, that their "integral part"[2] is changing based on the conditions, rather than history. The mean rudder angle offset

[2] quotes are used to respect the skippers, that are not autopilots.

is proportional to the off-centring of the sails and to the roll angle. The greater the roll, the greater have to be the mean offset. That was the fact that inspired our approach.

If the PID is stable, the integral part carries the offset information but can take some time to reach equilibrium. Designing and tuning the autopilot can be challenging as more decisions have to be made. A very reactive autopilot would keep the course, but the actuators would work all the time and energy consumptions would be high; a slowly reacting autopilot would consume less energy but would have a delay to sudden changes of the system, e.g. because of a gust. To partially improve the classical method, the autopilot calculates the ideal angle of rudder to keep the torque around global *z*-axis (pointing toward zenith) near zero. The calculated angle is introduced to the PID loop replacing an integral part. This approach immediately calculates the needed offset and allow the proportional and derivative terms to control the small, higher frequency noise. From now on this approach would be referred to as inverse dynamic offset PID (IDOPID), to differentiate from the usual PID.

3.2 *Working Principles*. The ideal angle is calculated using an inverse dynamic approach (Mahne Kalin *et al.*, 2018) from boat kinetics and wind speed in a similar manner as the simulator calculates the forces acting on the boat and its appendages. The calculation starts from the calculation of torque acting around global *z*-axis due to all the components except the rudder; the result of this calculation represents the torque required from the rudder to give zero torque and zero angular acceleration in that time step. The optimal angle of the rudder is found using the Newton-Raphson root finding algorithm on a function where: the independent variable is the rudder angle, and the dependent variable is the sum of all torques around the *z*-axis. The optimization loop has a set threshold proportional to 1 Nm and also a limit in iterations. The root finding algorithm results are bounded by maximum angles. The absence of root means that the rudder cannot overcome the force exerted by the other components, or in other terms, the boat is getting out of control. Such situations can be precursors to a broach[3].

We choose to use the Newton-Raphson algorithm because the forces and torques are calculated mainly using interpolation functions or interpolation data that depends on the actual boat geometry. The use of this algorithm is more user-friendly to future changes.

[3] due to torque between propulsion and resistance forces.

The IDOPID routine can be expressed with the following equations

$$G(\delta) = \vec{t}_3 \cdot \left(\sum \vec{\tau}_i + \vec{\tau}_{rud}(\delta) \right); \qquad i \in \{all\ except\ rudder\} \tag{4}$$

$$G'(\delta_{IDO}) = \frac{G(\delta_{IDO} + \Delta\delta_{IDO}) - G(\delta_{IDO})}{\Delta\delta_{IDO}} \tag{5}$$

$$\delta_{IDO,i} = \delta_{IDO,i-1} - \frac{G(\delta_{IDO,i-1})}{G'(\delta_{IDO,i-1})}; \quad i \in \{1, \dots, n\}\ ;\ \delta_{IDO,0} = 0 \tag{6}$$

$$\delta_{k+1} = c_P P + c_I I + c_D D + \delta_{IDO,n} \tag{7}$$

where: $\vec{\tau}_3$ third row of the rotation matrix between the boat and inertial coordinate system, δ ... generally the rudder angle, $\vec{\tau}$ the torques of various modeled features, *c* ... the coefficients of classic PID controller, $\Delta\delta_{IDO}$ a user defined small angle to compute the derivative. The index *IDO* refers to the inverse dynamic nature, the index *k* in (7) refers to the actual time step, index *n* in (7) refers to the last output of the Newton-Raphson (6), where convergence criteria were met; index *i* in (6) is an iterator, index *i* in (4) represents the modelled features except for the rudder, that is represented by index *rud.* In equation (4) the last term represents a vector, which is intended to extract the 3rd component of absolute torque (around *z*-axis in an inertial frame).

4. SIMULATION RESULTS

4.1 *Initial Conditions*. A comparison test was made to check the differences between the two approaches. The test was run in the simulator described in section 2. Initial conditions were set with the wind coming from the north with speed of 10 knots, boat navigating on heading 300° with speed 2 knots. At time 10 s the wind speed increases to 20 knots in one second and then remains constant. The autopilot directives are to follow the initial heading 300°, then at time 5 s change heading to 290°, then at time 15 s turn back to 300°.

Since the boat is small, it is very reactive, and a change in course can destabilize her. The gust and the changes in course are posed to imply a broach to the boat. The sail position is set to -50° for both sails, and it doesn't change during the simulation.

This constant[4] sail angle should support the broaching event. With regards to the experiment, PID coefficients were chosen with a trial and error approach and their gains were [0.8, 0.5, 0.03]. The trial and error experiment were carried on straight course keeping without gusts. A better combination of coefficients can exist for this particular case. For both autopilots the coefficients were the same, only the inverse dynamic offset was added to the autopilot output signal. That condition was chosen to compare the classical with the alternative autopilot directly.

4.2 *Results.* The results are shown in figures 1, 2 and 3. Figure 1 compares the time evolution of roll and pitch angles, the heading error and speed for the two autopilots. Only the time interval between 10 s and 20 s is shown, to have a more detailed view of the broaching event that happens around time 16 s. At time 10 s the wind starts to increase and at time 11 s it reaches the steady value of 20 knots. In both cases, the roll angle increases.

The PID autopilot initially provokes some sort of oscillation in heading error, which at time 15 s diverges in a broach. Looking at the rudder reactions it can be seen, that rudder angle and heading error oscillations have opposite phase. At manoeuvring time, the sudden change in rudder position creates a torque with the same sign, as the already present weather helm, which causes the broach.

The IDOPID autopilot reacts smoothly to the gust, as can be seen in the heading error line. Also, at the manoeuvre, the weather helm is taken into account at every iteration, and the response seen in the heading error is very similar to a typical PID regulator of the single-input-single-output system.

5. CONCLUSION

This was only a first attempt to check if the idea of a IDOPID is sound. On the basis of the results we conclude, that the approach looks better than the classical PID for this application. We aim to test and improve the model with sea trials. The next step in our research would be in treating the effects of sea surface waves with the available measurement equipment on board in real time.

[4] the sail angle is subject to the torque acting around the mast axis, which is connected to a spring, so the sails rotates if the forces acting upon them are too strong, as described in section 2.2.

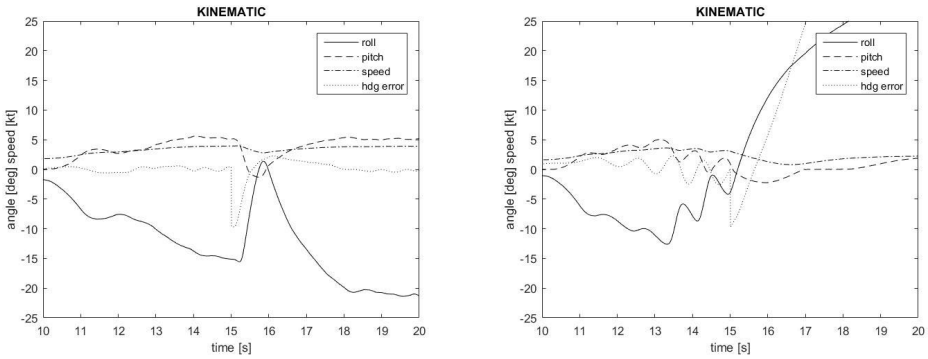

Figure 1. Comparison between IDOPID (left) and PID (right) kinematic at time 10 s to 20 s

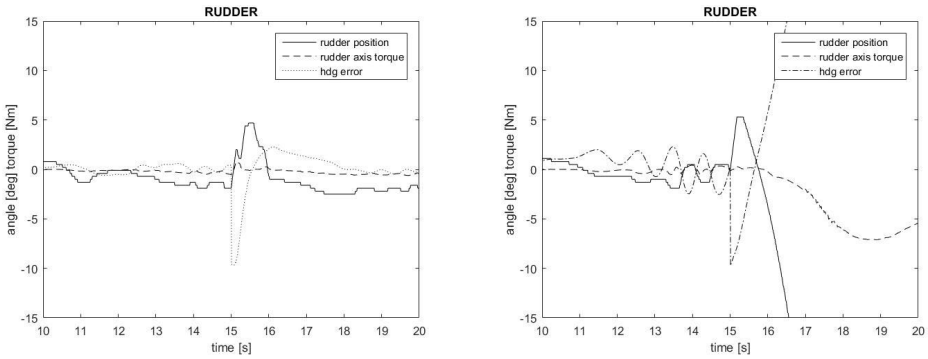

Figure 2. Comparison between IDOPID (left) and PID (right) rudder data at time 10s to 20s

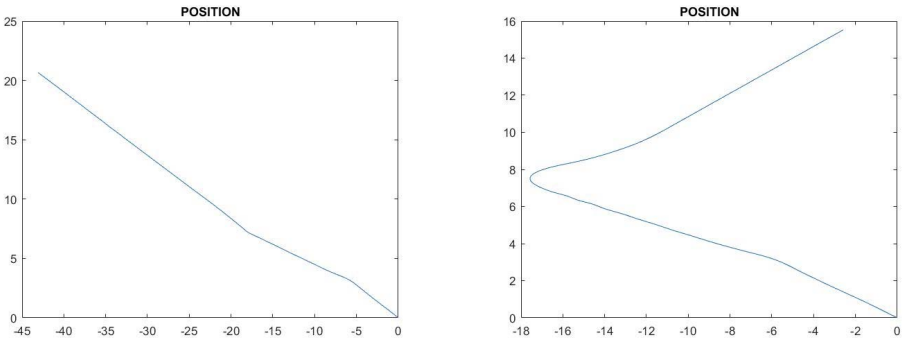

Figure 3. Comparison between IDOPID (left) and PID (right) rudder data at time 0 s to 30 s. The PID (right) autopilot involuntary broaches and tacks at time 16 s and cannot return to the ordered course without a change in sails' position. Boat continues to navigate after broach, because the spring system "eases the sheet" when pressure increases.

The integrated approach described in this article can be applied to any sailing boat, having at hand the relevant coefficients needed for its modelling, which is a major obstacle to this method. On the other hand, the model can be run in real time and can also be used on other control algorithms, to calculate the positions of control surfaces to obtain desired torque around the vertical axis. The practical effect of IDOPID control loop is, that predicts the needed rudder offset due to weather helm.

References

Angelou, M. and Spyrou, K. (2017). A new mathematical model for investigating course stability and maneuvering motions of sailing yachts. *Journal of Sailing Technology*. pp. 1–42.

Burns, R. (1995). The use of artificial neural networks for the intelligent optimal control of surface ships. *IEEE Journal of Oceanic Engineering*. 20(1). pp. 65–72.

Featherstone, R. (2008). *Rigid Body Dynamics Algorithms*. New York: Springer Science+ Business Media.

Fossen, T. I. (2011). *Handbook of marine craft hydrondynamics and motion control*. Hoboken: John Wiley & Sons, Inc.

Jiang, H., Li, Y. and Cheng, Z. (2014). Relations of lift and drag coefficients of flow around flat plate. *Applied Mechanics and Materials*. 518. pp. 161–164.

Mahne Kalin, A. (2014). *Uporaba Xsens MTI/g senzorja pri meritvi dinamičnih karakteristik šolske jadrnice Solarije*. Master Thesis. Portorož: Faculty of Maritime Studies and Transpot.

Mahne Kalin, A., Žagar, D. and Vidmar, P. (2018). Estimation of forces acting on a sailboat using a kinematic sensor. *Transactions on Maritime Science*. 7(2). pp. 128–135.

Piehl, H. P. (2016). *Ship Roll Damping Analysis*. Doctoral Dissertation. Hamburg: Fakultät für Ingenieurswissenschaften, Abteilung Maschinenbau und Verfahrenstechnik. p. 102.

Santos, D. *et al*. (2016). Design and implementation of a control system for a sailing robot. *Robotics*. 5(1). pp. 1–24.

Stelzer, R. (2012). *Autonomous Sailboat Navigation – Novel algorithms and experimental demonstration*. Doctoral Dissertation. Leicester: De Monfort University.

Stenersen, H. S. (2016). Construction and control of an autonomous sail boat. *IFAC-PapersOnLine*. 49(23). pp. 524–531.

Van Amerogen, J. (1984). Adaptive steering of ships – A model reference approach. *Automatica.* 20(1). pp. 3–14.

Technical co-sponsors

Beihang University

Satellite Navigation University Network

Sveučilište u Rijeci
TEHNIČKI FAKULTET

Sveučilište u Zagrebu 1876 1946
PMF
Prirodoslovno - matematički fakultet

Media coverage

Coordinates
A monthly magazine on positioning, navigation and beyond